UNIVERSITÀ
DEGLI STUDI
DI PADOVA

Dipartimento di Scienze Chimiche

SCUOLA DI DOTTORATO DI RICERCA IN SCIENZA E INGEGNERIA DEI MATERIALI

XXV ciclo

MESO- AND NANO-STRUCTURED METAL-DIELECTRIC INTERFACES FOR PLASMONIC NANOFOCUSING

Direttore della Scuola: Ch.mo Prof. Gaetano Granozzi

Supervisore: Ch.mo Prof. Filippo Romanato

Dottoranda: Marta Carli

To all those who believed in me, even when I did not

Abstract

With increasing demand for nanoscale optical devices, the ability to confine the light on length scales smaller than those allowed by the diffraction limit of light has begun to attract enormous interest. A possible solution to this problem is offered by Plasmonics.

Under certain conditions, a metal-dielectric interface supports Surface Plasmons (SPs), i.e. electromagnetic excitations strongly coupled to oscillations of free electrons in the metal. Thanks to these excitations, electromagnetic energy can be confined in a sub-wavelength volume close to the metal surface. This opens up the way for a wide range of opportunities and applications, from photovoltaics to biosensing.

The focus of this thesis was to engineer metal-dielectric interfaces in order to excite plasmonic hotspots, i.e. nanometer-sized regions where the electromagnetic field is strongly enhanced. As hinted above, this can be achieved by conveniently meso- and/or nano-structuring the metal surface. The properties of metal-dielectric interfaces emerging from these studies are of particular interest in the field of molecular sensing, but are also of more fundamental interest.

Different classes of devices are proposed. We started from digital plasmonic gratings, studying their excitation modes thoroughly. We then moved to nanostructures supporting a Localized Surface Plasmon Resonance (LSPR), specifically plasmonic nanoantennae, which are of special interest for the enhancement of well-established sensing techniques such as SERS. Coming to nanofocusing, we studied plasmonic wedges – which provide *adiabatic nanofocusing* at their ridge – as well as bull's eye/Archimedean spiral structures, which can generate and focus Surface Plasmons carrying orbital angular momentum (OAM). Finally, we proposed a non-trivial integration of the above-mentioned effects, in the form of an Archimedean spiral coupled to nanoantenna resonators.

In parallel, we collaborated with the company *A.P.E. Research* to develop a new characterization instrument, called *EllipsSNOM*. It consists in implementing a SNOM head on a J.A. Woollam Co. Inc. Variable Angle Spectroscopic Ellipsometer (VASE). This challenging task was pursued in order to get simultaneous control of the far field and the near field properties of the structures; ellipsometry and SNOM microscopy are indeed both essential techniques to achieve a full characterization of plasmonic nanodevices.

Compendio

All’aumentare della richiesta di dispositivi ottici di scala nanometrica, la possibilità di confinare la luce su scale di lunghezza inferiori a quelle consentite dal limite di diffrazione della luce ha iniziato ad attrarre un enorme interesse. Una possibile soluzione a questo problema è offerta dalla Plasmonica.

In determinate condizioni, un'interfaccia metallo-dielettrico supporta Plasmoni di Superficie (SP), cioè eccitazioni elettromagnetiche fortemente accoppiate alle oscillazioni degli elettroni liberi nel metallo. Grazie a queste eccitazioni, l’energia elettromagnetica può essere confinata in un volume di dimensioni inferiori alla lunghezza d’onda della luce vicino alla superficie metallica. Questo apre la strada a una vasta gamma di opportunità e applicazioni, dal fotovoltaico alla biosensoristica.

L’obiettivo di questa tesi è stato progettare interfacce metallo-dielettrico al fine di eccitare *hotspot* plasmonici, cioè regioni di dimensioni nanometriche dove il campo elettromagnetico è fortemente potenziato. Come accennato sopra, questo può essere ottenuto meso- e/o nano-strutturando opportunamente la superficie del metallo. Le proprietà delle interfacce metallo-dielettrico che emergono da questi studi sono di particolare interesse nel campo della sensoristica, ma sono anche di interesse più fondamentale.

Sono proposte diverse classi di dispositivi. Siamo partiti da reticoli plasmonici digitali, studiando a fondo i loro modi di eccitazione. Ci siamo poi spostati su nanostrutture che supportano una Risonanza Plasmonica di Superficie Localizzata (LSPR), nello specifico nanoantenne plasmoniche, che sono di particolare interesse per il potenziamento di tecniche sensoristiche ben consolidate come il SERS. Venendo poi al nanofocusing, abbiamo studiato strutture plasmoniche tipo *wedges* (cunei) – che forniscono *nanofocusing adiabatico* sulla loro cresta – e strutture tipo *bull’s eye*/spirali di Archimede, in grado di generare e focalizzare Plasmoni Superficiali che trasportano momento angolare orbitale (OAM). Infine, abbiamo proposto un'integrazione non banale degli effetti sopra citati, in forma di una spirale di Archimede accoppiata a una nanoantenna.

In parallelo, abbiamo collaborato con la ditta *A.P.E. Research* per sviluppare un nuovo strumento di caratterizzazione, chiamato *EllipsSNOM*. Esso consiste nell’implementazione di una testa SNOM su un ellissometro spettroscopico J.A. Woollam Co. Inc. Variable Angle Spectroscopic Ellipsometer (VASE). Questo intrigante obiettivo è stato perseguito al fine di ottenere il controllo simultaneo delle proprietà di campo lontano e di campo vicino delle strutture; ellissometria e microscopia SNOM sono infatti entrambe tecniche essenziali per realizzare una completa caratterizzazione dei nanodispositivi plasmonici.

Table of contents

Introduction

The study of light and especially the interaction of light with matter has always stimulated the interest of the scientific community. Half a century ago, Richard Feynman was well aware that "*there is plenty of room at the bottom*", thus paving the way for the development of nanotechnology. Accessing the "nanoworld" unveiled the fact that, besides providing the well-known electrical properties, the electron gas in noble metals also determines surprising *optical* properties, arising from its interaction with high-frequency electromagnetic fields. The study of these optical phenomena led to the development of Plasmonics, which studies the properties of the electromagnetic field resulting from collective electronic excitations in noble metal films or nanoparticles. These oscillations are commonly termed as Surface Plasmons (SPs) due to their interfacial nature.

These striking properties are not manifest in everyday life. As a matter of fact, the dispersion of SP waves propagating on a flat metal surface lies outside the light cone and the direct coupling of incident light to these waves is therefore impossible. It was the enormous progress in nanofabrication technology which took place during the 90s which allowed us to enter the fascinating world of Plasmonics.

In my research work, I exploited these powerful nanofabrication techniques to design and fabricate different plasmonic nanostructures, presenting a number of interesting and still not completely understood phenomena. We started from "simple" devices presenting well-defined plasmonic resonances; then, we moved to more complex structures, combining different optical effects. The final goal was to propose efficient structures for the delivery and concentration of light into nanoscale hotspots, together with the fine control of its properties.

The characterization of the same structures is another important issue which is worth to be addressed; an entire chapter will be dedicated to the development of an innovative instrument which allows a full (far- and near-field) optical characterization of the devices.

This thesis is organized as follows.

In Chapter 1 we provide an introduction to some basic concepts of Plasmonics. We approach the problem by recalling the unique optical properties of metals and we show that the existence of Surface Plasmons is a direct consequence of these properties. In particular, we discuss Surface Plasmon Polaritons (SPPs), with a special attention to their dispersion relation, and the

Localized Surface Plasmon Resonance (LSPR), due to the interaction between electromagnetic fields and sub-wavelength metal nanoparticles.

In the following two chapters (2 and 3), we start by considering two simple plasmonic structures, supporting propagating SPPs and LSPR, respectively. These studies allowed us to get a deep insight in the physical and material science properties of different plasmonic substrates, and we also describe their practical use for biosensing.

In Chapter 2, the first class of plasmonic structures investigated during this work is presented. It consists of gold digital gratings, lithographed and electrolytically grown on a substrate. We propose a full analysis of this structure, discussing the different kinds of supported plasmonic resonances thoroughly. After that, we present a published work in which we designed, fabricated and characterized such a plasmonic grating for SERS, optimized for concentrating electromagnetic radiation inside the slits.

In Chapter 3, we address another kind of plasmonic substrate, i.e. nanorod-shaped antenna arrays; their localized resonance was once again exploited for SERS. We discuss the parameters affecting the resonance, in order to define precise guidelines for the design of our nano-material. We also address in detail the materials and fabrication strategies which were chosen for the optimization of the structure, in order to obtain well-defined and reproducible plasmonic nanoantenna substrates. The recently started collaboration with Politecnico di Milano about exploiting these structures for Surface Enhanced Coherent Antistokes Raman Scattering (SECARS) will also be briefly described and preliminary results will be shown.

Nanofocusing is the delivery and concentration of light at a scale smaller than the limit imposed by diffraction. It gives the title to this thesis and it is with this topic that we deal in the chapters from 4 to 6. In the framework of this thesis, it can be considered a further step with respect to the simple resonances described in the previous chapters, since it enables a true and controlled manipulation of the properties of light at the nanoscale.

In Chapter 4 we discuss a wedge-shaped structure which enables nanofocusing of SPPs at the ridge. As will be discussed in detail, this kind of nanofocusing principle belongs to the family of *adiabatic* nanofocusing [1]. The advantage of the proposed structure lies in an extremely simple and scalable nanofabrication process, which allows in particular to obtain extremely low curvature radii at the tip. We numerically and experimentally demonstrate that this configuration can be exploited for enhancing Raman signal and we perform accurate near-field characterization.

In Chapter 5, we explore the optical properties of a new class of structures that has been object of great attention in the Plasmonics community very recently. It is the *Plasmonic Vortex Lens* (PVL) structure [2], which consists in a spiral- or circular-shaped grating made of grooves

milled in a gold slab. The interest around this kind of chiral structures stems from their ability to couple impinging circularly polarized light to SPP possessing a non-zero orbital angular momentum (OAM), also termed Plasmonic Vortices (PVs). At the same time, the structures focus the coupled Plasmonic Vortex towards their center, acting as lenses; therefore, they are often referred to as Plasmonic Vortex Lenses (PVLs). Such a class of structures opens up new possibilities for sensing and/or TC applications.

The possibility to achieve full optical characterization of plasmonic structures, with many degrees of freedom, is of fundamental importance when proposing new plasmonic devices. That is the reason which drove us to start a project with A.P.E. Research, a well-known company located in Trieste, which produces and develops SPM-type microscopes (AFM, STM, SNOM), with a peculiar attention to research. The aim of the project was to design a custom SNOM head to be mounted and interfaced with a pre-existing ellipsometer.

In Chapter 6, we describe the whole project, which was carried in the framework of the PLATFORMS project. The combined system was called EllipsSNOM and it allows performing coupled near- and far-field measurements, as well as particular and easy-to-setup SNOM characterization. Such an instrument has never been described in literature or industry, and it is very promising since it allows to completely describe and investigate the optical properties of plasmonic surfaces and devices.

In Appendix 1 we give an overview of the fabrication and characterization techniques which were use throughout this thesis, with particular regard to Electron Beam Lithography.

Chapter 1

The striking optical properties of metal-dielectric interfaces: an introduction to Plasmonics

1.1 Introduction

Metal-dielectric interfaces show unique optical properties. One of the most striking phenomena encountered in these systems are electromagnetic resonances termed Surface Plasmons (SPs). Using a term borrowed from Physics, Surface Plasmons can be described as the *eigenmodes* of this metal-dielectric interface, in the sense that they arise as (evanescent) solutions of Maxwell's equations at the interface. Plasmonic modes exist in a number of geometries and metals, among which noble metals such as gold and silver are the most common [3, 4, 5].

The interaction of metals with electromagnetic radiation is largely dictated by the free conduction electrons in the metal. Under certain circumstances, light can excite collective oscillations of the electron gas, giving rise either to *propagating* or *localized* plasmons. It is worth noting that the existence of SPs is characteristic for the nanoscale at optical/NIR frequencies. A similar behavior cannot be simply reproduced in other spectral ranges using the scale invariance of Maxwell's equations, since the material parameters change considerably with frequency. The study of Plasmonics then fits into the long trail of scientists' efforts to understand and manipulate the interaction between light and matter, a story that goes back in time to Newton.

Plasmonic surfaces range from corrugated surfaces and interfaces to nanoparticles. In these systems, SPs can give rise to strongly enhanced optical near-fields which are spatially confined to the interface. In the case of a small sub-wavelength particle, the overall displacement of the electrons with respect to the positively charged lattice leads to a restoring force, which in turn gives rise to extreme local charge accumulations and thus by strongly enhanced optical fields.

The interest in plasmon modes dates back to the beginning of the 20th century [6, 7, 8], but recent advances in structuring, manipulating and observing on the nanometer scale have

revitalized this field. Even though these technological advances were at first driven by an increasing demand for semiconductor based integrated electronic components, optical applications are now receiving increasing attention. Nowadays, plasmons are one of the most promising strategies exploited in bio-molecule sensors [9], and they are seen as one possible route in the development of sub-wavelength optics [10].

In this Chapter, after a short historical overview, we recall the unique optical properties of metals that lie at the basis of their plasmonic behavior. We show in particular that metals support electromagnetic surface waves that we shall call Surface Plasmon Polaritons (SPPs). We will discuss the dispersion relation of SPPs, showing that they cannot be directly excited by free-space light, and we will introduce some common coupling methods. Then, we will discuss another kind of plasmonic resonance, the Localized Surface Plasmon Resonance (LSPR), which is due to the interaction between electromagnetic fields and sub-wavelength metal nanoparticles. Finally, some of the techniques used for the detection and characterization of plasmons will be presented.

1.2 Timeline of Plasmonics

Plasmonics as a field of science and technology is not older than a couple of decades. Yet its origins lie in the turn of 20th century (1899-1909), when Sommerfeld theoretically studied electromagnetic waves on metal wires [11, 8], retrieving surface modes which are electromagnetically equivalent to SPPs, and his student Zenneck proposed a presented a paper on planar surface electromagnetic waves [6]. In the same period, Gustav Mie established a clear mathematical foundation on scattering of light on small spherical particles [7].

It was also in those years that Wood illuminated a metallic diffraction grating with polychromatic light and noticed narrow dark bands in the spectrum of the diffracted light, which he referred to as anomalies [12]. Lord Rayleigh suggested a physical interpretation of the phenomenon [13], but it took several years until Fano [14] associated these anomalies with the excitation of electromagnetic surface waves on the diffraction grating and realized that they were a special case of the waves first suggested by Zenneck and Sommerfeld.

In 1957, Ritchie related the electron energy loss in metal thin films to the excitation of collective oscillation in the electron plasma [15] and the experimental verification followed two years later by Powell and Swan [16, 17]. Further investigation was performed by Stern and Ferrell, who introduced the term “Surface Plasmons” for the quanta of these surface collective oscillations [18]. In 1958, experiments with metal films on a substrate [19] again showed a large

drop in optical reflectivity, and ten years later the explanation and repeated optical excitation of SPs were reported by Otto [20] as well as Kretschmann and Raether [21].

In 1967 Teng and Stern [22] illuminated a diffraction grating by varying the angle of incidence of incoming radiation, obtaining peaks at well-defined angular positions. Using this information, they were able to determine the SPP wave vector parallel to the surface of the grating and hence the dispersion curve could be mapped out.

Intense research on Plasmonics began in the 1980s, as chemists began to exploit the striking properties of Surface Plasmons for the enhancement of Raman spectroscopy [23]. Surface Enhanced Raman Spectroscopy (SERS) [24, 25, 26] is now probably one of the most winning applications of Plasmonics. Finally, the flowering of nanotechnology over the past decade brought about a proliferation of techniques for fabricating structures at the nanoscale - exactly what Plasmonics needed to progress from laboratory curiosity to practical applications.

1.2 Optical properties of metals: an overview

1.2.1 The dielectric function

The response of a material to electromagnetic radiation can be described in general by a complex dielectric function ε, related to the (complex) refractive index by $\tilde{n} = \sqrt{\varepsilon}$ [27]. For a dielectric medium like glass, the refractive index at optical frequencies is nearly constant and predominantly real (for glass, it is around 1.5). For metals instead, we cannot speak of a dielectric constant but rather of a frequency-dependent *dielectric function* ε(ω) and different frequency regimes can be described. In the low frequency regime, metals are highly reflective and do not allow electromagnetic waves to propagate through them, as we know from everyday experience; for this reason, metals are traditionally employed as cladding layers for waveguides and resonators. We say that they act like perfect or good conductors, i.e. they can be described by means of an infinite or fixed finite conductivity, with a negligible fraction of the EM wave penetrating into the metal. In the visible part of the spectrum, however, this penetration increases and leads to more loss. As we approach the UV part of the spectrum, metals converge to dielectrics and become transparent after a certain frequency threshold, albeit with varying degrees of attenuation, depending on the details of the electronic band structure. These optical properties are determined mainly by the fact that (1) the conduction electrons can move freely

within the bulk of the material, and (2) interband excitations can take place if the energy of the photons exceeds the band gap energy of the metal.

The dielectric function enters Maxwell's equations [28] in a medium and it can be shown [4] that it is related to the conductivity of a metal through

$$\varepsilon(\omega) = 1 + \frac{i\sigma(\omega)}{\varepsilon_0 \omega} \tag{1.1}$$

It is worth noting that equation (1.1) reflects a certain arbitrariness in the separation of charges into bound and free sets. At low frequencies, ε(ω) is usually used for the description of the response of bound charges and it is related to the concept of polarization, while σ describes the contribution of free charges to the current flow. At optical frequencies however, the distinction between bound and free charges is blurred.

In general, ε(ω) is a complex number $\varepsilon(\omega) = \varepsilon_1(\omega) + i\varepsilon_2(\omega)$ and is related to the complex refractive index $\tilde{n} = n + i\kappa$ by

$$\varepsilon_1 = n^2 - \kappa^2 \tag{1.2}$$

$$\varepsilon_2 = 2n\kappa \tag{1.3}$$

$$n^2 = \frac{\varepsilon_1}{2} + \frac{1}{2}\sqrt{\varepsilon_1^2 + \varepsilon_2^2} \tag{1.4}$$

$$\kappa = \frac{\varepsilon_2}{2n} \tag{1.5}$$

The imaginary part κ of the refractive index is called the *extinction coefficient* and determines the optical absorption of electromagnetic waves propagating through the medium.

1.2.2 The Drude model

Over a wide frequency range, many metals can be well described by a simple model developed by Drude [29], where a gas of free electrons of number density n_e moves against a fixed background of positive ion cores. Details of the lattice potential and electron-electron interactions are not taken into account, but some characteristics of the band structure are incorporated into the effective optical mass m of each electron. The electrons oscillate in response to an applied electromagnetic field and they scatter with phonons, electrons, lattice defects or impurities. Thus, their motion is damped with a common average relaxation time τ;

usually, the damping is described via the collision frequency $\gamma = 1/\tau$. At room temperature, τ is of the order of 10 fs, which corresponds to $\gamma \approx 100$ THz.

The equation of motion of such a system can be written as $m\ddot{\mathbf{x}} + m\gamma\dot{\mathbf{x}} = -e\mathbf{E}$, where **E** is the external electric field. If we assume a harmonic time dependence of **E**, we can solve the equation obtaining $\mathbf{x}(t) = \frac{e}{m(\omega^2 + i\gamma\omega)}\mathbf{E}(t)$ [30]. Then, using the constitutive relations of electrodynamics we arrive at

$$\varepsilon(\omega) = 1 - \frac{\omega_p^2}{\omega^2 + i\gamma\omega} \tag{1.6}$$

where $\omega_p = \sqrt{\frac{n_e e^2}{\varepsilon_0 m}}$ is the plasma frequency. The real and imaginary parts of the dielectric function are

$$\varepsilon_1(\omega) = 1 - \frac{\omega_p^2 \tau^2}{1 + \omega^2 \tau^2} \tag{1.7}$$

$$\varepsilon_2(\omega) = \frac{\omega_p^2 \tau}{\omega(1 + \omega^2 \tau^2)} \tag{1.8}$$

We can distinguish two frequency regions:

a) if ω is larger than ω_p, $\varepsilon(\omega)$ is positive and the corresponding refractive index $\tilde{n}$ is a real quantity. This is the so-called "transparency regime".
b) if ω is smaller than ω_p, $\varepsilon(\omega)$ becomes negative and $\tilde{n}$ is imaginary, which implies that an electromagnetic wave cannot propagate inside the medium. It is in this frequency region that metals retain their metallic character and we will limit ourselves to this case.

For metals, ω_p typically lies in the ultraviolet region, so the visible part of the spectrum falls in the latter case: that is why metals are shiny and glittering at visible frequencies.

If we consider "large" frequencies close to ω_p, however, $\varepsilon(\omega)$ is predominantly real, and we get

$$\varepsilon(\omega) = 1 - \frac{\omega_p^2}{\omega^2} \tag{1.9}$$

This equation can be interpreted as the dielectric function of the undamped free electron plasma. In a first approximation we will use this expression when discussing Surface Plasmons.

Figure 1.1 plots the real and imaginary part of the dielectric function of a Drude metal. We note that the real part is negative over the visible range where $\omega < \omega_p$.

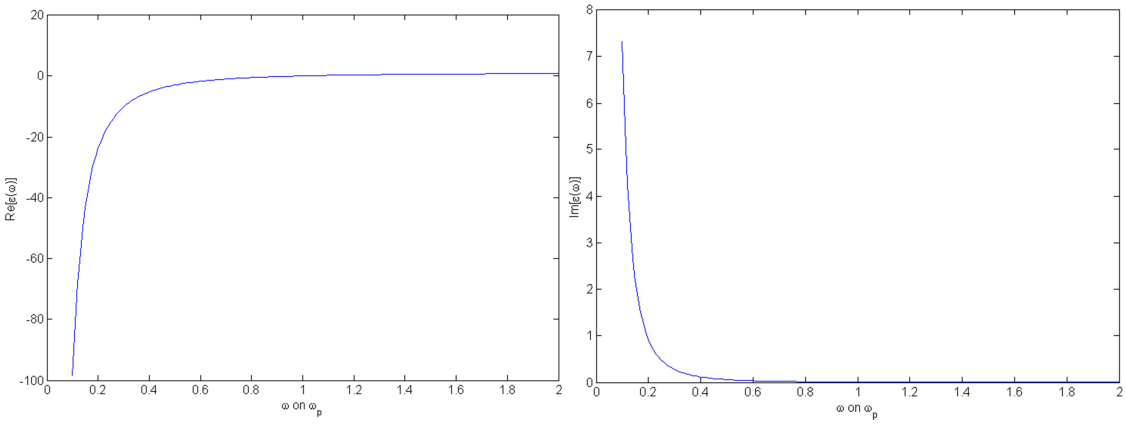

Figure 1.1 Real and imaginary parts of the dielectric function of a Drude metal, with the frequency expressed in terms of the plasma frequency ω_p.

1.2.3 Noble metals

At high frequencies, the Drude model describes the response of most metals less accurately, due to the presence of interband transitions [30]. This happens down to visible frequencies for noble metals such as gold and silver. For these metals, an extension to this model is needed, since the filled *d*-band close to the Fermi surface causes a highly polarized environment. This effect can be described by a dielectric constant ε_∞ (usually $1 \leq \varepsilon_\infty \leq 10$), and we can write

$$\varepsilon(\omega) = \varepsilon_\infty - \frac{\omega_p^2}{\omega^2 + i\gamma\omega} \tag{1.10}$$

This correction helps, but is still not enough to describe the experimental data correctly. This is particularly true for the imaginary part of $\varepsilon(\omega)$ where the contribution of electrons from the *d*-band is crucial. Therefore, the real and imaginary parts of $\varepsilon(\omega)$ which shall be used in the simulations are taken from experimental (ellipsometry) data.

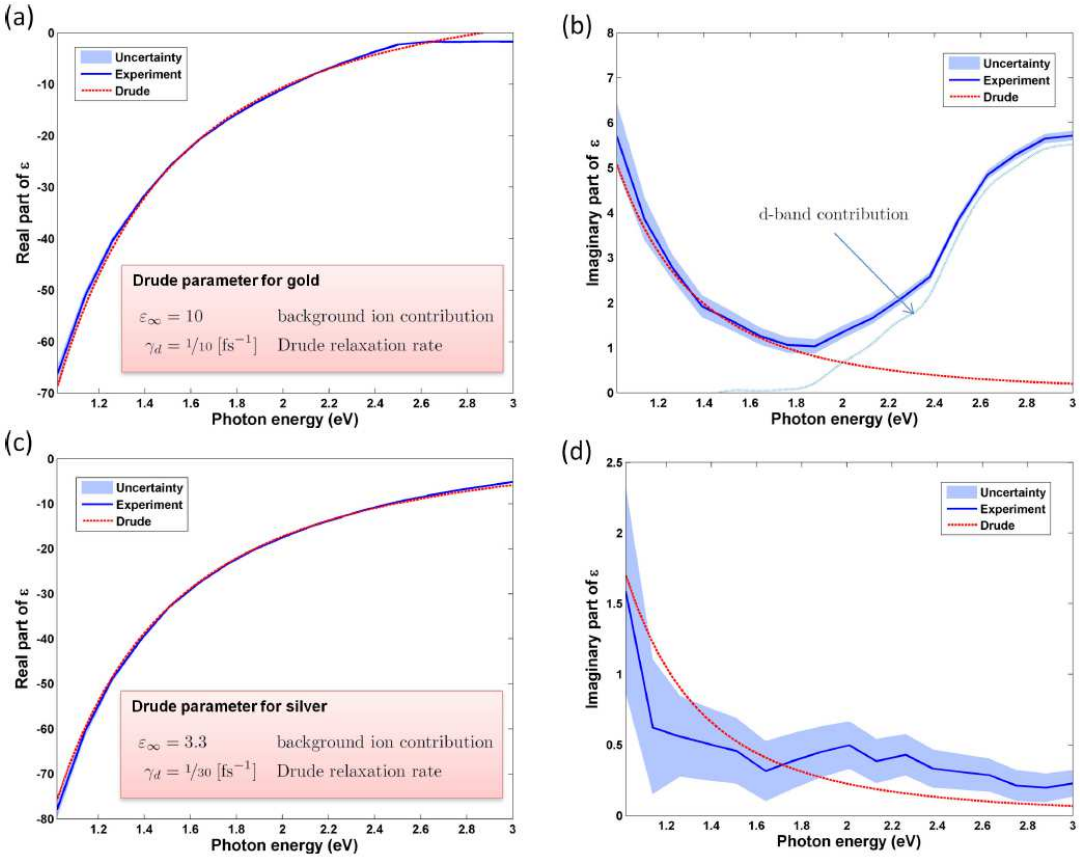

Figure 1.2 Real and imaginary parts of the dielectric function for gold (a)-(b) and silver (c)-(d). The experimental data together with the measuring uncertainty have been taken from Johnson and Christy [31].

One last remark can be extrapolated from the plots reported in Figure 1.2. It can be seen that the metal that exhibits the smallest absorption while having a large and negative real part of ε(ω) throughout the visible and NIR frequency regime is Ag, while Au is a good alternative in the NIR. This fact will be taken into account later when choosing the proper materials and experimental conditions.

1.3 Surface Plasmon Polaritons at a metal-dielectric interface

1.3.1 The dispersion relation of SPPs

As we said in the introduction, Surface Plasmons are collective electron oscillations existing at metal-dielectric interfaces. When SPs are coupled with electromagnetic energy, they are called Surface Plasmon Polaritons (SPPs). SPPs are *propagating* light waves that are bound to

and guided along a metal-dielectric interface and are different from Localized Plasmons which will be discussed in Section 1.5[1].

SPPs are evanescent modes, i.e. the amplitude of the SPP field decays exponentially away from the metal surface. Thus, they are confined at the interface, where the electromagnetic fields are highly enhanced.

The equation that describes the behavior of SPPs is their dispersion relation, i.e. the relationship between the angular frequency and in-plane wave vector k_{SPP}. The dispersion relation can be easily obtained from Maxwell's equations, introducing some hypotheses which shall be discussed here briefly. For a complete derivation we refer to [4].

1. *We consider the planar interface of two semi-infinite, optically isotropic, homogeneous, non-magnetic media.*

   This allows to combine the Maxwell's equations in a medium straightforwardly, yielding the well-known wave equation. We choose the interface to coincide with the plane z=0 of a Cartesian coordinate system, as sketched in Figure 1.3;

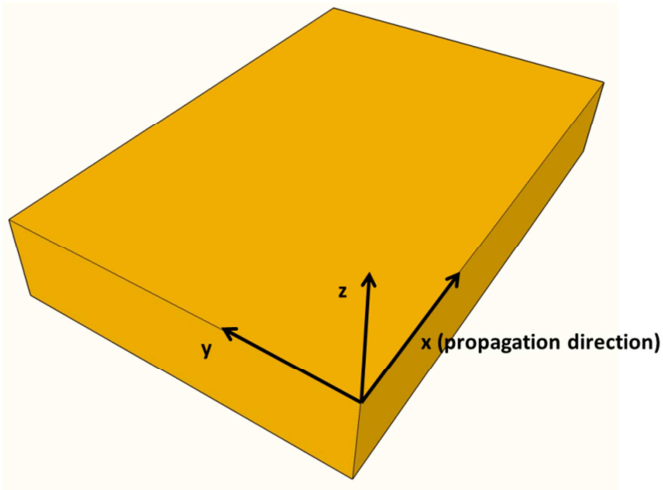

Figure 1.3 Sketch of the SPP-sustaining surface.

2. *We assume in all generality a harmonic time dependence of the electric field.*

   This turns the classical wave equation into the Helmholtz equation $\nabla^2\mathbf{E} + k_0^2\varepsilon\mathbf{E} = 0$, where $k_0=\omega/c$ is the wave vector of the propagating wave in vacuum.
3. *The dielectric profile $\varepsilon(\mathbf{r})$ depends only on one spatial coordinate: $\varepsilon = \varepsilon(z)$.*

[1] The difference lies in the boundary conditions that shall be applied in the two cases. More in general, these boundary conditions allow us to distinguish between bulk, surface and particle plasmons.

With this assumption the wave equation for the interface mode becomes $\frac{\partial^2 \mathbf{E}}{\partial z^2} + \left(\varepsilon k_0^2 - k_{SPP}^2\right)\mathbf{E} = 0$. An analogous equation exists for the magnetic field **H**.

4. *We are looking for interface waves that propagate along the interface in x and show no spatial variation along the perpendicular in-plane direction y*.

   These conditions imply respectively $\frac{\partial}{\partial x} = ik_{SPP}$ and $\frac{\partial}{\partial y} = 0$; with these requirements we can easily solve the wave equation for **E** and **H**. It can be demonstrated that two sets of self-consistent solutions exist, namely TM (or p) modes, having only E_x, E_z and H_y being nonzero, and TE (or s) modes, with only H_x, H_z and E_y being nonzero.

5. *We are looking for bound solutions*, i.e. with evanescent decay in the z direction.

   This implies a dependence $e^{-|k_z||z|}$ for the fields in both media, where k_z is the z component of the SPP wave vector. The spatial confinement of the plasmonic mode can be quantified by $\hat{z} = 1/|k_z|$.

6. *We impose continuity boundary conditions at the interface*.

   For TM modes this yields $\frac{k_{z,1}}{k_{z,2}} = -\frac{\varepsilon_2}{\varepsilon_1}$, where 1 and 2 denote the two media. It means that if one of the media is a dielectric with a dielectric constant $\varepsilon_2=\varepsilon_d$, the real part of the dielectric function of the material in the other half-space must be $\mathrm{Re}[\varepsilon_m(\omega)]<0$. As we have seen in the previous section, metals, especially noble metals such as gold and silver, do have a large negative real part of the dielectric constant. Therefore, **SPPs can exist at the interface between a noble metal and a dielectric**.

Imposing that the magnetic field H_y (for TM modes) satisfies the wave equation, we end up with $k_{z,i} = \sqrt{k_{SPP}^2 - \varepsilon_i k_0^2}$, with *i=d, m*. It can be shown that SPPs are only possible for TM waves.

With these conditions, the famous explicit expression for the SPPs dispersion is obtained straightforwardly:

$$k_{SPP}(\omega) = \frac{\omega}{c}\sqrt{\frac{\varepsilon_d \varepsilon_m(\omega)}{\varepsilon_d + \varepsilon_m(\omega)}} \tag{1.11}$$

In the following we will omit the frequency dependence for simplicity. The dispersion is plotted in Figure 1.4, assuming a Drude model for ε_m.

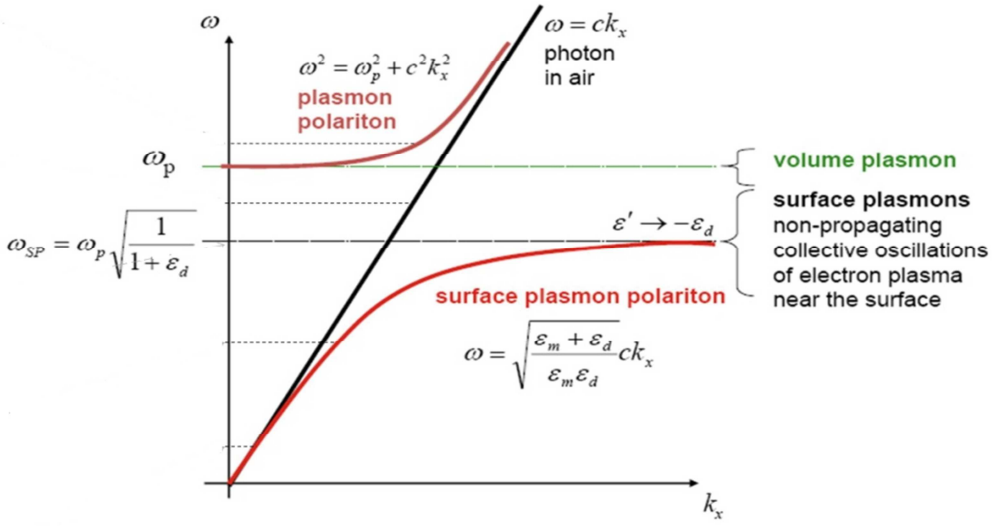

Figure 1.4 SPP dispersion for a single metal-dielectric interface.

The dispersion curve approaches the light line (ω=ck) at small values of k_{SPP} (k_x in the plot), but always to its right, i.e. it has larger momentum than that of free space light for a given frequency. This means that SPPs cannot be excited by simply illuminating a flat metal-dielectric interface with a plane wave; special coupling techniques are required, as shall be discussed in the next section. For these wave vectors, the waves extend over many wavelengths into the dielectric space and the corresponding SPPs are also known as *Sommerfeld-Zenneck waves*. At large values of k_{SPP}, the dispersion curve approaches a certain frequency, known as the Surface Plasmon resonance frequency ω_{SP} , which occurs when $Re[\varepsilon_m] = -\varepsilon_d$. At this frequency, the group velocity of SPPs approaches zero and the density of optical states diverges (in real metals, it only reaches a finite value due to the metal loss).

1.3.2 The length scales of SPPs

So far, we have not discussed the role of the imaginary parts of k_{SPP} and k_z. These imaginary parts account for the losses in the media and thus determine the characteristic length scales of SPPs [32]:

- *SPP wavelength*, $\lambda_{SPP} = 2\pi/Re[k_{SPP}]$;
- *SPP propagation length*, $L = 1/[2 \cdot Im[k_{SPP}]]$;
- *SPP penetration depth in dielectric*, $\delta_d = 1/Im[k_{z,d}]$;
- *SPP penetration depth in metal*, $\delta_m = 1/Im[k_{z,m}]$.

In Figure 1.5 (b), the four length scales for silver and gold are reported; the permittivities are taken from literature [33]. Besides, the real and imaginary parts of the SPP dispersion relations are plotted in Figure 1.5 (a); their knowledge allows to calculate the aforementioned lengths. We notice that they present a back bending and an "S" shape around ω_{SP}. As a matter of fact, although the SPP wave vector tends to diverge for $\omega \rightarrow \omega_{SP}$, its maximum value is limited by losses in metal, accounted in the complex-valued ε_m. As can be seen in Figure 1.5 (b), the scales go from few nanometers for δ_m to hundreds of microns for L.

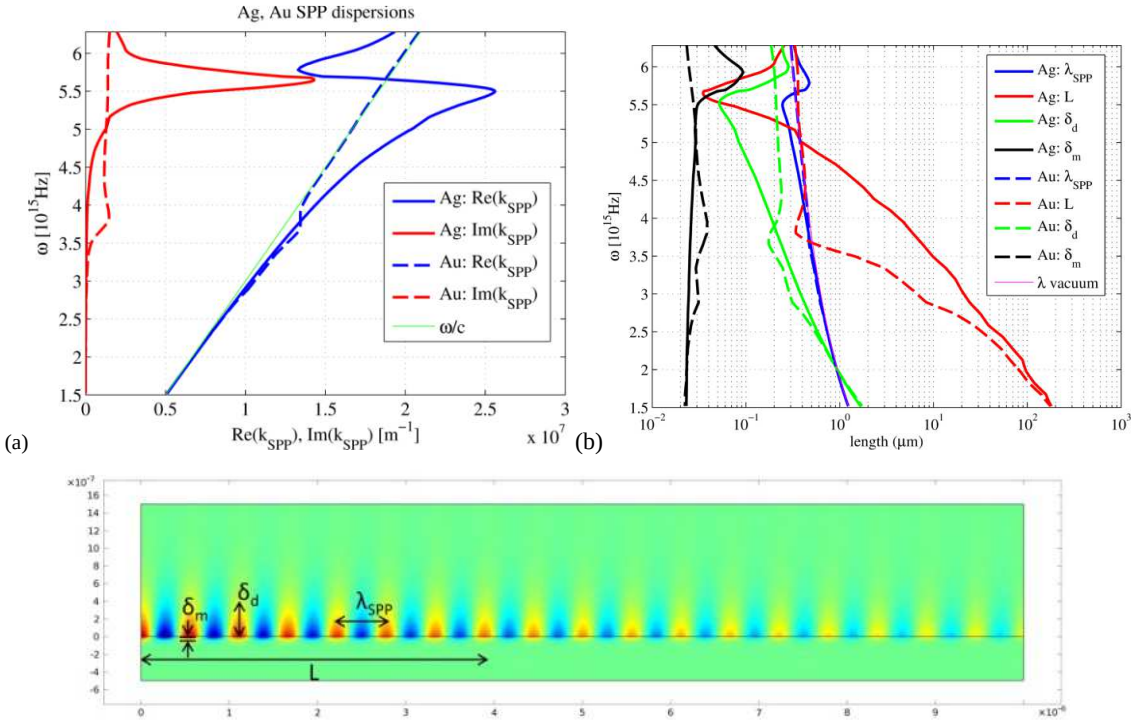

Figure 1.5 (a) Single metal-dielectric SPP dispersion curves in case of gold and silver, dielectric constants are taken from literature [33]; (b) SPP characteristic length scales; (c) SPP H_z field in case of silver and vacuum wavelength λ_0=590nm.

The SPP wavelength λ_{SPP} is relevant from a practical point of view, since it is the length scale to which we have to compare the structures we shall design and fabricate. As can be seen in Figure 1.5 (b), it keeps slightly lower than vacuum wavelength across the whole frequency range. It is worth noting that, when the overlying dielectric is not air/vacuum but some other medium, λ_{SPP} will be reduced in proportion of the refractive index.

The propagation length, L, is also important in practice, since it sets an upper limit on the size for SPP photonic components or waveguides. Its finite value is due to the complex nature of ε_m which results in a complex SPP propagation constant k_{SPP}. We note that L is much larger

than λ_{SPP}. Although it is possible to reach much higher L in the IR range, one should take into account that the increased propagation length is at the expense of field confinement δ_d.

1.4 Excitation of SPPs by light

As already pointed out, the fact that the SPP dispersion curve lies to the right of the light line means that light impinging on the interface from the dielectric cannot couple directly to the SPP modes. The wave vector mismatch between SPPs and radiation thus needs to be overcome in some way. In the following, we will describe *prism coupling* and *grating coupling*, since they will be exploited in this thesis.

1.4.1 Prism coupling or Attenuated Total Reflection (ATR)

This method exploits the phenomenon of total internal reflection in a dielectric with a higher refractive index than the one which shall sustain the SPP. Typical ATR setups are shown in Figure 1.6 (a) and (b) [3]. Configuration (a) is called the Kretschmann-Raether setup. The high-refractive index medium (n_1) is a prism, combined with a thin metal film and a lower refractive index (n_2) dielectric. The working principle can be understood by looking at Figure 1.6 (c), in which we report the light lines in the prism and the dielectric and the dispersions of silver-dielectric and silver-air SPPs. Thanks to the higher prism refractive index, the dielectric-metal SPP dispersion lies to the left of the light line in the prism and momentum matching is therefore possible for some impinging angles θ, according to the relation

$$n_1 k_0 \sin(\theta) = k_{SPP} = k_0 \sqrt{\frac{\varepsilon_m(\omega)}{\varepsilon_m(\omega)+1}} \tag{1.12}$$

In conditions of total internal reflection illumination (where total internal reflection is intended between the prism and the lower index medium), an evanescent wave can tunnel through the prism/metal film and reach the lower-index dielectric, where it may excite SPPs. This wave has enough momentum to efficiently couple to metal-air SPPs.

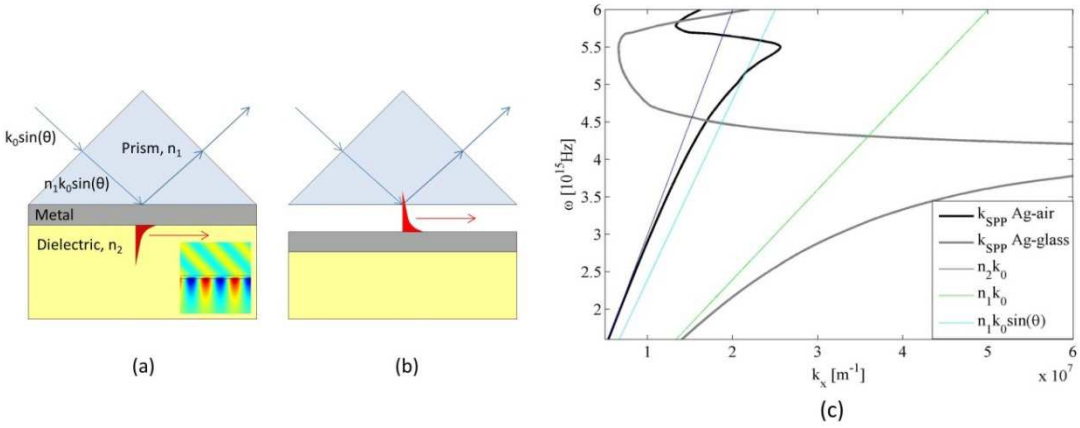

Figure 1.6 ATR coupling schemes, Kretschmann-Raether (a) and Otto (b); (c) SPP dispersion relations at metal-air and metal-prism interfaces compared with light lines in the two dielectrics.

An analogous mechanism is exploited in configuration of Figure 1.6 (b), also termed Otto configuration. In this case, the prism is kept at a sub-wavelength distance from a metal slab, in order to allow near-field coupling.

1.4.2 Grating or diffraction coupling

Another technique to optically excite SPPs is based on the diffraction of incident light by a metallic grating [3, 4, 34], sketched in Figure 1.7 (b). Some diffraction orders can couple to an SPP if the momentum of the diffracted light parallel to the surface equals the propagation constant of the SPP:

$$\mathbf{k}_{\parallel} + n\mathbf{G} = \mathbf{k}_{SPP} \tag{1.13}$$

being $\mathbf{k}_{\parallel}$ the component of the wave vector of impinging light parallel to the surface and $\mathbf{G} = \frac{2\pi}{d}\hat{\mathbf{k}}_x$ the reciprocal lattice vector (d being the period for 1-dimensional gratings). The process can be visualized in Figure 1.7 (a). The yellow region is the light cone. Without any periodic modulation, only the single-interface SPP dispersion curve is present (thick solid lines). In presence of a (shallow) modulation, instead, multiples of the grating crystal vector **G** sum up to the impinging light parallel momentum, allowing to match the required SPP momentum. In an equivalent view, the SPP dispersion curve is shifted by multiples of **G**. Some portions of the "diffracted curves" then fall within the light cone allowing SPP coupling.

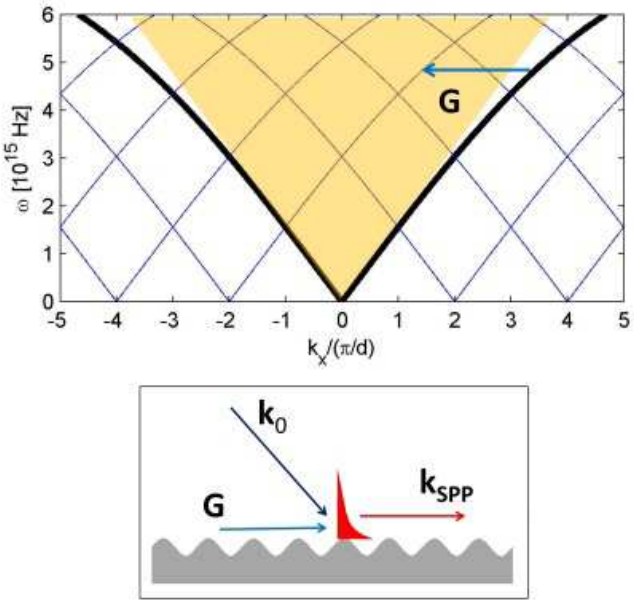

Figure 1.7 Scheme of the grating coupler working principle.

We point out that this is a good approximation only in presence of shallow gratings. The presence of a relevant surface modulation will be discussed in Chapter 2.

1.5 Localized Surface Plasmon Resonance in metal nanoparticles

When a metallic nanoparticle is illuminated by white light, the plasmonic resonance determines the color we observe [35]. This effect was well-known, even if not physically understood, by artist in the Middle-Age, who incorporated tiny gold and silver particles in the stained glasses of church windows to create their beautiful lustrous colors. Another very famous example dates back to antiquity – a Roman cup made of dichroic glass illustrating the myth of King Lycurgus [36].

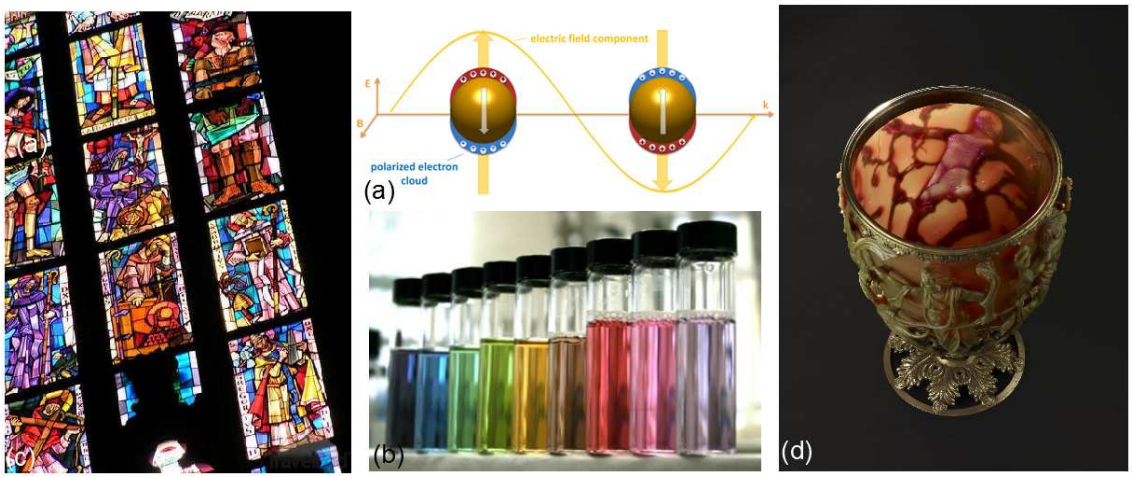

Figure 1.8 Color effects of LSPR in metal nanoparticles. (a) Scheme of the particle resonance excitation. (b) Nanoparticles of various size and shape in solution (photo by Carsten Sönnichsten, http://www.nano-bio-tech.de). The spectral position of the LSPR determines the colour. (c) Stained glass window in the Cathedral of Milan, seen from the inside, and (d) top view of the Lycurgus cup, highlighting the different color observed in reflection (reddish) and in transmission (green). These artistic effects are due to dispersions of metallic nanoparticles or alloys.

This resonance is physically different from the one we have described so far, where *propagating* plasmons were traveling on an infinitely extended metal surface acting as a SPP waveguide. In a finite-sized system, a non-propagating, Localized Surface Plasmon Resonance (LSPR) is observed. The electrons at the particle surface, driven by external fields, are subject to a restoring force exerted by the curved surface of the particle. Therefore, the system can be seen as a forced and damped oscillator and the typical resonance effect occurs. For gold and silver, the peak falls in the visible range.

As we will discuss in the following, the simplest LSPR is the dipole mode of a metal nanoparticle, which has been widely studied and exploited in many applications. Among these, biosensing is probably the most important, since even the slightest change in the dielectric surrounding leads to a detectable shift of the resonance energy.

Before discussing the LSPR, we highlight some differences between that and SPPs.

Surface Plasmon Polaritons	Localized Surface Plasmons
Propagating and dispersive waves	Non-propagating excitations
Need of coupling strategies	Can be directly excited by free space light
1d sub-wavelength confinement	3d sub-wavelength confinement
The excitation strongly depends on the angle of incidence	No angular dependence

Table 1.1 The differences between Surface Plasmon Polaritons (SPPs) and Localized Surface Plasmons (LSPs).

In the beginning of the 20th century, Gustav Mie solved Maxwell's equations for an electromagnetic wave interacting with a sphere [7]. When applying the correct boundary conditions, calculations gave a series of multipole oscillations (dipole, quadrupole, …) for the extinction and scattering cross section of the particle as function of particle radius.

For particles significantly smaller than the free-space wavelength of the incident light, the fields can be considered constant over the particle volume at any instant in time; this assumption is called the *quasi-static* or *electrostatic* approximation. In this regime, only the low-order modes contribute to the extinction and resonance effects can be determined by finding the electrostatic potential for a given geometry and dielectric constant. In formulas, we look for solutions of the Laplace equation $\nabla^2\Phi = 0$, from which we will then calculate the electric field $\mathbf{E} = -\nabla\Phi$.

For simplicity, we consider a spherical nanoparticle of radius *a*, as sketched in Figure 1.9. We denote $\varepsilon_m(\omega)$ and ε_d its dielectric function and the dielectric constant of the (dielectric) medium where it is embedded, respectively. The electric field on the particle can be considered static, $\mathbf{E} = E_0\hat{\mathbf{z}}$.

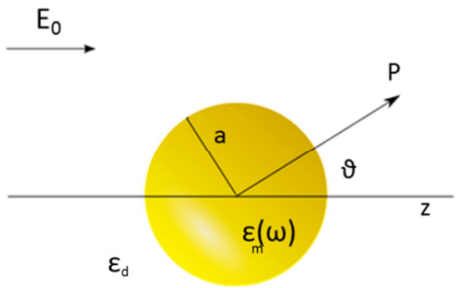

Figure 1.9 Sketch of the LSPR system.

Exploiting the symmetry of the system and applying the boundary conditions at $r \to \infty$ and $r = a$, we obtain [28]

$$\Phi_{\text{in}} = -\frac{3\varepsilon_d}{\varepsilon_m(\omega) + 2\varepsilon_d} E_0 r \cos\theta \tag{1.14}$$

$$\Phi_{\text{out}} = -E_0 r \cos\theta + \frac{\varepsilon_m(\omega) - \varepsilon_d}{\varepsilon_m(\omega) + 2\varepsilon_d} E_0 a^3 \frac{\cos\theta}{r^2} \tag{1.15}$$

We notice that Φ_{in} is constant inside the particle, while Φ_{out} is given by the superposition of the applied field and that of a dipole located at the particle center. This physical interpretation allows us to rewrite Φ_{out} by introducing the dipole moment **p**:

$$\Phi_{\text{out}} = -E_0 r \cos\theta + \frac{\mathbf{p} \cdot \mathbf{r}}{4\pi\varepsilon_0\varepsilon_d r^3} \tag{1.16}$$

With $\mathbf{p} = 4\pi\varepsilon_0\varepsilon_d a^3 \frac{\varepsilon_m(\omega) - \varepsilon_d}{\varepsilon_m(\omega) + 2\varepsilon_d} \mathbf{E}_0$. We can thus say that the applied field induces a dipole moment inside the sphere, proportional to $|E_0|$. Now, if we introduce the polarizability α, defined by $\mathbf{p} = \varepsilon_0\varepsilon_d \alpha \mathbf{E}_0$, we can finally write

$$\alpha = 4\pi a^3 \frac{\varepsilon_m(\omega) - \varepsilon_d}{\varepsilon_m(\omega) + 2\varepsilon_d} \tag{1.17}$$

It is clear that the polarizability experiences a resonance when $\varepsilon_m(\omega) + 2\varepsilon_d$ is a minimum, which, if $\text{Im}[\varepsilon_m(\omega)]$ is small or slowly-varying around the resonance, means

$$\text{Re}\left[\varepsilon_m(\omega)\right] = -2\varepsilon_d \tag{1.18}$$

We immediately notice that quasi-static resonance frequencies are independent of particle size, while they strongly depend on the dielectric constant of the environment, besides of course on the metal itself. Therefore, a gold or silver particle can be used as a sensing element, since its resonance will shift upon local dielectric changes, e.g. due to the specific binding of certain ligands after chemical functionalization of the particle surface. Equation (1.18) is called the Fröhlich condition and is associated to the dipole mode of the LSPR. Figure 1.10 shows plots of the term $\frac{\varepsilon_m(\omega) - \varepsilon_d}{\varepsilon_m(\omega) + 2\varepsilon_d}$, proportional to the polarizability α, for two metals (Ag and Au) and for

different dielectric media (air, water, glass). The data are taken from F.J. García de Abajo, http://nanophotonics.csic.es/static/widgets/eps/index.html.

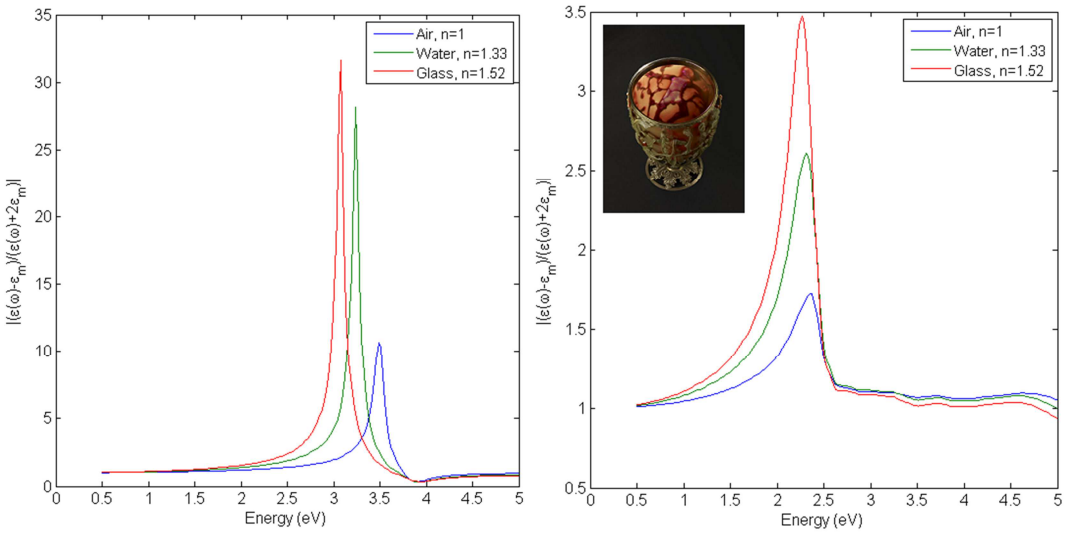

Figure 1.10 Plot of the term $\frac{\varepsilon_m(\omega)-\varepsilon_d}{\varepsilon_m(\omega)+2\varepsilon_d}$, proportional to the polarizability α, for (a) Ag and (b) Au nanoparticles in three different media: air/vacuum (n=1, ε_d=1, blue curves), water (n=1.33, ε_d=1.77, green curves) and glass (n=1.523, ε_d=2.32, red curves). A red shift is observed as the refractive index of the dielectric medium increases. We also notice that the resonances for Au are red-shifted with respect to the same resonances for Ag: they fall in the green spectral region (energy: 2.2-2.3 eV, wavelength: 520-550 nm), while the Ag resonances fall in the violet/UV region. This explains the bright red color of Au nanoparticles observed in transmission.

We notice that the polarizability of an Au nanosphere in the considered dielectrics has a maximum at an energy between 2.2 and 2.3 eV, corresponding to the wavelengths of green (520-550 nm). That is why Au nanoparticles in transmission show the characteristic reddish color also observed in the Lycurgus cup[2].

At resonance, the field is strongly localized near the surface of the particle. An interesting feature is that the electric field inside the particle is homogeneous, as was already pointed out. For metal particles this is an unexpected result, as we know that electromagnetic fields decay exponentially into metals. Consequently, the quasi-static approximation is only valid for particles that are smaller in size than the skin depth of the metal. For larger particles, size-effects are expected and the resonance depends on the particle size.

We now briefly discuss how the theory described above can be generalized.

[2] Actually, in the Lycurgus cup the colloidal nanoparticles form a gold-silver alloy.

1.5.1 Oscillating fields

We must now consider spatial retardation effects over the particle volume. Under plane-wave illumination with $\mathbf{E}(\mathbf{r},t)=\mathbf{E}_0 e^{-i\omega t}$, the fields induce an oscillating dipole moment $\mathbf{p}(t)=\varepsilon_0\varepsilon_d\alpha\mathbf{E}_0 e^{-i\omega t}$, with α given by the electrostatic result. The radiation of this dipole leads to scattering of the plane wave by the sphere, which can be represented as radiation by a point dipole.

1.5.2 Non-spherical particles

We consider an ellipsoid with semiaxes $a_1 \leq a_2 \leq a_3$. In this case we obtain three polarizabilities for the three axes, given by (i = 1, 2, 3) [37]:

$$\alpha_i = 4\pi a_1 a_2 a_3 \frac{\varepsilon_m(\omega)-\varepsilon_d}{3\varepsilon_d + 3L_i\left(\varepsilon_m(\omega)-2\varepsilon_d\right)} \tag{1.19}$$

Where L_i is a geometrical factor depending on a_1, a_2, a_3 and such that $\sum_i L_i = 1$ (for a sphere $L_i = \frac{1}{3}\ \forall i$).

A special case is that of spheroids (ellipsoids having two axes of the same length), that exhibit two spectrally separated plasmon resonances, corresponding to oscillations of its conduction electrons along the major or minor axis, respectively. The resonance due to oscillations along the major axis can show a significant spectral red-shift compared to the plasmon resonance of a sphere of the same volume. Thus, plasmon resonances can be lowered in frequency into the near-infrared region of the spectrum using metallic nanoparticles with large aspect ratio. Lithographic nanorods which we will discuss in the next chapters show a similar behavior, with two distinct peaks, one due to the excitation of a plasmon mode along the long axis of the particle, the other corresponding to a plasmon along the short axis. For the longitudinal excitation, the field-induced charges are separated over a larger distance with respect to a sphere with the same volume. The restoring force is thus smaller and hence the resonance frequency is red-shifted. This issue will be addressed in more detail in Chapter 3.

1.5.3 Non-homogeneous surrounding medium

This is the case, for example, of lithographic particles, which are fabricated on a substrate having, normally, an higher refractive index than the other half-space (usually air). The electromagnetic fields in such an asymmetric environment are different than for a nanoparticle in an homogeneous and isotropic medium, and the resonance can exhibit strong shifts. We distinguish two cases:

DIELECTRICS [38, 39]: In the presence of a dielectric substrate, the nanoparticle plasmon can couple to its image of surface charges in the dielectric, screened by the factor $(\varepsilon_s - 1)/(\varepsilon_s + 1)$, where ε_s is the permittivity of the substrate. Dielectrics with a larger permittivity give rise to a stronger "image" and larger interactions. The effect is a hybridization of the multipolar plasmon modes of the nanoparticle. However, this interaction is usually modeled as an effective refractive index embedding the nanostructure.

METALS [40, 41, 42, 43]: In this case, we have a strongly coupled plasmonic system, with hybridization of LSP of the nanoparticle and the SPPs of the extended metal. The observed energy shift contains both image-like contributions, resulting from the interaction of the nanoparticle plasmons with their images in the metal, and hybridization shifts, resulting from the dynamic interaction between the plasmon modes. Two peaks are actually present, which eventually degenerate in a single peak, with a line shape broader than the single particle resonance.

1.5.4 Particle chains

When two or more LSPR-supporting particles are placed sufficiently close to each other (interparticle distance $d << \lambda$), interparticle coupling occurs, leading to shifts in the spectral position of the plasmon resonance compared to the case of an isolated particle. For small particles, these interactions are essentially of dipolar nature, and the particle ensemble can in a first approximation be treated as an ensemble of interacting dipoles. For closely spaced particles, the particles interact predominantly via their near-field. The direction of the resonance shift can be intuitively understood by considering the Coulomb forces associated with the polarization of the particles. As sketched in Figure 1.11, the restoring force acting on the oscillating electrons of each particle in the chain is either increased or decreased by the charge distribution of neighboring particles. Depending on the polarization direction of the exciting

light, this leads to a blue-shift of the plasmon resonance for the excitation of transverse modes, and a red-shift for longitudinal modes.

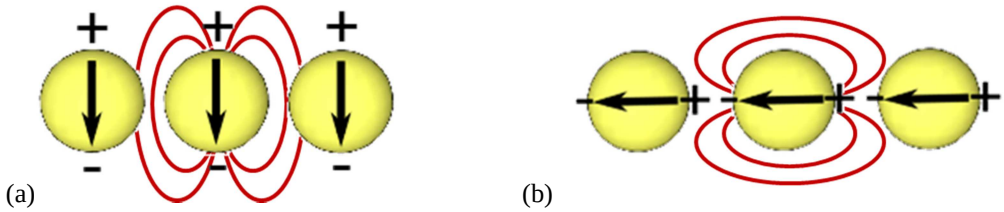

Figure 1.11 Schematic of near-field coupling between metallic nanoparticles for (a) transverse and (b) longitudinal polarization with respect to the particle chain.

For such chains of closely-spaced particles, strong field localization in nano-sized gaps between adjacent particles has been observed [44], suggesting that these system may be good substrates for SERS.

For larger particle separations, far-field dipolar coupling dominates, with a distance dependence of d^{-1}. A detailed description of the properties of complex metal nanoparticle systems can be found in [45].

1.6 Revealing Plasmons

Different techniques have been used to reveal Surface Plasmons; here we give an overview of the ones which shall be used in this thesis. A more detailed description of the specific instrumentation used is provided in Appendix 1.

1.6.1 Surface Plasmon Resonance - SPR

In a typical SPR experiment, a light beam with a certain wavelength λ is shined on a plasmonic substrate and the reflected intensity is measured as a function of the angle of incidence θ [46, 9]. Let us consider the case of a shallow metallic grating. If a *p*-polarized light beam is shined on the surface, it will be almost perfectly reflected if no SPPs are excited. However, if the resonance condition is met and thus a plasmon excitation is set up, a sharp drop of the reflectivity will be observed, since the electromagnetic energy couples to the surface wave and is therefore not radiated back in the far-field. In general, the successful excitation of

SPPs can be deduced from a decrease in the intensity of a reflected (or transmitted) light beam; beside the “angular interrogation” described above, a “wavelength interrogation” (fixed θ, spectral scan) can be adopted. In this thesis, far-field measurements were usually taken using a spectroscopic ellipsometer, described in Appendix 1.

1.6.2 SNOM

To achieve a direct visualization of the plasmonic excitation, the system must be studied with sub-wavelength resolution, which is not achievable with a conventional far-field microscope. A powerful technique to do that is *Scanning Near-field Optical Microscopy* (SNOM), in which a sharp tip, usually a tapered optical fiber, is brought in close proximity of the plasmonic substrate under study and collects photons by coupling the evanescent near field above the surface to propagating modes inside the fiber [47, 48].

The near-field optical tip is often metalized at the end in order to suppress the coupling of diffracted light fields. The resolution of this technique is limited by the size of the tip aperture, which can reach dimensions of only 50 nm. With this technique, it is possible for instance to measure the SPP propagation lengths and in-plane confinement, thus highlighting the trade-off between the two [49, 50, 51]. This technique is used throughout this thesis and Chapter 6 is specifically dedicated to the development of a custom SNOM head.

1.6.3 Fluorescence

Fluorescent emitters such as molecules, quantum dots, or rare earth ions can be placed in a dielectric host close to metal surfaces supporting SPPs. If the frequency of the propagating SPPs lies within the broad spectral absorption band of the emitters, they can be excited via SPP and emit radiation to the far field. This can be collected in a microscope to serve as a measure of the local SPP intensity that is responsible for exciting the emitters. Therefore, SPP propagation on a metal-air interface can be mapped, even if not with sub-wavelength resolution [52]. Of course, care must be taken to counteract non-radiative quenching.

Chapter 2

Plasmonic resonances on digital gratings

2.1 Introduction

We have already pointed out that Surface Plasmons cannot be excited by directly illuminating a flat surface, due to their non-radiative nature [3, 4]. We have overviewed the different strategies which are possible to overcome this limit; one of these is to pattern the metal-dielectric interface with a diffractive grating of period *d* [3, 4, 34]. In this way, one of the diffraction orders of the grating may couple to a plasmonic mode according to (1.13), explicitly

$$k_0 \sin\theta + nG = k_{SPP} = k_0 \Re\left(\sqrt{\frac{\varepsilon_d \varepsilon_m(\omega)}{\varepsilon_d + \varepsilon_m(\omega)}}\right) \tag{2.1}$$

where n=1,2…, α is the angle of incidence, $G=2\pi/d$ the reciprocal vector of the lattice, $k_0 = \omega/c$ the vacuum wave vector of the impinging wave. This simple description, however, holds only as long as the grating can be considered a small perturbation of the flat metallic surface. If the grating is thicker, the response can be more complex.

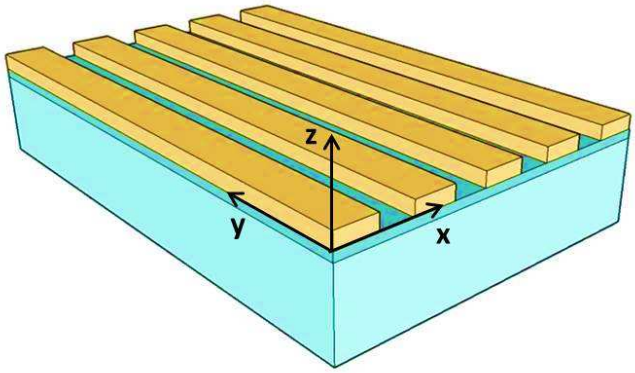

Figure 2.1 Sketch of the 1D digital metallic grating structure. In our structures, a gold grating was fabricated on a transparent glass substrate with a 100 nm –thick ITO layer.

As the starting point of this thesis work, we wanted to study the optical response of a 1D digital metallic grating on a dielectric substrate. Such a structure can be described as a nanomaterial which is uniform in one dimension, e.g. y-direction in Figure 2.1, and periodic in the other dimension (x-direction in the same figure).

In this Chapter, we present a work in which we designed, fabricated and characterized a 1D gold grating, optimized for concentrating electromagnetic (EM) radiation inside the slits. The plasmonic properties of this grating were then exploited for Surface Enhanced Raman Scattering (SERS) applications. This technique, which allows identifying molecules at very low concentrations, is widely used, since the molecular fingerprint information present in Raman spectra makes it specific and quantitative. Moreover, Raman measurements are non-destructive and non-invasive. SERS, which relies on the amplification of the Raman signal induced by suitable metal nano-structured surfaces, allows to overcome a drawback of Raman spectroscopy, which is its lack of sensitivity. However, it is often extremely difficult to perform accurate measurements of the amount of functionalized molecules. To our knowledge, only a few papers have previously computed and measured the SERS enhancement factor [53]. This is due to the combination of several factors related mainly to the geometry of the nanostructures and to the intensity and distribution of the electromagnetic (EM) fields.

An accurate control on these parameters can be obtained by patterning the metal-air interface in a controlled way. Nano-lithography offers a powerful tool to achieve this goal. On the other hand, by choosing simple geometries with a high degree of symmetry, such as digital gratings, it is possible to fully simulate the response of the structures with a relatively short computational time. In this way, we gain a better insight in the field distribution on the metal surfaces.

The approach described in this Chapter for the development of a plasmonic device represents a “flowchart” which was used for the design, fabrication and characterization of all the structures presented in this thesis. The first step was obviously identifying the scientific problem and/or interest concerning a topic and studying the literature. After that, the goal was identifying one or more nanostructures which presented the desired characteristics. Not only the structures should be good candidates to “solve” the scientific problem, but it should be possible at the same time to fabricate them with our tools and characterize them with the techniques available to us. Then, the structures were simulated by numerical analysis, using the commercial software COMSOL Multiphysics, which implements the Finite Element Method (FEM). This step enables us not only to “see what happens”, thus checking if our predictions make sense, but most of all to optimize the geometrical and structural parameters of the structures, as well as carefully choosing the materials for our devices and the experimental conditions. At this point,

the structures were fabricated. Defining the best nanofabrication process (substrates, resists, technique) is a fundamental step, and optimizing the nanofabrication parameters (exposure/development doses/times, metal deposition parameters, …) is crucial. Finally, characterization of the devices was performed.

In the work described in this Chapter, the structure was a digital Au grating, as hinted above. The reason for the choice of such a structure was its simplicity both in simulation and fabrication, which, however, does not limit the efficiency of the device as a SERS substrate. After FEM simulations, a chip with the correct geometrical parameters was fabricated by Electron Beam Lithography (EBL) and electrolytic growth. The SERS enhancement factor of the chip was be measured and compared with the theoretical estimation.

2.2 Resonances in digital metallic gratings

In order to have an insight into the physics of our system we considered a thorough numeric approach using Finite Element Method (FEM) simulations. Figure 2.2 summarizes the response of the grating. We consider only TM-polarized incident light since it is the only polarization which can give rise to SPPs. Different modes are possible:

1) *Cavity mode (CM) resonances*. These resonances result from the multiple scattering of the single propagating mode inside the slits. The mode is partially reflected and transmitted at the slit ends. When the phase difference between the waves transmitted in the substrate is a multiple of 2π, a peak in transmittance is observed, like in a Fabry-Perot resonator. When this resonance takes place, a great fraction of the incident light is funneled within the slits and is transmitted in the substrate, resulting in what is called Extraordinary Optical Transmission (EOT) [54].

2) *Surface Plasmon Polariton (SPP)* resonances. They are excited in a 1D grating when the in-plane component of the incident *p*-polarized radiation and that of the scattered waves sum up to match the SPP momentum, following equation (2.1). This kind of resonance is associated to a transmittance extinction and to a high field enhancement in proximity of the grating (hundreds of nm in silicon) [55].

3) *Wood-Rayleigh anomalies* (WR). Abrupt changes in transmittance as a function of period are observed in configurations for which a diffraction order lies in the plane of the grating, i.e. at periods $d_n = n\lambda/N$, being N the refractive index of the dielectric medium. WR anomalies are not resonant phenomena but are rather due to pure geometrical reasons and are fully independent of CM and SPPs [56].

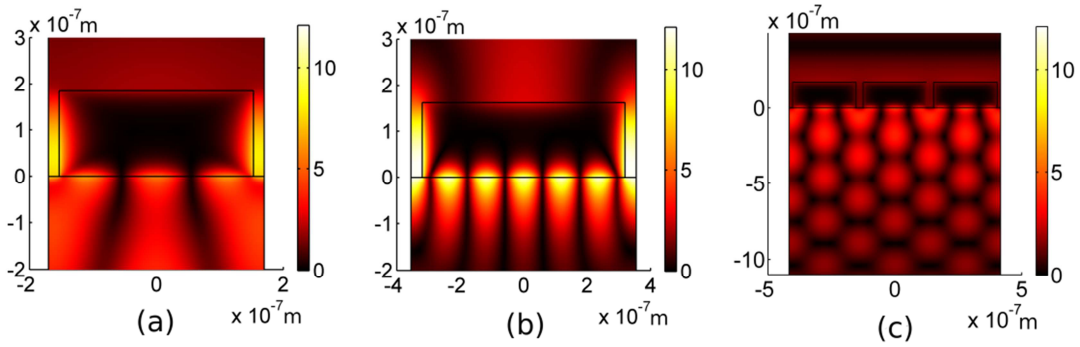

Figure 2.2 Magnetic field norm in a unit cell of a digital grating. (a) CM-resonance; (b) SPP-CM resonance; (c) WR-CM resonance.

It is worth noting that CMs are *local* resonances, since they would appear as well in a single illuminated slit without any periodicity [57]. On the other hand, SPPs are *global* resonances since they can exist thanks to the coherent periodicity of the structure [3]. As many authors pointed out, however, CMs and SPPs are not independent each other [58]; actually, one should better speak of a hybrid mode which presents both CM and SPP resonant characteristics. On the other hand, the EOT efficiency is greatly enhanced in presence of a periodic structure [54, 58].

2.3 Design

2.3.1 Materials

The substrate was an Indium Tin Oxide (ITO)-coated glass slide (Sigma-Aldrich, ITO thickness: 100 nm, resistivity: 15-25 Ω/sq, linear formula In_2O_3 $(SnO_2)_x$). Indium tin oxide is a highly degenerate *n*-type semiconductor with a wide band gap (3.5–4.3 eV) [59, 60]; it exhibits high transmission in the visible region, high reflectance in the infrared region and high electrical conductivity (2500–5000 Ω^{-1} cm^{-1}) [59]. Due to these unique properties, ITO has been used in a wide range of applications including light-emitting diodes (LEDs) [61, 62], gas sensors [63], antireflection/antistatic coatings [64] and flat panel displays [59, 65]. In our case, transparency was required since the characterization would be performed in transmission; on the other hand, conductivity is preferred in order to avoid surface charging inside the EB system, and is also needed to perform electrolytic growth.

The material constituting the grating must be a noble metal; the choice usually falls on silver or gold. In this case, even if both metals provide a plasmonic resonance at the desired

wavelength (633 nm), gold was chosen since it does not suffer oxidation. The simulation also takes into account a thin (2 nm) dielectric layer of a non-absorbing material conformal to the plasmonic grating surface profile, resembling the benzenethiol layer used for functionalization.

2.3.1 Plasmonic properties

The structures were designed in order to obtain a Cavity Mode resonance inside the slits. A scheme of the simulated structure is shown in Figure 2.3. In order to minimize the computational time, perfect periodic boundary conditions were imposed, and calculations were made for one period only. The dielectric constants of the different layers were taken from ellipsometric data, which were obtained directly from the samples used for the experiments. The gold grating was illuminated from the air side at normal incidence with TM polarization. In principle, the EM field distribution depends on all the geometric parameters: metal thickness (h), slits width (a), and period (d). In our simulations, the duty cycle (slit width/period ratio) was fixed to 40% in order to have a large zone of active SERS surface, while slit width and period were taken as the parameters to be optimized.

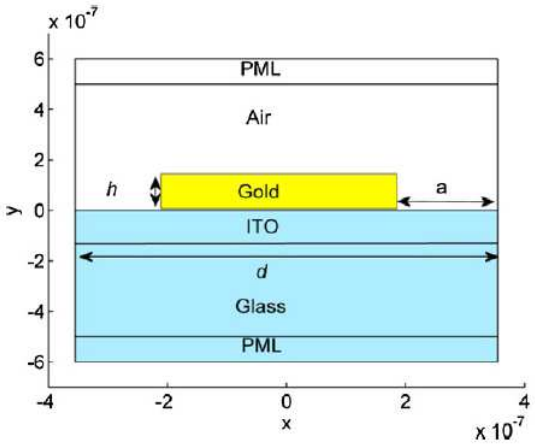

Figure 2.3 Sketch of the FEM model.

In order to obtain useful information about EM field configuration, far field quantities, such as reflectance, transmittance and absorbance were evaluated as a function of period and thickness; this is shown in Figure 2.4 (a) and (b). As can be clearly seen, a periodic pattern in the maps is present. The areas of minimum reflectance and maximum metal absorbance correspond to Fabry–Perot resonances excited by plasmonic effects. Looking at the maps, these two conditions are verified for a gold thickness (h) of 100, 350 and 600 nm, and up to a grating period (d) of 400 nm. The chosen parameters were period d=300 nm and thickness h=350 nm.

The other possible values for the thickness presented hot spots that are not well localized (h = 100 nm) or have a lower intensity (h = 600 nm). In Figure 2.4 (c) the optimized EM field configuration for TM (right) and TE (left) polarization are shown. It clearly appears that TE polarization is forbidden to penetrate the trances of the slits. On the contrary in TM polarization the EM generates a plasmonic standing wave.

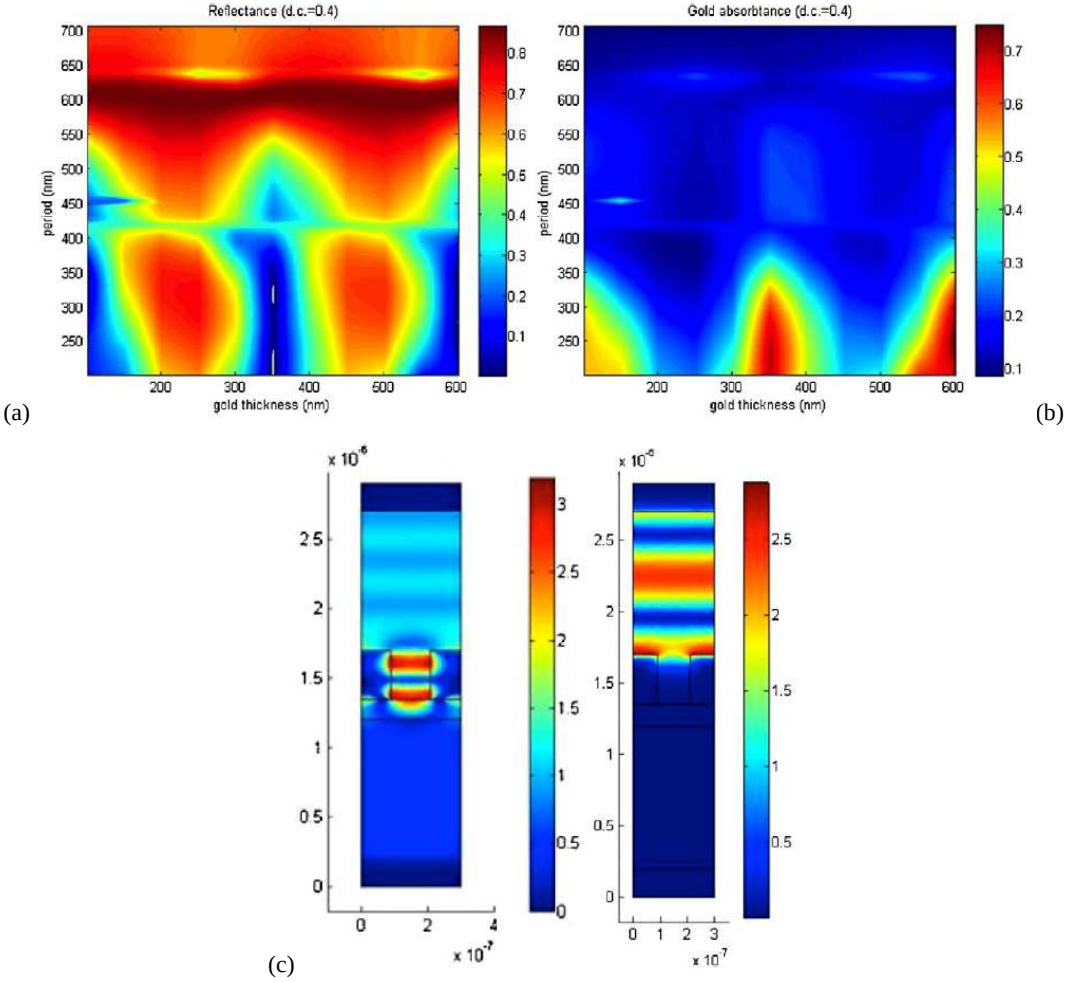

Figure 2.4 Maps of (a) reflectance and (b) absorbance in the gold layer as a function of period and thickness. The areas corresponding to plasmonic excitations lie in the period range 200–400 nm and in metal thickness range 320–380 nm. (c) Optimized field configuration for TM polarization (left; d = 300 nm, h = 350 nm, a = 120 nm) and TE polarization (right). In the latter case, the EM field is not localized inside the slits.

2.4 Fabrication

As pointed out in the previous sections, a precise control on the geometry of the grating is needed in order to obtain hot spots inside the slits. This is ensured by the chosen fabrication

process, which consists of two main steps. First of all, Electron Beam Lithography (EBL) was performed on the ITO/glass substrate by using a JEOL EBX-6300FS EBL system operating at 100 keV, with a current of 2 nA. The substrate was previously spin-coated with a 490nm-thick PMMA resist layer and soft baked at 180°C on a hot plate for 10 minutes. A dose of 1200 $\mu C/cm^2$ was used for the exposure. An area of 2 mm x 2 mm was patterned on the surface. Although a smaller area could be fabricated, samples with large and uniform SERS-active surfaces can be more easily implemented in practical devices. After the exposure, the sample was developed in a methyl-isobutyl-ketone (MIBK) solution diluted with isopropyl-alcohol (IPA) (volume ratio: MIBK:IPA = 1:3) for 30 s at room temperature, and rinsed in pure IPA. The metallic structures were obtained by electrolytic growth. The electrolytic bath used in the process was the commercial solution Karatclad™ 265 HS, with 4.5 nominal pH. The growth parameters were deposition temperature 36° C, growth current 100 mA, voltage 2.9 V and growth time 45 s. The growth rate was calibrated to be 3.3 nm/s. In Figure 2.5 (a) a fabricated grating is shown.

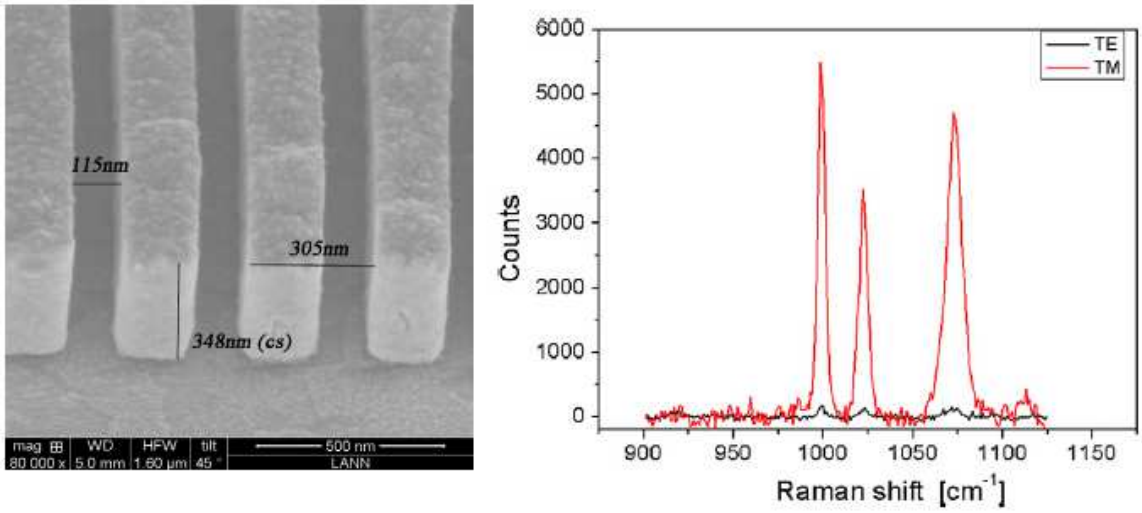

Figure 2.5 (a) SEM picture of the optimized fabricated structure. (d) SERS spectrum (TM-pol: red, TE-pol: black) upon functionalization with benzenethiol.

2.5 Experimental results

SERS measurements were performed with a Renishaw micro-Raman instrument employing a 50x microscope objective and the 632.8 nm line of a He–Ne laser. Spectra were acquired with different laser polarizations, obtaining either the transverse magnetic (TM) or transverse electric

(TE) mode. The SERS enhancement factor is determined by recording the SERS signal of a benzenethiol (BT) monolayer adsorbed on the nano-patterned surface.

BT presents an intense Raman signal at 992 cm^{-1}, corresponding to the breathing of the benzenic ring, with a well-known Raman cross-section [66]. The experimental SERS substrate enhancement factor (SSEF) can be evaluated by using the formula:

$$EF = \frac{I^{SERS,BT}}{I^{RS,BT}} \frac{C_V^{BT} H_{eff}}{C_S^{BT}} \frac{\sigma_{Toluene}}{\sigma_{BT}} \frac{1}{A} \tag{2.2}$$

where I is the Raman signal intensity of the molecule monolayer absorbed on the metal surface (SERS) and the liquid used as reference (RS), CV and CS are the volumetric and packing density of the reference liquid and the BT adsorbed, H_{eff} is the collection efficiency of the experimental set-up, σ is the Raman differential cross section and A is the ratio between the patterned area and a flat one. As the reference liquid we used toluene instead of benzenethiol, for technical reasons. The volumetric density of toluene and the packing density of benzenethiol are known from literature: CV = 5.69 x 10^{21} molecule/cm^3 and CS = 6.8 x 10^{14} molecule/cm^2 [67, 68, 69]. The ratio $\sigma_{Toluene}/\sigma_{BT}$ was measured to be 0.56. Figure 2.5 (b) shows SERS spectra of BT: the Raman signal recorded with TM polarization is much more intense than the one recorded with TE polarization, as foreseen by simulations.

The experiment is characterized by the possibility to compare the SERS intensity I_{SERS} for the two polarizations, without changing any other experimental parameters. Therefore, we considered the parameter R=[$SSEF_{TM}/SSEF_{TE}$] and compared its theoretical value with the experimental one, obtained by evaluating (2.2) in the TM and TE conditions and taking their ratio. This yields

$$\mathrm{R}_{\exp} = \left[\frac{SSEF_{TM}}{SSEF_{TE}} \right]_{\exp} = \left[\frac{I^{SERS,BT}}{I^{RS,BT}} \right]_{\exp} \tag{2.3}$$

since all the other factors except for the I_{SERS} and the I_{RS} contribution are eliminated in the ratio.

A similar reasoning can be applied for the theoretical value. In principle, the SERS EF for a specific molecule on a specific substrate can be computed by spatially averaging the EF of a single molecule, $M_{Loc}(r,\omega_L)\, M_{Loc}^{PW-P}(r,\omega_R)$, over the entire metallic surface:

$$SSEF^P = \left\{ M_{Loc}(r,\omega_L) M_{Loc}^{PW-P}(r,\omega_R) \times \left[T\left(\alpha_N, \mathrm{e}_{Loc}(r,\omega_L), e_{Loc}^{PW-P}(r,\omega_R)\right) \right] \right\} \tag{2.4}$$

Rigorous definitions about the terms in (2.4) are provided in [66]. The curly brackets denote spatial averaging while the square brackets represent the averaging over allowed molecular orientations. $T(\alpha_N, e_L, e_R)$ is the surface selection rules factor, which couples the excitation and re-emission problems through the normalized Raman polarizability tensor (characterizing the symmetry of the Raman tensor and the molecular orientation). Basically, the total SERS enhancement factor is due to two multiplicative factors: the electromagnetic *M* factor and the chemical one [66]. The *M* factors can be computed taking into account the field distribution provided by the simulation code within the $|E|^4$-approximation [66]. On the contrary, the contribute in the square brackets is independent on the EM field; it depends only on the orientations of the molecules on the surface of the grating, and it is eliminated when we compute the ratio between the TM and TE values.

A match between the experimental and theoretical ratio was found, as reported in Table 2.1. The error associated to the experimental SSEFs is calculated from experimental data collected on different regions on the sample and it gives an estimation of the homogeneity of the device.

Theory			**Experiment**		
EM EF_{TM}	*EM* EF_{TE}	***R***	*SSEF* EF_{TM}	*SSEF* EF_{TE}	***R***
6,43 (A=4,2)	0,17 (A=4,2)	**37,43**	245,67±9,82	7,51±1,51	**32,68±6,52**

Table 2.1 Comparison of the theoretical and the experimental EFs. EM EF_{TM} and EM EF_{TE} are evaluated in the $|E|^4$-approximation. Experimental SSEFs are evaluated using (2.2). R is the ratio defined in (2.3).

2.6 Conclusions

We designed, fabricated and characterized a digital gold grating supporting a plasmonic resonance with hot-spots inside the slit, called Cavity Mode resonance. This excitation differs from the classical Surface Plasmon Polariton and has a local character.

The structure was designed with the help of FEM simulations. Its geometry was optimized and proper materials were chosen. The grating was then fabricated by Electron Beam Lithography followed by electrolytic growth; the fabrication process also required optimization and an accurate choice of all the variables. The device was then used for SERS applications. Its Enhancement Factor was calculated both theoretically and experimentally and a good match was found between the two.

The approach described here provides a way to gain good control of the SERS phenomenon and its Enhancement Factors (EFs). In fact, despite the high potential demonstrated by the

SERS technique, it is often difficult to obtain a controllable and reproducible EF due to uncertainties in the surface geometry and the electromagnetic fields distribution. On the contrary, thanks to accurate FEM simulations and powerful and reliable fabrication techniques, we were able to foresee the behavior of the device in a satisfactory and promising way.

This result is a good starting point for tailoring the properties (like field distribution) of more complex nanostructures, which can be optimized and exploited for different applications.

Chapter 3

We go small: localized plasmon resonances on gold nanorods

3.1 Introduction

In recent years, an increasing interest has arisen around the possibility of engineering of the near-field localization properties of nanostructures supporting LSPR [70, 71, 72]. In fact, a properly designed structure offers unique opportunities to build integrated optical devices with sub-wavelength localization of light [73] and plays a key role in developing more efficient sensors [74], optical antennas [75], and nanofocusing elements [76]. The resonant optical response of metallic nanoparticles can be largely tuned by a careful design of the particle morphology and/or by arranging the particles in a convenient fashion [77, 78, 79, 80].

Structures such as bowties [74], nanodisks [81], nanocubes [82], nanostars [83], nanorods/wires [84, 85] and nanoshells/nanorings [86, 87] have been investigated recently. Such structures are sometimes called nanoantennae for their ability to couple propagating light to strongly localized electromagnetic fields [88, 89, 85, 90]. In particular, it has been demonstrated that plasmonic dimers, i.e. nanoparticle pairs separated by sub-wavelength gaps, give rise to highly concentrated electromagnetic fields in the gap region [81, 91, 92]. This makes these structures particularly interesting for many sensing techniques [93] and in particular for SERS, since they can efficiently funnel optical radiation into nanometer-sized volumes and thus boost the Raman cross-section of molecules attached to their surface by several orders of magnitude [94, 95, 96].

We have already remarked that LSPR can be tuned over a wide range via a careful choice of nanoparticle size, shape, materials and arrangement. Therefore, it is crucial to rationally design reproducible plasmonic nanoparticle arrays, capable of producing the highest field enhancement at well-defined locations and targeted frequencies [97, 98].

For many years, technological limitations have strongly slowed down the development of LSPR-based techniques. In particular, most of the proposed SERS substrates exploited chemically roughened surfaces [23, 24] or colloids [95], which of course support LSPR but do not provide the high degree of control needed to effectively tune and control the resonance. In

the last decade, however, the advancement of modern nanofabrication techniques such as EBL has removed this main limit and opened up the possibility to fabricate lithographic nanoparticles with arbitrary as well as controllable and reproducible shape, size and arrangement.

The choice of a suitable nanoantenna geometry requires great attention. In our case, we chose periodic arrays of nanorod-shaped particles fabricated by EBL on top of an ITO coated glass slide. By “nanorods” we mean planar rectangular nano structures with rounded ends, which can be viewed as elongated disks; they can be considered the “planar version” of the ellipsoids discussed in Chapter 1 and they exhibit similar properties, even if we have to take into account effects due to the anisotropy of the system. The planar nanorod geometry was chosen for the following reasons:

a) Due to their shape, nanorods exhibit a large anisotropy with respect to the polarization direction. If the polarization is parallel to the long axis, the observed resonance is red-shifted, has a smaller linewidth and a higher intensity with respect to nanodisks/nanospheres of the same volume (see Figure 3.1). The short axis mode is blue-shifted, broader than the long-axis resonance, and weaker. Moreover, non-radiative damping is reduced and the scattering efficiency is increased in nanorods as compared to nanospheres of the same volume.

b) Their high degree of symmetry makes them easy to simulate and fabricate.

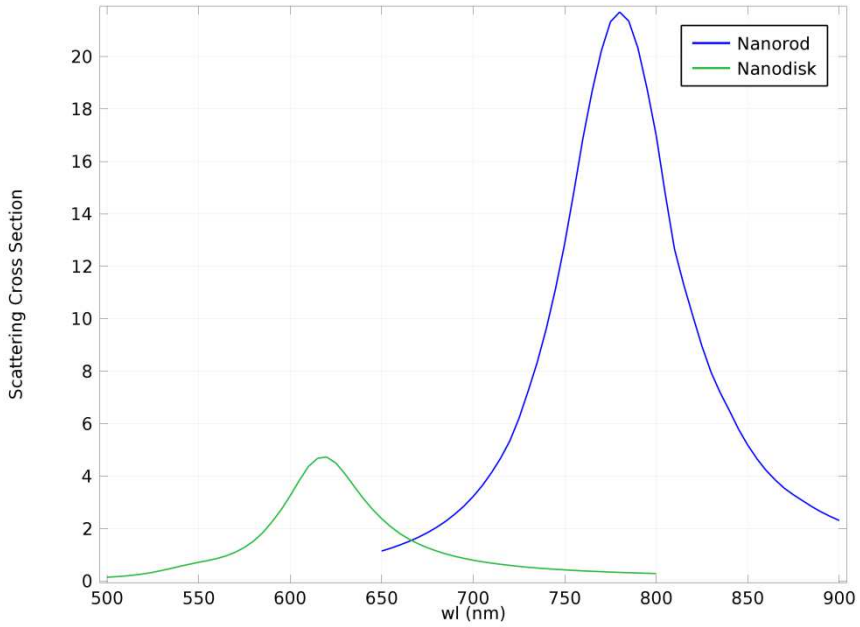

Figure 3.1 Comparison between the LSPR resonance of a nanorod and a nanodisk of the same volume. Light polarization is set along the nanorod major axis. It can be easily seen that the resonance of the nanorod is red-shifted and higher.

In this work, we designed, fabricated and characterized coupled nanorod arrays in order to exploit their localized resonances for SERS. As discussed in the previous Chapters, SERS is a powerful analytical technique, since it enables molecules to be identified from their vibrational spectra at very low concentrations. An even higher response can be envisaged by combining LSPR with coherent Raman techniques such as Coherent Anti-Stokes Raman Scattering (CARS), for which the possibility of enhancing the signal by means of plasmonic nanostructures is far from being an established approach [99].

First of all, we discuss the parameters which affect the resonance, in order to define precise guidelines for the design of our nano-material. These parameters include both geometrical variables (length, width, gap width, thickness) as well as considerations about the materials to be employed for the particle and for the substrate.

We will then discuss the design of the nanorods, which was performed using numerical simulations based on the Finite Elements Method. This study showed different possible solutions among which we chose the most suitable one for our experiments. The optical properties of the optimized structure will be discussed, with particular regard to the polarization dependence and the estimation of the enhancement factor.

The fabrication will then be described thoroughly, highlighting the experimental issues we had to deal with and the final strategy we chose. Finally, the SERS experiment will be presented, together with its experimental enhancement factor which shall be compared with the calculated one.

Recently, we have started a collaboration with Politecnico di Milano about exploiting these structures for Surface Enhanced CARS, or SECARS. Preliminary results will be shown and discussed at the end of this Chapter.

3.2 Parameters affecting the resonance

As hinted above, our LSPR substrate consists in a double-periodic array of rod-shaped nanoparticles, fabricated on top of an ITO-coated glass slide; the array configuration was chosen to obtain a large number of hotspots in a small area. The nanorods are oriented with their major axis along *y* and they are coupled, being separated along the major axis by a small gap. To obtain a resonance inside the gap, the polarization is set along *y*. A sketch of the device is reported in Figure 3.2.

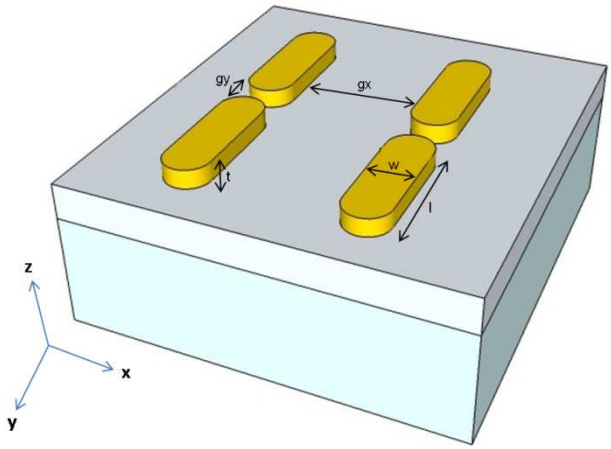

Figure 3.2 Sketch of the nanorod array geometry, which consists in Au nanorods fabricated on top of an ITO/coated glass slide. Four unit cells are shown.

We will now briefly discuss how the different geometrical parameters of the array affect the LSPR of the nanorods. These parameters are:

- Nanorod length (l);
- Nanorod width (w);
- Nanorod thickness (t);
- Gap along the nanorods major axis, parallel to the *y* direction (g_y);
- Gap along the nanorods minor axis, parallel to the *x* direction (g_x).

The first three parameters affect the resonance of the single nanorod. In particular, the length of the nanorods is the main parameter determining the spectral position of the resonance, i.e. the wavelength at which a nanorod can be excited. Increasing the length of a nanorod, a red-shift of the resonance is observed, as shown in Figure 3.3 (a). On the contrary, a blue-shift of the resonance is observed when the width of the nanorods is decreased while keeping the length fixed, i.e. with increasing aspect ratio l/w (Figure 3.3 (b)). The resonance also blue-shifts as the thickness of the nanorod is increased (Figure 3.3 (c)).

The values of the gaps, on the contrary, influence the specific properties of the array. As the gap along y is decreased (i.e. the structures are “more coupled”), the resonance is red-shifted and its intensity is increased (Figure 3.3 (d)). Actually, the red-shift is not so big until the gap is larger than ≈ 10 nm. Strong-coupling effects leading to large red-shifts and huge enhancements are observed for gap amplitudes below this value. However, we will not enter this regime, as discussed in the following. The variation of the gap along x is not so crucial with our polarization setup. However, if the particles are too near along the minor axis, a lowering of the resonance intensity is observed, due to lateral cross-talk of the particles.

In Figure 3.3 we report a study as the above-mentioned parameters (length, width, thickness and gap width along y) were varied. These results have been considered in the design of our structures.

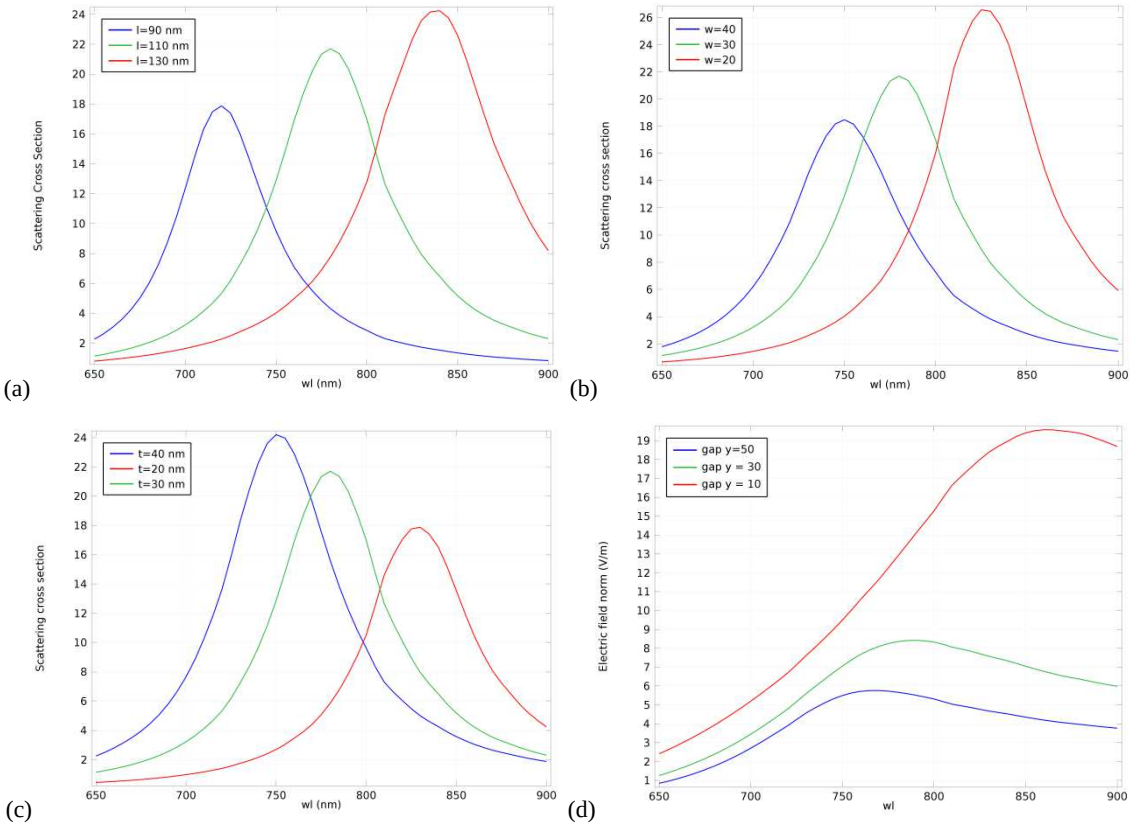

Figure 3.3 Spectral position of the LSPR resonance as different parameters of the geometry are varied. (a) As the nanorod length is increased, the resonance red-shifts. (b) As the width is decreased (i.e. the aspect ratio is increased), the resonance red-shifts. (c) As the nanorod thickness is increased, the resonance blue-shifts. (d) As the gap along the major axis becomes narrower, the resonance red-shifts and its intensity increases.

We now consider the materials which can be used to fabricate the nanorods; we discuss in particular the choice of the metal supporting LSPR. As said many times, Ag and Au are the most common plasmonic materials. Although the plasma frequencies for both metals are comparable, the corresponding LSPR mode of a nanorod-shaped particle with the same size occurs at different wavelengths: the deviation originates from the additional contribution of the interband electronic transitions to the dielectric function. In the case of the Au nanoparticle, the resonance occurs at higher wavelengths as compared to the one for Ag, as shown in Figure 3.4. Keeping this fact in mind, we started by choosing Au as our plasmonic metal, due to its higher stability.

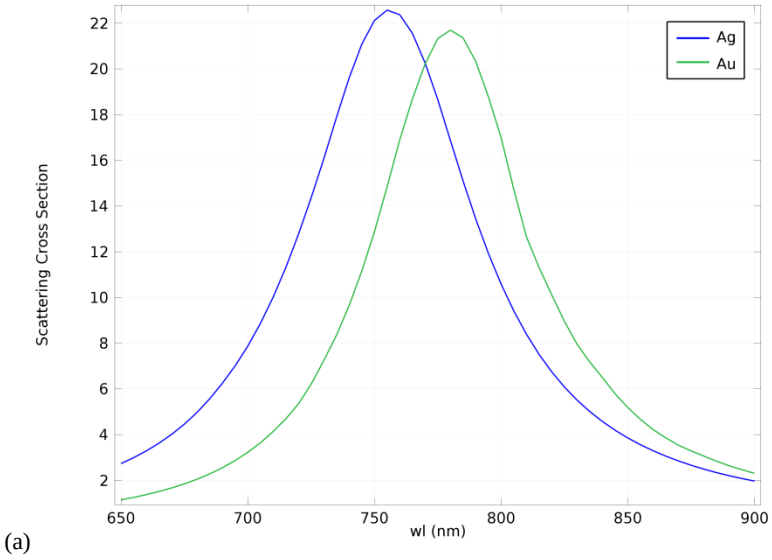

(a)

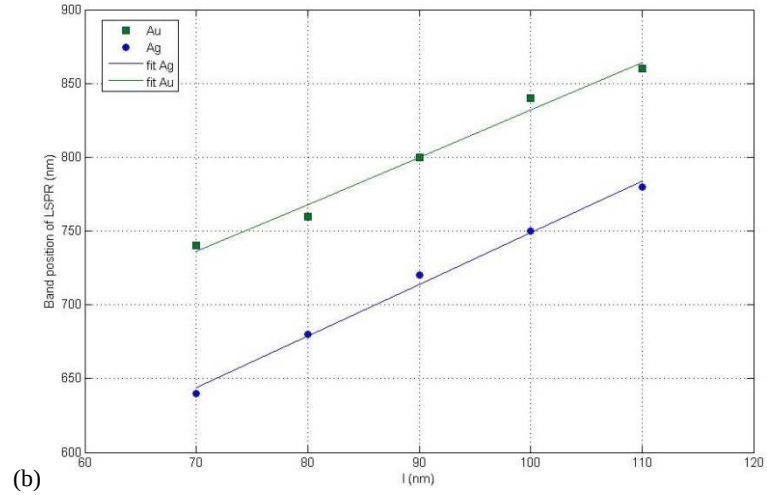

(b)

Figure 3.4 Comparison between the LSPR resonance (shown is the scattering cross section) of a single Au (green line) and Ag (blue line) nanorod with the same dimensions. (a) Spectral position of the resonance for an array made of nanorods having l=110 nm, w=35 nm, t=30 nm, g_y=30 nm and g_x=165 nm. (b) Band position of the LSPR as a function of l for the two materials. The LSPR of Au nanorods is clearly red-shifted.

3.3 Design

To investigate the behavior of the system as a function of the geometric parameters and the materials involved, we performed FEM simulations using the commercial package COMSOL Multiphysics. We have seen in Section 2 that many parameters are affecting the LSP resonance of lithographic nanoparticles. In the case of nanorods, the parameters which determines the spectral position of the resonance is length; nanorod thickness and width also play a role in the optimization of the structure, while the effect of the amplitude of the gaps is to adjust the resonance intensity and cause a slight red- or blue-shift. We therefore decided to keep the gaps

fixed. Along the major axis, g_y was set to 30 nm to obtain high field enhancement as well as lithographic reproducibility. Moreover, this can be seen as a trade-off between high enhancement and the necessity to avoid the "four-wave-mixing" effect (occurring at $g_y < 30$ nm) [100], which is a competitive effect for applications such as SECARS. Along the short axis, we set a period of 200 nm. To optimize the nanorod geometry, instead, we (a) optimized its length using FEM simulations while keeping all the other parameters fixed, (b) adjusted the width and thickness once length was optimized, thus fine-tuning the antenna. For nanoparticle arrays intended for SERS or SECARS, a suitable variable to be observed to determine the best geometric parameters was the electric field norm in the gap. To evaluate it, we considered its average on a three-dimensional region inside the gap; this allows to smooth out possible singularities due to the meshing of the specific simulated geometry. The calculated vales were then normalized to the incident field at the same place.

Initially, we tried to optimize our structures for λ=633 nm, available in our lab. The structures were illuminated from the air side and light polarization was set along the nanorods major axis. The metal was gold, deposited by electrolytic growth; its optical constants were measured by ellipsometry and implemented in the simulations. The substrate was an ITO-coated glass slide; the thickness of the ITO layer was 100 nm. As initial values in the simulations, we set 30 nm for both width and thickness, since similar values are used for nanoantenna structures in literature. We found a resonance for a length of 30 nm. In Figure 3.5 we report the spectral dependence of the electric field norm in the middle of the gap.

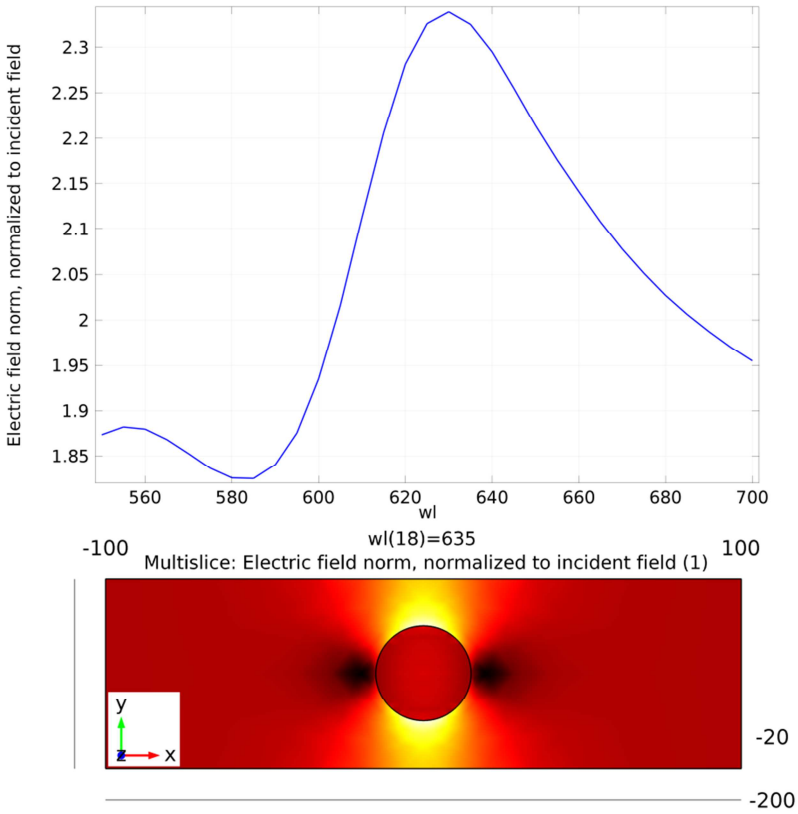

Figure 3.5 Spectral dependence of electric field norm in the middle of the gap, for an array of Au nanorods with l=w=t=30 nm, separated by a gap of 30 nm. Inset: plot of the electric field norm in a unit cell for the optimized geometry (slice at half thickness).

With these parameters, the rod is actually a nanodisk, thus losing the interesting properties shown by the nanorods due to their higher aspect ratio, discussed above. Moreover, the enhancement factor for the electric field norm is relatively low (a factor 3). To obtain a better resonance on a "proper" nanorod structure, we therefore tried to use silver, which should have a blue-shifted resonance for a given nanorod length, as suggested from the study reported in Section 2. We repeated the simulation with the same parameters, just changing the metal from gold to silver, obtaining a resonance for a length of 70 nm. Width and thickness were also fine-adjusted and their best values actually turned out to be 30 nm. We report the spectral dependence of the electric field norm in the middle of the gap in Figure 3.6; the inset shows the electric field norm in a unit cell for the optimized geometry. A resonance is clearly set on at the nanorods ends and inside the gap.

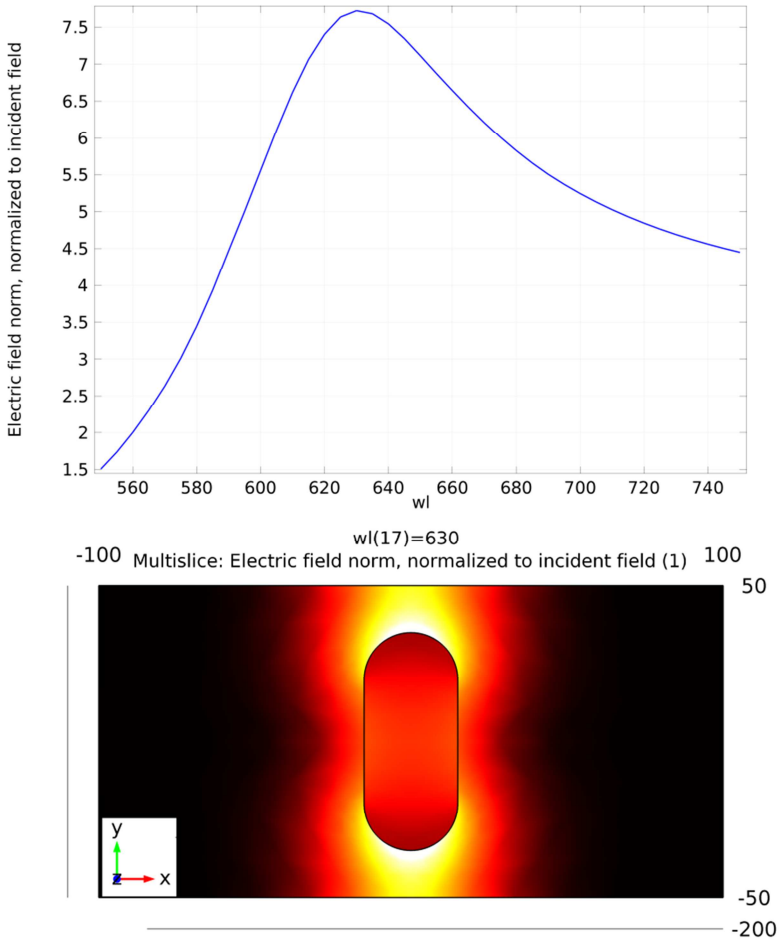

Figure 3.6 Spectral dependence of electric field norm in the middle of the gap, for an array of Ag nanorods with l=70 nm and w=t=30 nm, separated by a gap of 30 nm. Inset: plot of the electric field norm in a unit cell for the optimized geometry (slice at half thickness).

Although these configuration provides the desired resonance, we still prefer to use Au as the LSPR-supporting metal, since it does not suffer oxidation. A possible solution is to switch to an higher wavelength, for which a resonance should exist, for gold particles, at higher values of *l*. We chose λ=780 nm since it is widely used in literature and it is available in many characterization laboratories. Thinking of our structure as a SERS substrate, 780 nm is therefore our "pump" wavelength. The optimal nanorod length turned out to be 95 nm, while both width and thickness are 30 nm. Figure 3.7 shows the spectral dependence of the electric field norm in the middle of the gap, together with a plot of the electric field norm in the unit cell.

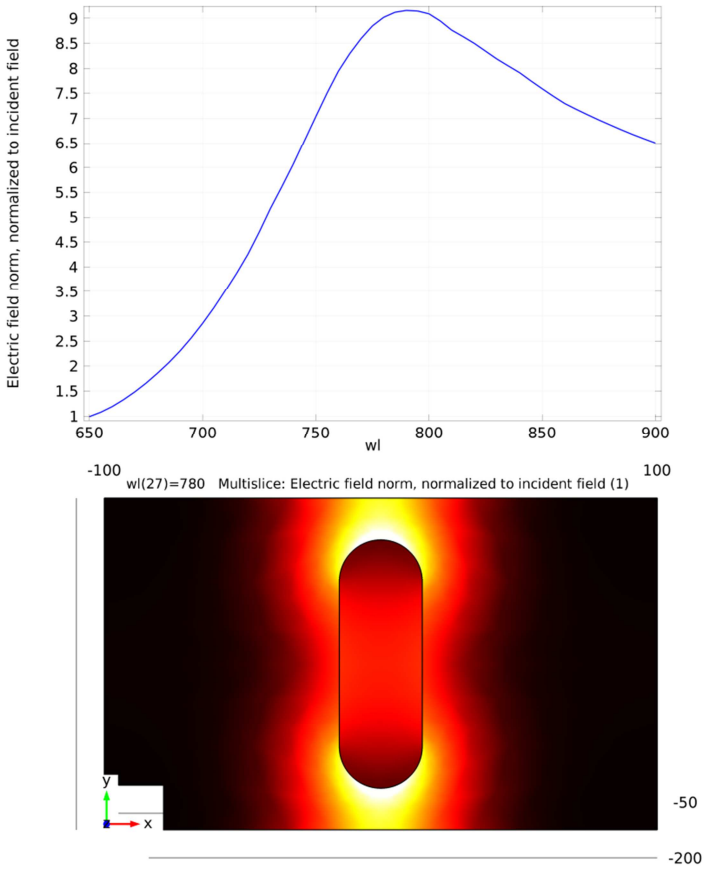

Figure 3.7 Spectral dependence of electric field norm in the middle of the gap, for an array of Au nanorods with l=95 nm and w=t=30 nm, separated by a gap of 30 nm. Inset: plot of the electric field norm in a unit cell for the optimized geometry (slice at half thickness).

At this point, the design of the structures was completed and we started performing fabrication. However, as will be shown in the next section, we encountered some problems during fabrication, due to the high roughness of the ITO layer. We therefore decided to use ITO-coated glass slides with a thinner ITO layer (nominal thickness: 15-30 nm). The simulations were repeated with the new configuration. The optimal and final values found in this case are summarized in Table 3.1. Figure 3.8 shows the spectral dependence of the electric field norm in the middle of the gap and with the full solution in a unit cell of the array for the optimized geometry. A peak is clearly visible for λ=780 nm.

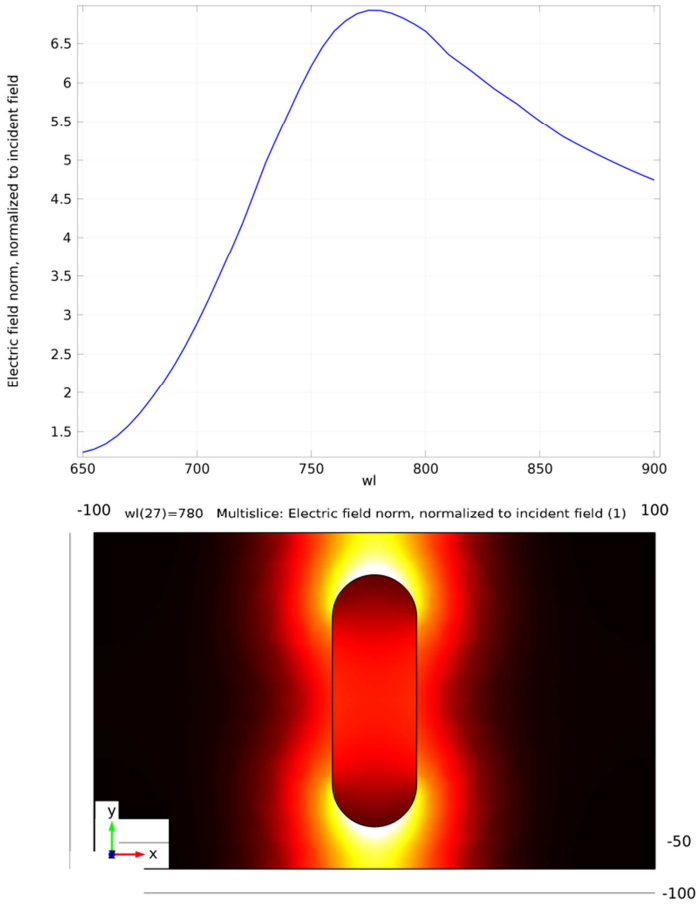

Figure 3.8 Spectral dependence of electric field norm in the middle of the gap, for an array of Au nanorods with l=90 nm and w=t=30 nm, separated by a gap of 30 nm and sitting on a 20 nm- thick ITO layer. Inset: plot of the electric field norm in a unit cell for the optimized geometry (slice at half thickness).

NR length	NR width	NR thickness	Gap y	Period x
90 nm	30 nm	30 nm	30 nm	200 nm

Table 3.1 Final optimized nanorod array parameters, with an ITO thickness of 20 nm.

Figure 3.9 compares the calculated electric field norm for two perpendicular directions of polarization, namely along the major axis ((a), used in the simulations reported above) and along the short axis (b). The figure includes two unit cells of the array along y for a better visualization of the hot-spot and was calculated at resonance. It is clear that, when we switch polarization from “parallel” to “perpendicular” with respect to the nanorods major axis, the device is switched on and off.

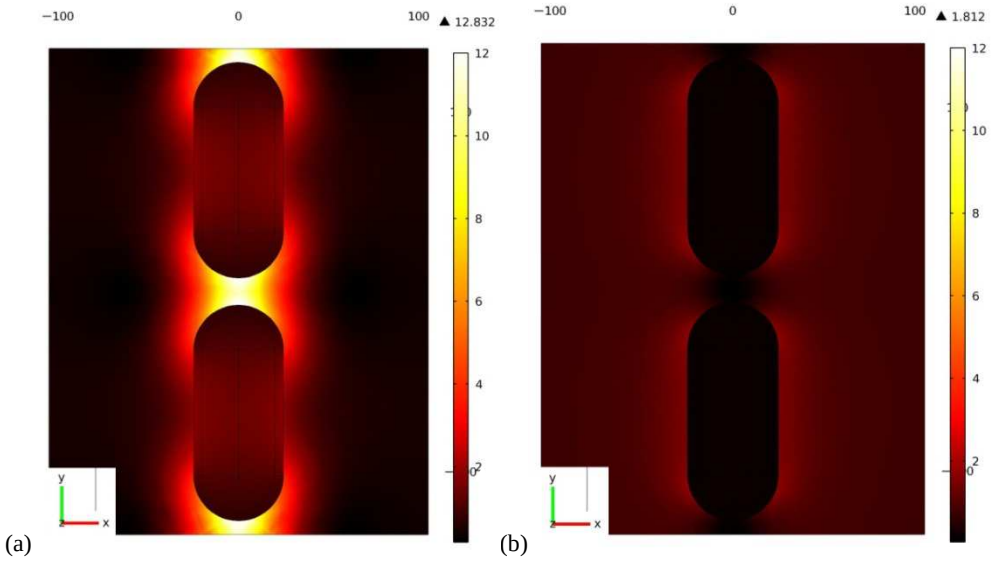

Figure 3.9 Plot of the electric field norm around the nanorods with (a) parallel and (b) perpendicular polarization.

We now want to quantify the expected SERS enhancement factor of our device. As can be seen from the optimization, the expected electric field enhancement factor is 6.9 at pump wavelength, while at the Stokes wavelength of 845 nm (corresponding to the Raman shift 992 nm^{-1}, breathing of the benzenic ring) it reduces to 5.5. We calculated the enhancement factor as $|E_{pump}|^2 \, |E_{Stokes}|^2$, obtaining $1.44 \cdot 10^3$.

3.4 Fabrication

The structures were fabricated by EBL, followed by electrolytic growth of gold. A sketch of the fabrication process is reported in Figure 3.10.

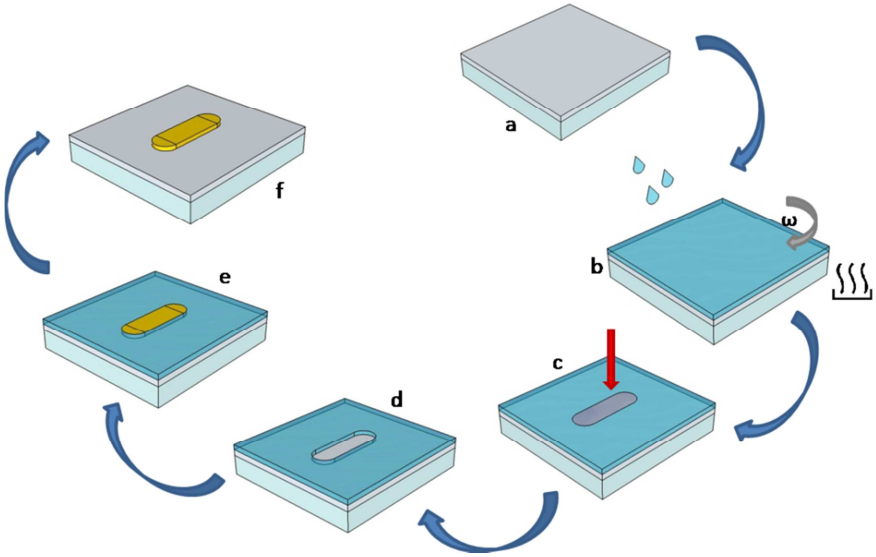

Figure 3.10 Sketch of the fabrication process. (a) The substrate is an ITO-coated glass slide. (b) The sample was spin-coated with PMMA (positive tone resist) and soft-baked at 180° for 10 minutes on a hot plate to obtain a final thickness of 90 nm. (c) The sample was exposed by high-resolution electron-beam lithography and (c) developed in DI H_2O:IPA 3:7 for 20s. (e) 30 nm of gold were deposited by electrolytic growth and finally (d) the resist was stripped by dipping the sample in hot acetone (52° C) for 3 minutes and rinsing in cold acetone and IPA.

EBL was performed in high resolution (HR) mode (100 keV, beam current 100 pA). This technique offers a high degree of control of the particle shape, its orientation and the pattern arrangement. In fact, the performance of our machine in HR mode achieves a minimum line width below 10 nm. Moreover, the structures can be easily placed into a regular array, so that the uniformity of the sample is guaranteed and the distance between the nanorods can be easily and precisely controlled.

The initial substrate, as mentioned above, was a glass slide coated with an ITO layer having a nominal thickness of 100 nm. First of all, PMMA (AR-P 671.02, nominal thickness 90 nm at 4000 rpm) resist was spun onto the substrate for 60 s and soft-baked at 180° for 10 minutes, to obtain a final resist thickness of 90 nm. Then, the sample was exposed in HR-EBL.

In order to obtain uniform and well-defined chips, a naïve EBL exposure is often not enough. As discussed in detail in Appendix 1, Proximity Effect Correction (PEC) is extremely important; it refers to the dose correction that must be applied to different regions on the same sample, in order to compensate for the different amount of backscattered energy which hits the sample in a geometry-dependent way. In the case of nanorods, it is important to correct for wrong dose assignments not only overall the chip (in order to maintain the desired array structures also at the chip sides and corners) but also around the nanorod ends, which are at the same time tiny and very close to one another. To this end, short-range PEC was performed together with long-range PEC. The correct base dose (BD), α, η and β parameters were

identified by exposing nanorods chips with different PEC parameters around the standard ones foreseen for the materials we were using. In the end we obtained BD=1860 $\mu C/cm^2$, β=40 nm, η=0,4 and α=10 nm. We therefore exposed the corrected pattern with these parameters.

After the EBL exposure, the samples were developed in a mixture of DI H_2O and IPA 3:7 for 20 s and rinsed in DI water. Then, Au was grown on the lithographed substrates by electrolytic growth in a bath with an acidic solution, controlled in voltage. The growth rate was calculated to be 2.2 nm/s. The resist was then stripped and the obtained samples were finally imaged by SEM, as shown in Figure 3.11.

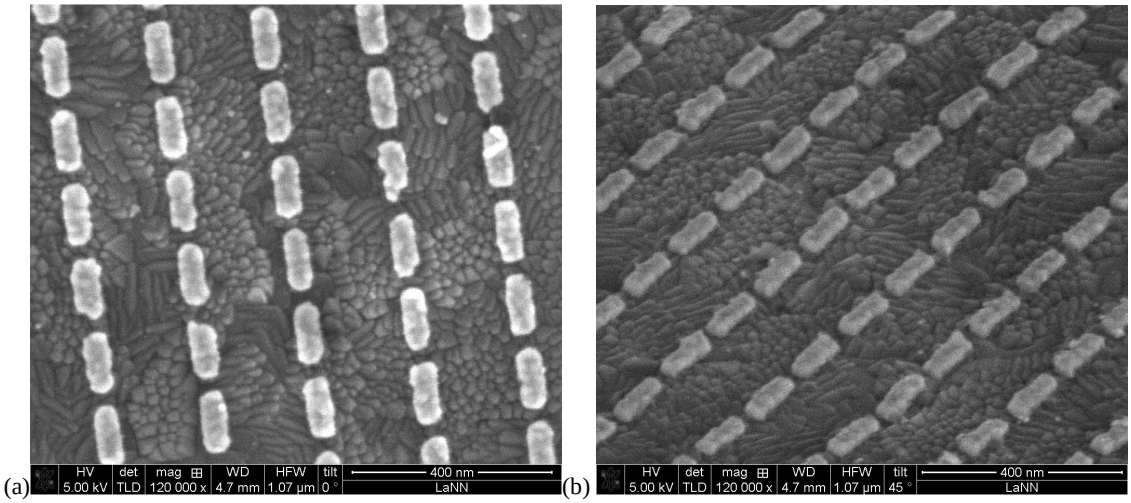

Figure 3.11 (a) SEM micrograph of the first fabricated nanorods. (b) Tilted picture. As can be seen, the roughness of the substrate strongly affects the growth of the nanorods, which follows the morphology of the ITO crystals.

As can be seen from the pictures, the result was not good. The shape of the structures is quite irregular; in particular, they seem to follow the morphology of the underlying ITO crystals, which are quite big compared to our structures. This effect did not significantly influence the growth of bigger structures such as the plasmonic gratings described in Chapter 2, but strongly affect the geometry of our tiny nanorods.

Before considering changing the substrate, we tried modifying the post-lithographic process, using Au evaporation instead of electrolytic growth. However, the lift-off step did not work properly, since the gap was very narrow; moreover, the shape of the rods was not improved (Figure 3.12).

(a) 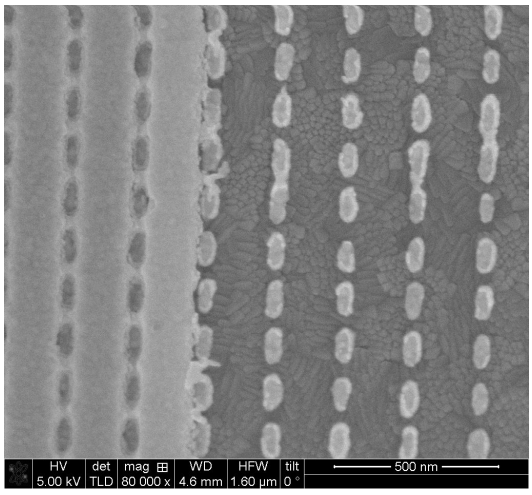

(b) 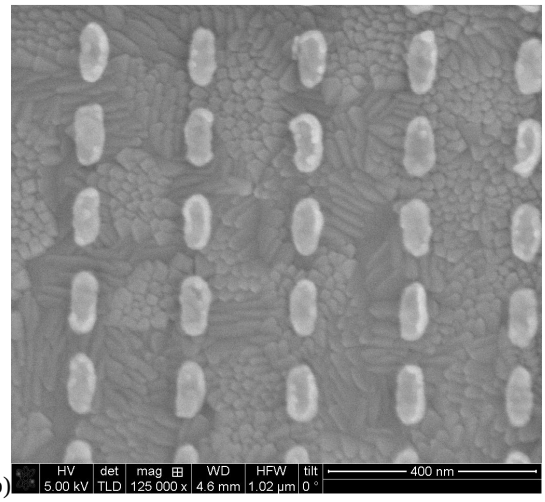

Figure 3.12 (a) Problems with the lift-off process. (b) SEM picture of the nanorods fabricated by EBL, followed by Au evaporation and lift-off. It seems that changing the metal deposition strategy does not improve the shape of the structure, which is mainly determined by the morphology of the substrate.

It therefore seemed that the metal deposition strategy was not the problem. The shape of the nanostructures was mainly determined by the morphology of the substrate, and this problem could be overcome neither by changing the post-processing strategy nor by improving the lithography or PEC. We therefore decided to use a smoother substrate. We bought ITO-coated glass slides with a thinner ITO layer from Sigma-Aldrich; the nominal thickness was ≈20 nm. With these new substrates, we were able to obtain very good structures, as shown in Figure 3.13.

(a). 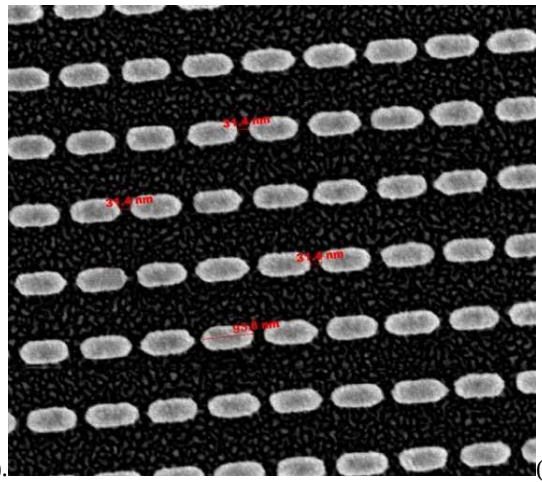
(b) 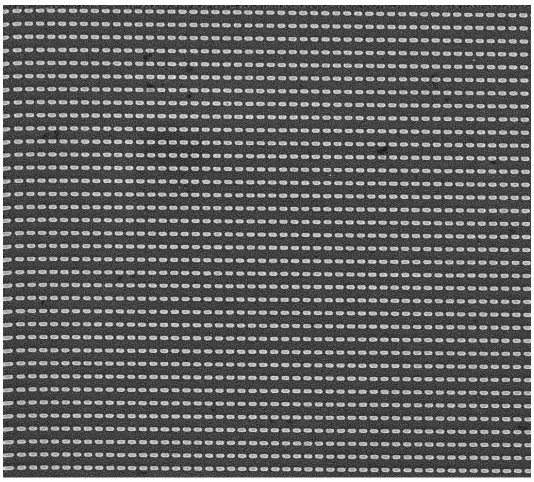

Figure 3.13 SEM pictures of a fabricated nanorod arrays. (a) Coupled nanorods corresponding to the simulated structures. (b) Large image showing the uniformity of the fabricated chip.

3.5 SERS experiments

We then used our structures for SERS analysis. The nanostructures were functionalized with benzenethiol, which was chosen since its refractive index is well-known and because of the high cross sections of its Raman bands. The functionalization was performed by dipping the substrate in liquid benzenethiol (10mM) overnight. The SERS measurements were performed with a micro-Raman instrument equipped with a 50x microscope objective. The microscope allows focusing of the incident beam into a spot of 2 μm. The light, collected in backscattering by the same objective, is filtered through a notch filter that cuts almost all elastically scattered light, transmitting the Raman emission of the sample.

In Figure 3.14 we report a typical SERS spectrum measured on a nanorods chip. The black curve refers to parallel polarization while the red one refers to perpendicular polarization. As expected, the signal is highly suppressed for perpendicular with respect to parallel polarization, suggesting that the enhancement is actually due to the LSPR resonance rather than to any isotropic effects (i.e. surface roughness).

The experimental SERS substrate enhancement factor (SSEF) can be evaluated by using

$$EF = \frac{I^{SERS,BT}}{I^{RS,BT}} \frac{C_V^{BT} H_{eff}}{C_S^{BT}} \frac{1}{A} \tag{3.1}$$

where I is the Raman signal intensity of the molecule monolayer absorbed on the metal surface (SERS) and the liquid used as reference (RS), CV and CS are the volumetric and packing density of the reference liquid and the BT adsorbed, H_{eff} is the collection efficiency of the experimental set-up and A is the ratio between the patterned area and a flat one.

The experimental enhancement factor, calculated using the 992 cm^{-1} Stokes band of benzenethiol, was $(1.4\pm0.8)\cdot10^3$, in good agreement with predictions.

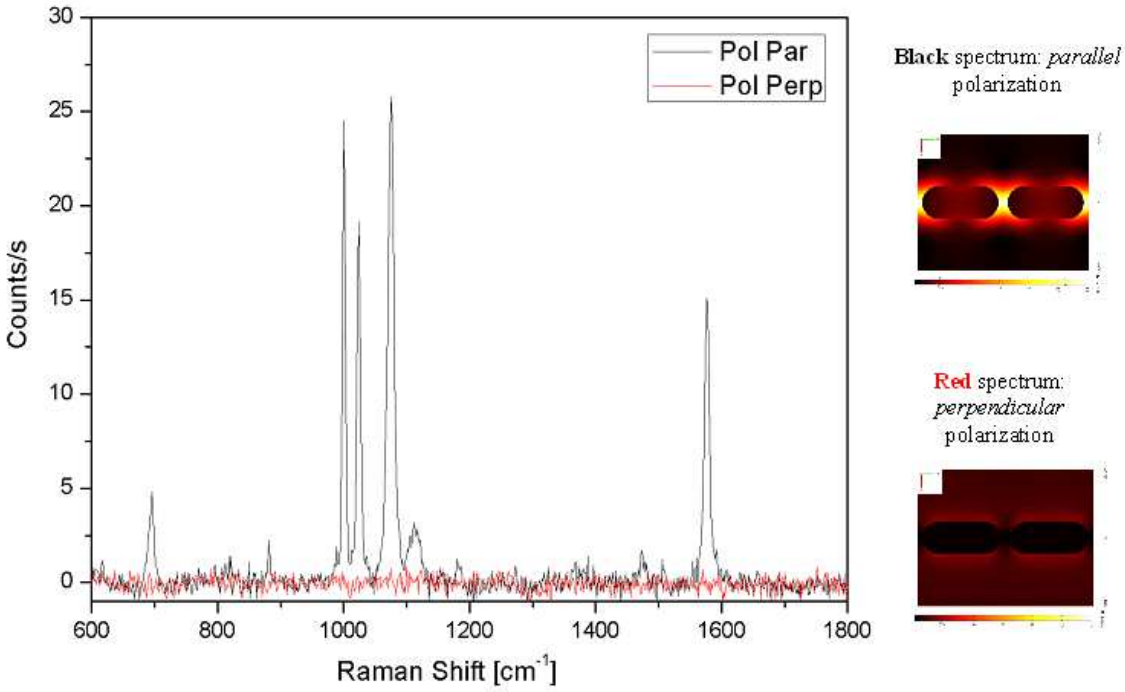

Figure 3.14 Measured SERS spectrum on a nanorod array chip. The red spectrum (perpendicular polarization, no enhancement) is clearly suppressed with respect to the black one (parallel polarization). Insets: plot of the electric field norm.

3.6 Application to SECARS

We have recently started a collaboration with Politecnico di Milano for the application of the nanorod structures to SECARS. CARS is a resonant process induced in its simplest form by a pair of narrowband picosecond pulses with frequencies ω_{pump} and ω_{Stokes} - the so called pump and Stokes frequencies – the difference of which matches a Raman active molecular vibration Ω. When resonant excitation occurs, a third photon at ω_{pump}, also provided by the pump beam, interacts with the excited vibration level to coherently emit a photon at the anti-Stokes frequency $\omega_{anti\text{-}Stokes}$, thus providing a chemically specific signature of the probed molecule. In CARS, a strong issue is represented by the dependence of the signal on the square of the number of oscillators in the focal volume. Whenever such number is low, due to a strongly diluted sample or to a low density of chemical bonds, CARS fails to exhibit the required sensitivity for many applications. That is why a strong interest has arisen around the possibility of exploiting Surface Enhancement (SE) techniques similar to the ones used for SERS, in order to boost the CARS signal (SE-CARS).

Due to these characteristics of SECARS, it would be extremely interesting if we could produce multiple-resonance structures, able to enhance the signal at both the excitation

wavelengths and possibly at all the three wavelengths. In some very recent experiments in literature [99], the Enhancement Factor for SECARS has been reported to be proportional to be $G_{SECARS} = g_{pump}^4 g_{Stokes}^2 g_{anti-Stokes}^2$, where $g = E/E_0$ is the enhancement in local optical field at each frequency, thus providing an advantage over SERS ($G_{SERS} = g_{pump}^2 g_{Stokes}^2$) given by $\frac{G_{SECARS}}{G_{SERS}} = g_{pump}^2 g_{anti-Stokes}^2$. In our case, the wavelengths of interest were 780 nm (pump), 895 nm (Stokes) and 690 nm (anti-Stokes).

As a zero-step, we wanted to investigate the behavior of the SE-CARS enhancement factor when only one of the three wavelengths is enhanced at a time. Therefore, the structure could simply be an array of nanorods, like the ones we have already studied for SERS and described above. Of course, we have to fabricate three separate arrays, each one optimized for one of the three wavelengths involved. To this end, we repeated the optimization described above for Stokes and anti-Stokes wavelengths. Moreover, in this case, an additional fabrication issue had to be taken into account. In fact, with the new (cyanide free) electrolytic solution in use in our lab, the thin ITO layer turned out to be not enough conductive, resulting in a non-uniform growth. The use of a cyanide-free solution was imposed by safety issues. In order to improve the conductivity of the substrate, we decided to sputter a nanometric (2-3 nm thick) layer of Au on the ITO surface before spinning the resist. This must of course be taken into account in the simulations; thus, we also had to repeat the optimization for 780 nm. We kept the width and thickness fixed for all three wavelengths, in order to have nanorod length as the only parameters changing in the three chips. The optimized parameters are reported in Table 3.2; Figure 3.15 (a) shows the spectral dependence of the resonances.

Wavelength	**Length**	**Width**	**Thickness**	**Gap y**	**Gap x**
690 nm	105 nm	35 nm	55 nm	30 nm	160 nm
780 nm	150 nm				
895 nm	220 nm				

Table 3.2 Final optimized nanorod array parameters, with an ITO thickness of 20 nm.

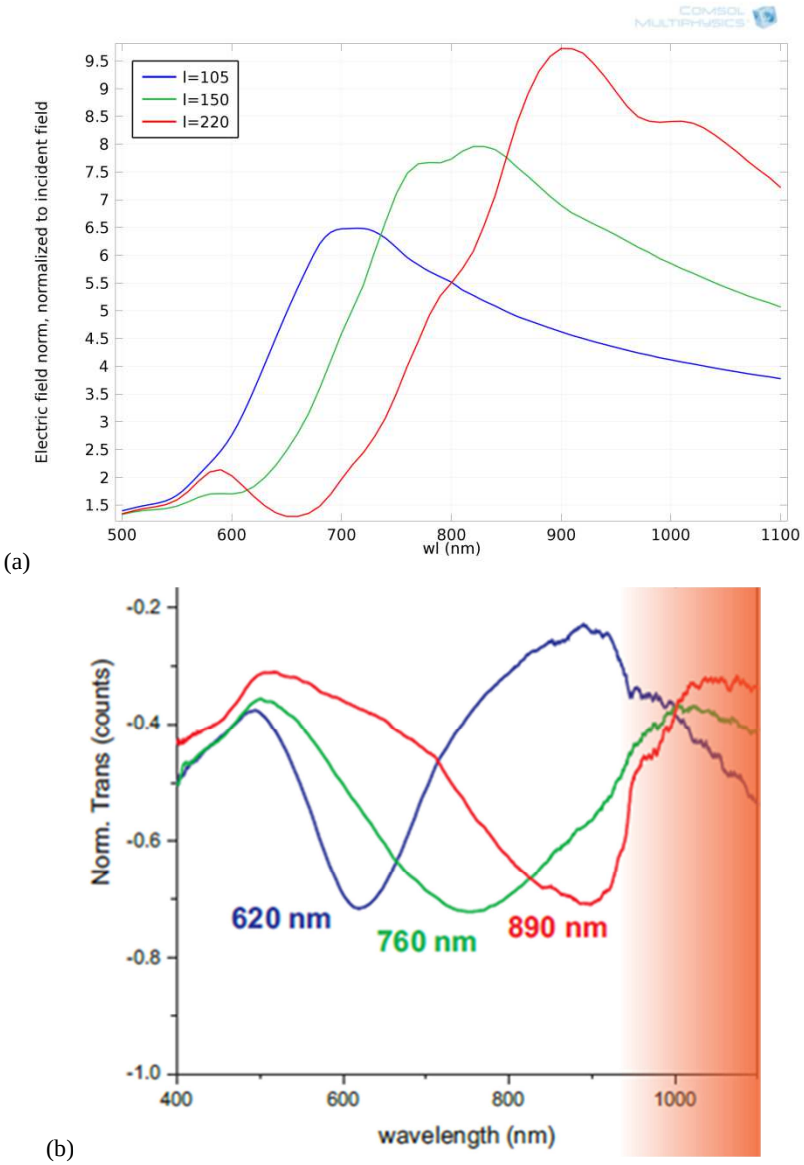

Figure 3.15 (a) Spectral dependence of the resonance, calculated for the three wavelengths involved: 690 nm (Anti-Stokes, blue curve), pump (780 nm, green curve), Stokes (895 nm, red curve). The spectra were calculated for optimized geometry. (b) First extinction measurements performed on nanorods arrays on a glass/ITO/Au(sputtered) substrate. The resonances are broad and slightly blue-shifted. This effect is probably due to the sputtered Au layer.

The resonances are broad, but anyhow they meet the spectral requirements of the SECARS experiment. We then fabricated the nanorod arrays using the same fabrication process described above. The presence of the sputtered Au layer increased the roughness a little bit, but in a way that did not affect the metal deposition. SEM pictures of the fabricated structures are shown in Figure 3.16 for the three wavelengths, together with the calculated electric field norm in a unit cell of each array.

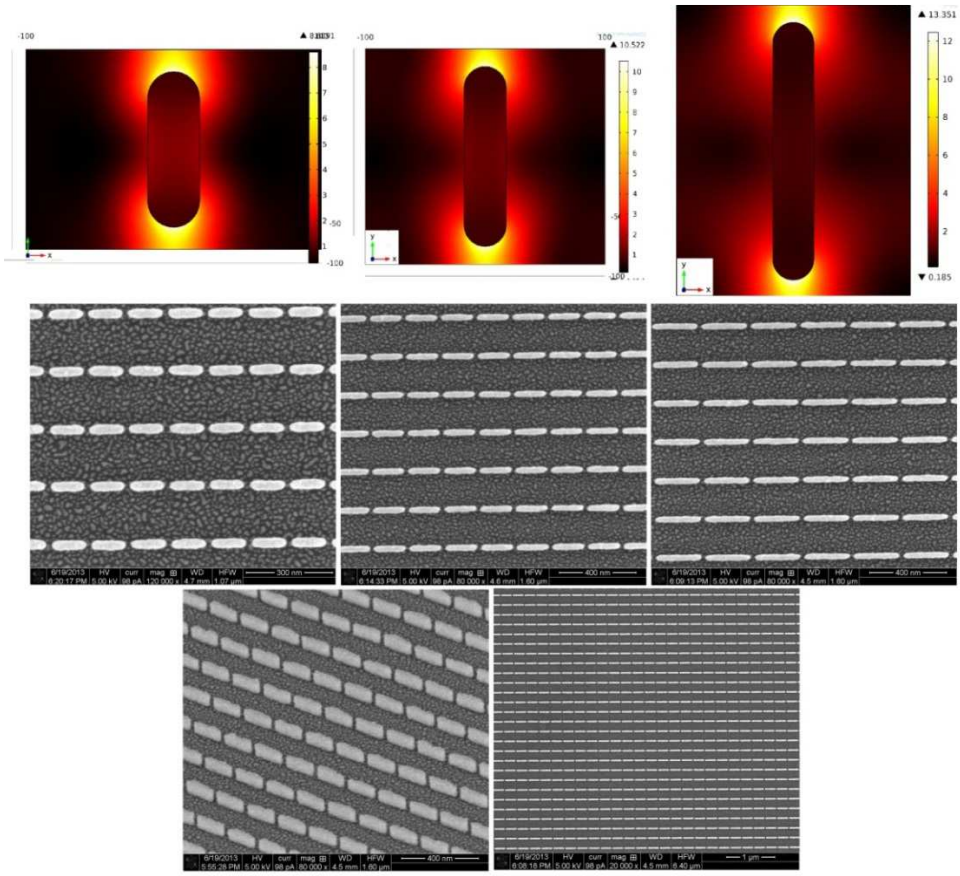

Figure 3.16 SEM pictures of the fabricated nanorod arrays for SE-CARS. First line: plot of the electric field norm, normalized to the incident field, for the optimized geometry. Left to right: optimization for 690 nm, 780 nm and 895 nm, respectively. Second line: corresponding fabricated arrays. Third line: tilted SEM picture and large-field picture highlighting the uniformity of the samples.

The substrates were characterized at Politecnico and the results are shown in Figure 3.15 (b). For optimized structures, the resonances meet the design wavelength, but, as expected, they are quite broad. Moreover, we found that the thickness of the sputtered Au layer strongly affected the resonance: for instance, passing from 3 nm to 10 nm, the resonance is blue-shifted of 100 nm, as shown in Figure 3.17 (a). This effect could explain some results obtained by PoliMi, where some nanorod chips exhibited strongly blue-shifted resonances, reported in Figure 3.17 (b). Since sputtering does not allow such a precise control of the thickness of the Au layer, we decided to remove it and use another electrolytic solution, available in our partner laboratory at IOM/TASC, in Trieste. This solution is not cyanide free but it enables electrolytic growth on the ITO layer without the need of any additional conductive layers.

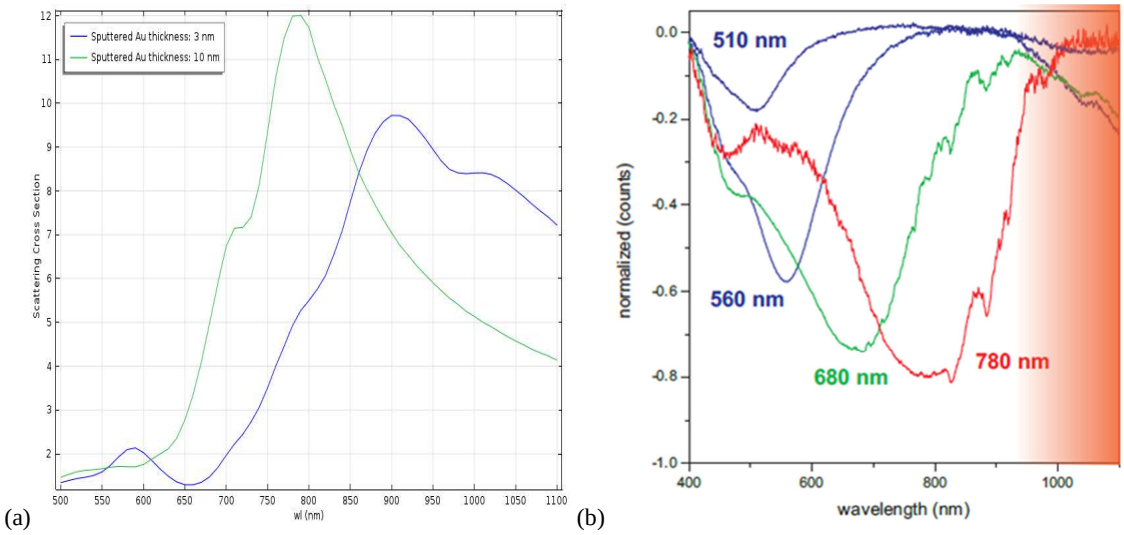

Figure 3.17 Effect of varying the thickness of the sputtered gold layer deposited onto the substrate to enhance the conductivity of ITO. (a) Passing from 3 nm (blue curve) to 10 nm (green curve) of gold, a shift of more than 100 nm is observed. (b) In one of the samples measured at PoliMi, the resonances looked blue-shifted by around 100 nm. An imprecise control of the Au layer thickness may be the cause, since the control on this parameter is not accurate enough (and for sure less accurate than the other parameters, which are defined by lithography), provided that, as shown in (a), the slightest shift on this parameter can dramatically change the response of the device.

Moreover, we decided to study the effect of placing the particles in array, in order to clearly distinguish the features of the response of single (or coupled) particle from collective effects. To this end, we considered three different configurations: isolated single nanorods, isolated nanorod dimers, nanorods array. The simulations show that, in the three configurations, the resonance occurs for similar (even if not equal) values of the geometry; nevertheless, it would be interesting to investigate the response of the system experimentally. All the structures – three wavelengths for three configurations - were therefore optimized in the new conditions after having measured the optical constants of the new electrolytically grown gold; the results are summarized in Table 3.3 and the scattering cross section of the optimized single structures is reported in Figure 3.18 as a function of the wavelength. The fabrication is being optimized in these weeks.

	λ=690 nm	**λ=780 nm**	**λ=895 nm**	**Other parameters**
Isolated particle	80 nm	110 nm	150 nm	t=w= 30 nm for all g_y=30 nm where present Period along x: 300 nm
Dimer	75 nm	105 nm	140 nm	
Array	70 nm	100 nm	140 nm	

Table 3.3 Optimization of the new nanostructures for SECARS.

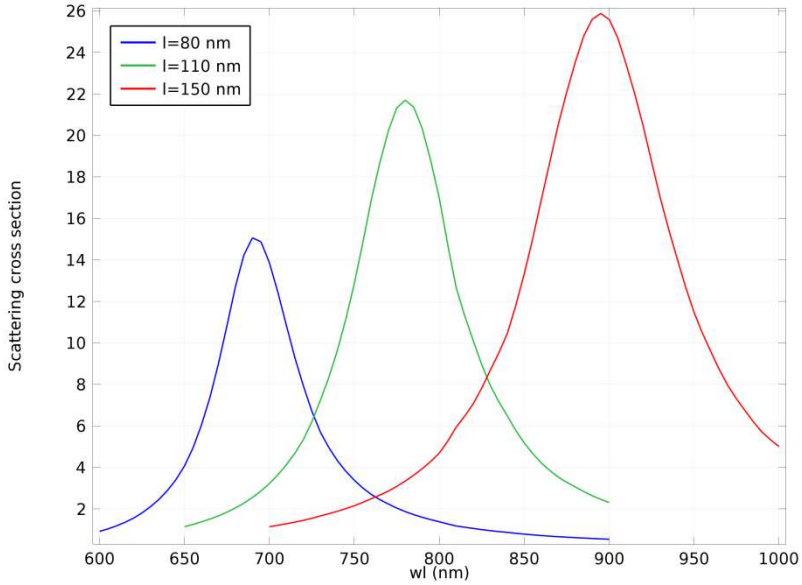

Figure 3.18 Scattering cross section of the optimized single structures according to Table 3.3, as a function of the wavelength. The spectra for dimers and arrays are similar.

In the meantime, SECARS measurements will be done on the old samples; in fact, the observed broad resonance could be useful to enhance more than one wavelength at the same time, as actually required for the optimal SECARS measurements, and it would be useful to compare these results with the one obtained in separately resonant substrates.

Parallel to this optimization, we are studying structures providing multiple resonances; this would actually be the optimal configuration, with sharp-and well defined resonances at exactly the wavelengths of interest. In particular, we were inspired by the Y-shaped structure reported in [101]. We modified this structure by setting a different length for each of the "short" arms of the Y, expecting two resonances to occur, at two separate wavelengths, for the two arms. Moreover, we wanted to obtain the multiple resonance *at the same place* on the structure. To this end, we further modified the structure by adding a small gap (15 nm) in the long arm of the Y; a sketch of the structure is shown in the inset in Figure 3.19.

We expect that, for conveniently small gaps, this region will be excited at both the resonant wavelengths. Figure 3.19 shows the results of an optimization performed by FDTD simulations on such a structure; in this case, the structure is optimized for being resonant at the Stokes and anti-Stokes wavelengths, but it can be tune to obtain any combination of the three wavelengths of interest. The transmittance as a function of the wavelength is shown, together with the full solution (shown is the electric field norm) on a slice at half thickness. For both wavelengths, the electric field is enhanced within the gap.

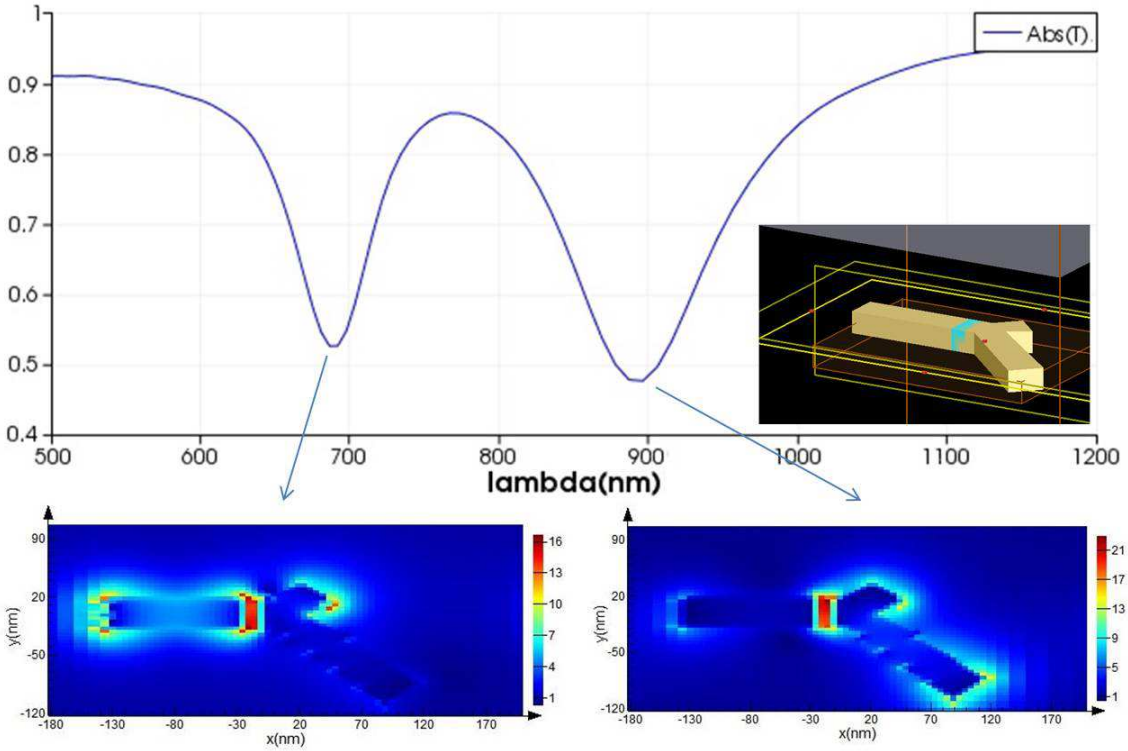

Figure 3.19 FDTD model solution of a Y structure supporting two resonances at separate wavelengths. The big plot shows the transmittance as a function of the wavelength, showing two dips at 690 nm (anti-Stokes) and 895 nm (Stokes). The insets show the electric field norm on the structure (slice at half thickness) at the two resonant wavelengths. For both resonances, the electric field is enhanced within the gap. The structure can be tuned in order to obtain any combination of the three wavelength of interest.

The fabrication of this structure will be performed as soon as the characterization of the first proposed substrates (nanorods) has been completed.

3.7 Conclusions

We designed and fabricated coupled gold nanorods, arranged in a periodic array, and we used these chips for SERS applications. We extensively studied all the parameters affecting the resonance. This allowed us to identify the parameters which should be tuned to obtain an optimized SERS substrates and gave us a strong reference framework for the design of the nanorods.

We simulated the structures numerically using the Finite Element Method. Initially, we were looking for a resonance at the visible and common wavelength of 633 nm, but soon we realized that a “proper” gold nanorod structure could not support this resonance. Instead, we found a resonance either for Ag particles at the same wavelength, or for Au particles, but using a higher

wavelength. We chose the NIR 780 nm wavelength since it is also widely used in labs and it allowed us to work with Au nanoparticles, which do not undergo oxidation. We then fabricated the structures by EBL and electrolytic growth, thus achieving a good and reproducible control on particle geometry and arrangement. We also described a SERS experiment which provided an experimental enhancement factor in good agreement with the calculated one.

We also described the recent collaboration started with Politecnico di Milano. The project aims to exploiting these structures for SECARS. About this, preliminary results were shown and discussed. It is worth mentioning that the work described in this Chapter and the deep understanding it gave us about LSPR-supporting nanostructures will pave the way to the design and fabrication of smarter structures (e.g. supporting multiple resonances) which are being optimized and shall be used in the framework of this SECARS project.

Chapter 4

Squeezing light on a ridge: plasmonic adiabatic nanofocusing by means of metal wedges

4.1 Introduction

In Chapter 1 and Chapter 3 we have seen how nanostructures supporting a Local Surface Plasmon Resonance can find important applications in all the fields where nano-scale resolution is essential. As a matter of fact, the investigation of such strongly localized plasmons has attracted a large interest in recent years, due to the possibility of confining light beyond the diffraction limit [73].

In the localized plasmon-supporting structures we have described so far, a plasmon is directly excited by impinging light and has an inherently localized nature, due to the confined geometry considered. Now, a central problem of the nano-optics is: "Is it possible to *deliver* and *concentrate* the optical radiation energy on the nanoscale?" This problem introduced the concept of *nanofocusing*, with which we are dealing in this Chapter.

The word "focusing" probably reminds us the concept of a lens. In particular, we know that a spherical lens focuses electromagnetic energy into a small region. However, for a spherical lens, the dimensions of this region cannot be smaller than those allowed by the diffraction limit (half the wavelength of the incoming radiation). For a plasmonic nanofocusing system, instead, this is possible; in the case of a metallic nano-tip for instance, the region of localization has the dimensions of the tip curvature radius, that can be as small as few nanometers, i.e. two orders of magnitude lower.

A major issue when dealing with electromagnetic energy transfer in materials are losses. In many cases, only a minor part of the excitation energy is actually transferred to the nanoscale. A way to overcome this problem was proposed by Stockman [1]. In that work, he theoretically demonstrated that axially symmetric SPPs propagating toward a tip of a tapered metallic nanowire, acting as a surface plasmon waveguide, are slowed down and asymptotically stop near the tip, i.e. their phase and group velocities tend to zero. This phenomenon, referred to as

adiabatic nanofocusing, causes accumulation of energy and giant local fields at the tip, leading to huge EM field enhancements; the term “adiabatic” refers to the absence of power losses involved in the phenomenon other than metal dissipation [1, 102]. The fact that the tip is a plasmonic waveguide rather than the conventional tapered optical fiber supporting guided photonic modes is crucial. In the latter case, in fact, there would be a cut off at some waveguide radius, beyond which the propagation is not possible [1, 103], because of back-reflections. This problem is well-known, regarding, for instance, the efficiency of SNOM probes [30, 104]. With the proposed plasmonic waveguide instead, the local EM field is oscillating in space with progressively decreasing wavelength and increasing amplitude, and the highest enhancement is limited only by the tip size.

In this Chapter, we present a work in which we designed, fabricated and characterized propose an alternative structure providing adiabatic nanofocusing. In particular, we obtained plasmonic field localization at the ridge of a metal-coated dielectric wedge. The proposed layout is significantly simpler than axially symmetric configurations proposed in literature. These structures theoretically provide higher field enhancements, but their performance crucially depends on the curvature radius at the tip [102, 105], which is very difficult to control in fabrication.

Gramotnev and Vernon [106] discussed nanofocusing of SPPs along the sides of a sharp metallic wedge, describing it as a metal film with varying thickness. In these structures, the two SPPs travelling along the sides actually couple near the tip, where they form a film plasmon. However, only plasmons with an anti-symmetric distribution of the magnetic field across the wedge will experience nanofocusing. Proper excitation of the wedge mode is therefore a major problem we must take into account. Fabrication issues, such as metal surface quality and tip sharpness, are at least equally important. In fact, as previously reported [107], Surface Plasmons are very sensitive to surface inhomogeneities, which may cause enhanced metal losses, scattering, and limited propagation.

With our compact design, both efficient coupling of light to SPPs and the correct in-phase matching of SPPs are achieved. This is obtained by combining metal-coated transparent wedges with a dielectric step-like phase shifter. The role of the phase shifter is to produce a π-phase shift between SPPs on the two sides of the wedge, thus allowing the correct interference conditions at the tip. Full field Finite Elements simulations allowed to verify the design and to optimize the materials and the geometrical parameters. In order to achieve large field enhancements [102, 105], then, we chose a fabrication process ensuring very sharp features, in particular very low tips radii, and low surface roughness. We were inspired by the strategy proposed by Napgal et al. [107] and Boltasseva et al. [108], which leads to very smooth surfaces

and sharp edges, and we developed a fabrication process which basically consists in a template stripping based on replica in a transparent polymer. Characterization was carried out by means of Scanning Near-field Optical Microscopy (SNOM) and Raman spectroscopy measurements.

The enhancement obtained with our structure, although not comparable to that obtained with 3D focusing structures, demonstrates that the proposed scheme for coupling and phase matching can be effectively exploited for nanofocusing purposes.

4.2 Parameters affecting nanofocusing

Nanofocusing in tapered plasmonic waveguides has been extensively investigated by Gramotnev et al. [106] and Stockman [1, 109] in the *adiabatic* hypothesis. For this hypothesis to be matched, there must be a parameter (or a parameter set) slowly ("adiabatically") varying along the waveguide, in such a way that the phase velocity of these SPPs tends to zero in the vicinity of some point at a finite distance. This condition can be described in terms of the *adiabatic parameter*, expressed by

$$\delta = \left| \frac{dk_{SPP_x}^{-1}\left[p(x) \right]}{dx} \right| \prec 1 \tag{4.1}$$

where x is the propagation direction of SPPs, $p(x)$ is the parameter set varying along the waveguide and k_{SPPx} is the projection of the real part of the SPP propagation constant along the propagation direction. In metal wedges and tips, $p(x)$ is the cross sectional size (wedge thickness or tip conical tip radius). For adiabatic nanofocusing to take place, it is also required that the excited SPP mode exists without a cut-off in the entire range of the parameters. If these conditions are satisfied, the effect can be simply described in terms of the SPP modes of the straight structure; the adiabatic theorem predicts that the wave will propagate without back-reflections and scattering into three dimensions to the stopping point, where it is converted into a quasi-electrostatic Surface Plasmon.

As can be shown [109], an important consequence of this hypothesis is that it sets an upper limit to the aperture angle θ. On the other hand, arguments of general validity can be applied which lead to a general scaling law of the SPP field amplitude as a function of the distance from the tip. This hypothesis is reasonable whenever the SPP wavelength is much shorter than the vacuum wavelength. In these conditions it was demonstrated [109] that a constraint to the minimal aperture angle, θ, exists and is given by:

$$\theta > \theta_{\min} = \arctan\left(2\frac{\operatorname{Im} k_a}{1+d}\right) \tag{4.2}$$

where d is the waveguide dimensionality and k_a is a complex quantity. The physical meaning of this limit is that SPPs should be focused sufficiently fast to allow the nanofocusing field enhancement to exceed the SPPs losses in metal. Therefore, from these arguments is seems that, for a tapered waveguide, the range of angles for which adiabatic nanofocusing is possible is strictly limited. Actually, numerical simulations [110] revealed that these conditions are too restrictive, and the adiabatic theory also works for relatively large angles. Moreover [111], an increased taper angle often means a wider power collection to SPP modes and a therefore a more efficient power delivery to the tip. As a matter of fact, numerical studies demonstrated that in case of tapered rods, the taper angles maximizing the field enhancement lie in the range 30-40° [110].

Another parameter to be taken into account is curvature radius. In particular, it is interesting to note that, for reasonable experimentally achievable curvature radii (≥5nm), the field enhancement depends by a much lower extent upon aperture angles; above this limit, the curvature radius still actually turns out to be the most relevant parameter that determines the nanofocusing performances.

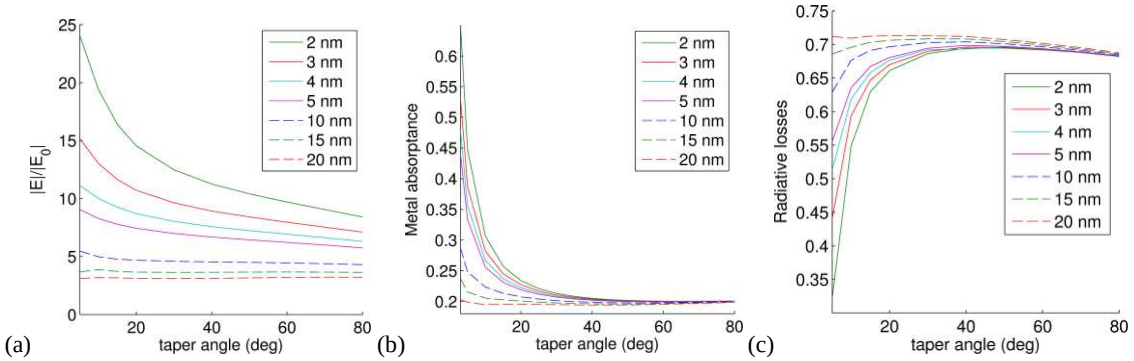

Figure 4.1 FEM-calculated field enhancement at the tip (a), metal absorptance (b) and radiative losses (c) as a function of taper angle, for different curvatures radii at the tip. The metal considered is silver [33], the SPP wave has frequency $\omega = 2.97 \cdot 10^{15}$ Hz (vacuum wavelength 633 nm).

These considerations led us to consider the wedge nanostructures presented in the following. In fact, despite the high aperture angle, the proposed structure can be fabricated with extremely low curvature radii, thus allowing to reach valuable nanofocusing effects.

4.3 Proposed device layout and simulations

Different experimental setups can be designed in order to verify the nanofocusing properties of wedges [112, 113, 114]. Our setup resembles the well-known Kretschman-Raether [3, 115] SPPs generation scheme. We consider first the layout sketched in Figure 4.2, i.e. a transparent dielectric wedge coated with a thin metal film. Air is supposed to be present in the other half-space. TM polarized light with proper frequency impinges normally onto the basis of the wedge from the transparent dielectric side. Thin-film SPPs can thus be excited at the metal-air interface.

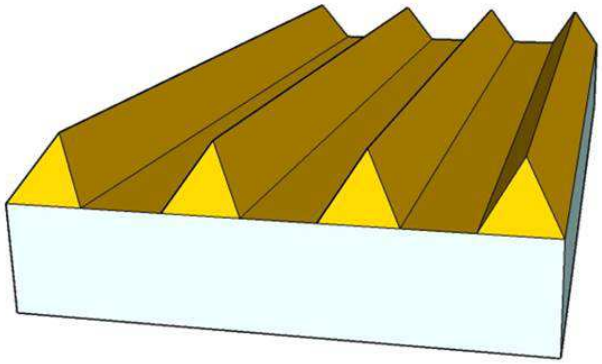

Figure 4.2 Sketch of the wedge structure.

In order to verify the plasmonic effects outlined above and to properly design the structure so as to maximize the field enhancement at the ridge, we simulated the full electromagnetic fields by means of the Finite Elements Method. The FEM model layout is reported in Figure 4.3 (a)). Since the structure is inherently invariant along the out-of-plane dimension, 2D simulations were performed. A port excitation is set at the upper boundary, providing a unit power of incident light. Perfectly Matched Layers are placed all around the model in order to properly absorb light scattered from the structure. Model discretization is performed by means of the COMSOL automatic meshing tool. In particular, different mesh sizes were used in different parts of the model in order to maximize resolution in the regions of steepest variations of the fields, keeping at the same time reasonable the computational costs.

Figure 4.4 (a) shows the results of the simulations. Let us look at the y component of the electric field plotted in the inset. The two contributions on each side of the wedge are π-out-of-phase and SPPs are thus expected to undergo disruptive interference when they reach the tip, resulting in a plane wave propagating away from the structure into air

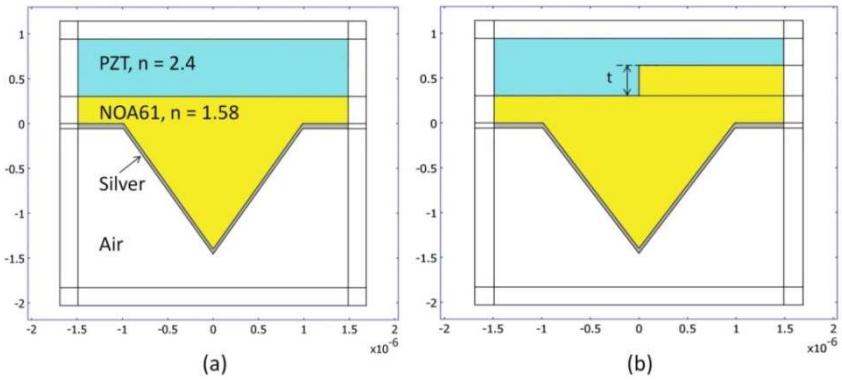

Figure 4.3 FEM models layouts of the simulated metal coated dielectric nanowedge structures. Configuration without (a) and with (b) phase shifter. TM polarized plane waves impinges normally onto the structures from the top wedge aperture is 70.4° as reported in the text.

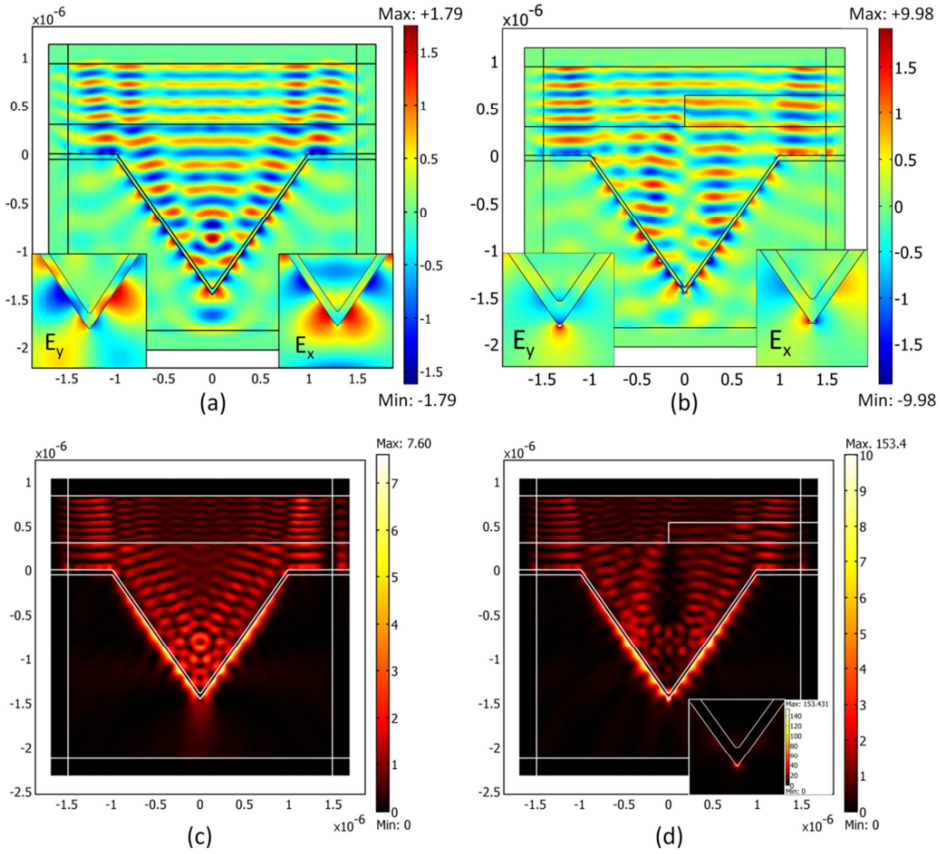

Figure 4.4 (a), (b) Full field simulated x component in the presence and absence of the phase shifter. Insets: zooms on the wedges edge; (c), (d) Field intensity maps. The fields are normalized to the amplitude of the impinging wave in vacuum. Note that in (d) the maximum field value is well above the maximum colorscale value. Geometrical parameters of the structure are the following: wedge height: 1.4 μm, metal thickness on the wedge sides: 33 nm, phase shifter thickness: 238.6 nm, curvature radius at the wedge edge: 5 nm. TM polarized light with vacuum wavelength λ = 390 nm impinges normally on the structures from above.

Thus, in order to obtain in-phase SPPs at the wedge ridge, the illumination condition must be adjusted. In particular, the wedge must be illuminated with π-out-of-phase light on one side with respect to the other side. This can be obtained with the setup shown in Figure 4.3 (b), where a step-like dielectric phase shifter is introduced immediately before the metal-coated wedge. Its height, *t*, is given by

$$\frac{2\pi}{\lambda} t \left| n_1 - n_2 \right| = \pi \tag{4.3}$$

being λ the vacuum wavelength of the impinging wave, n_1 and n_2 the refractive indices of the lower and upper media, respectively. In this configuration, SPPs generated on each side of the wedge approach the edge in phase and are thus expected to interfere constructively. As reported by several authors [1, 106], the field enhancement expected in this case is much higher than that obtained by the trivial sum of two SPP waves, because of the nanofocusing effect.

The final results can be visualized by comparing Figure 4.4 (a) and (c), relative to the configuration without a phase shifter, and Figure 4.4 (a) and (c), which refer to the phase-shifted configuration. Surface Plasmon dynamics is well visualized looking at the components of the electric field in the two configurations, with and without the phase shifter. As can be seen, light coupling to SPP modes takes place at both sides of the dielectric-silver interface, with low reflections. Without the phase shifter, SPPs reaching the wedge edge have opposite E_y fields and parallel E_x fields. SPPs destructively interfere at the tip and power is therefore coupled to propagating waves in the air domain. On the other hand, in the presence of the phase shifter, SPPs constructively interfere in a very small metal region close to the edge (see Figure 4.4 (b), insets).

After having identified the correct illumination conditions, the first issue we dealt with was finding the optimal combination of materials, metal thickness and incident wave vacuum wavelength in order to maximize the SPP coupling for a given wedge aperture. As will be discussed in the next section, wedge aperture is fixed to 70.4° by the chosen fabrication technique. This aperture angle limits the efficiency achievable with this structure [116], but leads to a very smooth surface in the final fabricated samples, which is crucial for the performance of the device. The dielectric material constituting the wedge is also fixed by experimental issues (NOA61), having a refractive index of ~1.58 at visible wavelengths. The upper material was then chosen to have a much higher refractive index, in order to obtain the desired phase shift within relatively small thicknesses, according to equation (4.3). Lead Zirconate Titanate (PZT) was chosen, having a refractive index of ~2.4 in the spectral range of interest.

As discussed in the previous section, that the curvature radius at the wedge edge crucially influences the extent of EM field focusing. The adopted nanofabrication technique allows to obtain a very small curvature radius, which in our case is about 5 nm. Therefore, also curvature radius was considered a fixed parameter. On the contrary, wedge dimensions, metal coating material and thickness and illumination wavelength were set as varying parameters in order to maximize field enhancement at the wedge edge. Concerning the wavelength, high efficiencies were found in the UV part of the spectrum. For the metal coating, gold and silver were considered. Silver turned out to give the best performance due to its lower dissipation rate at UV-VIS wavelengths, and the optimal metal thickness was 33 nm.

The already discussed Figure 4.4 refers to this optimal configuration; the optimized geometrical and physical parameter values are reported in the figure caption. As can be seen in Figure 4.4 (d), a remarkably high intensity enhancement at the wedge edge is predicted in the latter case, with a maximum enhancement factor around 150 (note that the maximum intensity value lies well outside the color scale range, see also the inset plot). On the contrary, no enhancement at the wedge tip is found in absence of phase shifter, as expected.

As reported above, the optimal metal coating for our wedges is Ag with a thickness of 33 nm. With these parameters, the best focusing performance occurs at a wavelength of 390 nm. Unfortunately, we are not equipped for near-field optical characterizations at this wavelength. Nevertheless, the experimental verification of the nanofocusing effect can be carried out also at higher wavelengths, even if a lower intensity enhancement is expected, which can however be related to the optimal case. We therefore repeated the simulations imposing a standard 514 nm laser light; in this case, Au turned out to provide better coupling.

4.4 Fabrication

The fabrication process of our wedge array requires the following steps:

- Focused Ion Beam (FIB) lithography;
- Wet etching;
- Au evaporation;
- Phase shifter integration;
- Replica molding.

A flowchart of the process is reported in Figure 4.5. A SiO_2 layer of approximately 500 nm was thermally grown on Si <100> in a hot furnace. This oxide layer was patterned by FIB lithography (FEI nova 600i dual beam). An array of rectangles (500 nm deep, 3 µm wide) was

fabricated with a single exposure over an area of 640µm x 640µm. After that, an anisotropic KOH wet etching was performed to obtain V-grooves defined by crystalline Si (111) atomic planes, thus obtaining the negative of the desired structure. The KOH etching along the (111) planes fixes the wedge aperture angle at 70.4°, as hinted in the previous section.

We should now evaporate a gold film on the substrate, which will eventually become the metal coating of the final structure. Since the low adhesion of Au on Si could be a serious drawback, the patterned grooves were previously oxidized in air for 5 hours at 1000 °C. Hence, e-beam evaporation of 33 nm Au was performed on the SiO_2 layer. The metallized grooves array was then used as a master for replication into NOA61 (transparent thiolene optical adhesive from Norland Optical Adhesives) by UV curing. Negative copies of the master, i.e. wedges, were thus obtained.

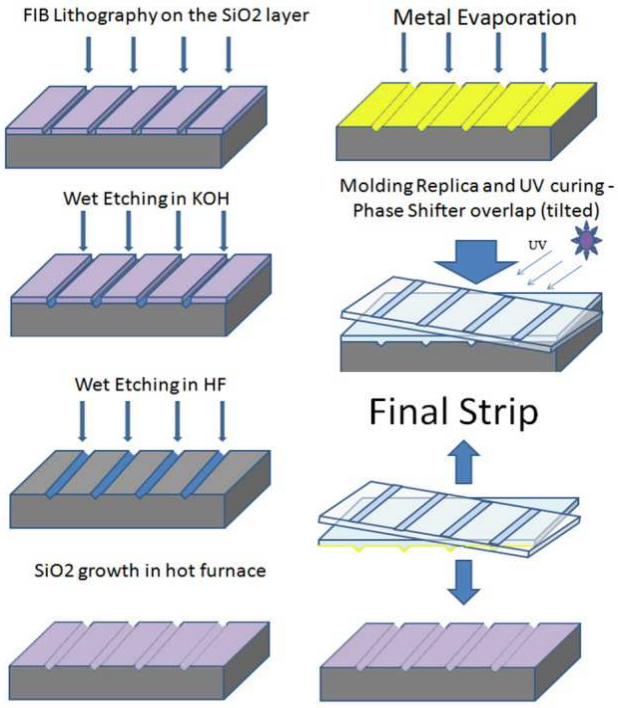

Figure 4.5 Scheme of the fabrication process.

As discussed above, a digital grating placed at the bottom of the wedge ensures the required phase shift between the two sides of the wedge. The phase shifter was fabricated by means of FIB lithography on a ITO/glass substrate, where a commercial PZT52/48 sol-gel solution (Inostek) layer with n=2.4 (@514nm) was previously spin coated at 3600 rpm and annealed at 300°C for 30 min. After repeating the spin-coating and baking process four times, the samples were annealed in a muffle furnace at 450 °C. The NOA61 refractive index is about 1.58 in the VIS spectrum; therefore the correct thickness of the phase shifter turns out to be 313 nm.

The integration of FIB patterned phase shifter grating with the grooves pattern was obtained by pressing a drop of NOA61 between the metallized Si master and the phase-shifter substrate, aligning the two patterns under an optical microscope and compressing the stack in a manual hydraulic press at 100 bar. After 10 minutes, UV curing is performed by illuminating the sample - still under pressure - through a transparent thick glass plate that acts as a top compression plate. The compression process is necessary to maintain a small (< 500 nm) distance between the wedge base and the phase shifter pattern. UV curing was performed using a 100 Watt UV flood lamp (SB100P spectroline) optimized for 365 nm wavelength. When performing the NOA replica, a stripping effect removes Au from the oxidised Si mold and covers the NOA wedges. This process allows to obtain wedge ridges with a radius of curvature below 5 nm, as can be seen in the inset of Figure 4.6.Figure 4.

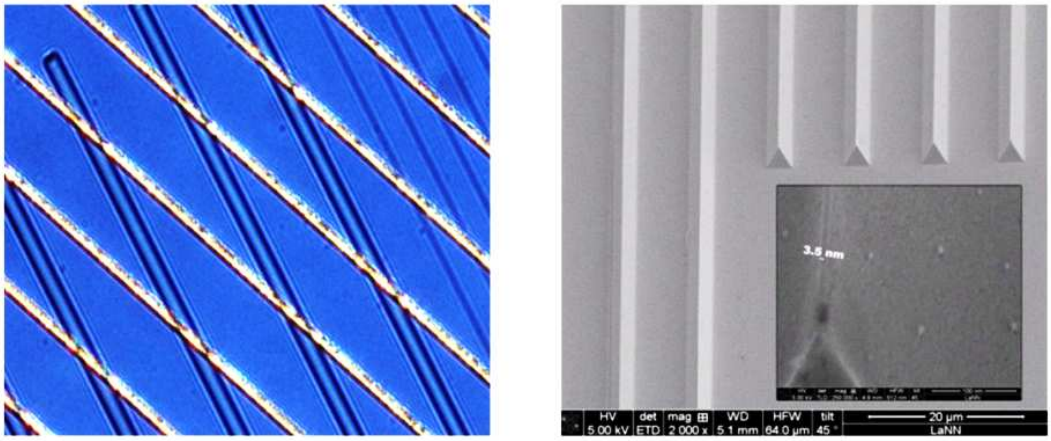

Figure 4.6 (a) Optical Microscope image of the final sample (b) SEM micrographs of the replicated nanowedge array. The inset shows a detail of the nanowedge tip, highlighting the extremely small curvature radius.

In Figure 4.6, optical (a) and SEM (b) images of the prepared wedges array are reported. In particular, the inset in Figure 4.6 (b) reports details of the obtained tip radius. It is worth to notice that the phase shifter pattern was intentionally rotated by around 25 degrees with respect to the wedge array before compression, so that the correct conditions for phase shifting exist only at the points where the wedge edges cross the phase shifter stripes (Figure 4. (a)). This approach allows to compare the behaviour of the structure in optimal and non-optimal configuration.

4.5 Optical characterization

4.5.1 Near-field Scanning Optical Microscopy (SNOM)

Experimental near-field characterization was performed by means of Scanning Near-Field Optical Microscopy (SNOM) [117] using a confocal Witec microscope equipped with a fibre-coupled 150 mW Ar^+ laser, providing a wavelength of 514 nm. The sample was illuminated from the backside with either unpolarized or TM-polarized light. An "apertured" metal-coated SNOM tip (cantilever type, see Appendix 1) was used to collect the spatial intensity profile of the wedges near-field. Figure 4.7 reports SNOM maps of light intensity over an area of 50µm x 50µm, showing the details on five wedges of the array. An intensity peak is observed at the wedges tip and a minimum of the intensity is present in correspondence of the phase shifter.

In order to better understand the experimental results, a FEM simulation of the interaction between the SNOM tip and the wedge structure was performed. A schematic SNOM tip was included in the simulation domain, together with the full wedge and phase shifter layout. The SNOM tip was modelled as an aluminum-coated hollow pyramid with a 100 nm-sized central hole. All the geometrical parameters of the wedge focusing structure were set to match the ones of the fabricated sample, in order to faithfully reproduce the results of the experimental characterization. Experimental dielectric constants were used for gold, obtained from ellipsometric measurements. We calculated the fraction of light power transmitted from the tip into the hollow pyramid, which models the SNOM intensity signal sensed by the detector. In Figure 4.8 we report the out-of-plane magnetic field H_z with and without the phase shifter. As can be seen, no signal is transmitted when the phase shifter is present (a), while a non-zero signal is transmitted in its absence (b). In order to simulate a SNOM scan of the wedge edge, the calculation was repeated for several y positions of the phase shifter with respect to the wedge symmetry axis. In particular, the initial and final phase shifter positions are set sufficiently far from the wedge edge position in order to reproduce the optical configuration of Figure 4.3 (a) in which no phase shifter is seen above the wedge structure.

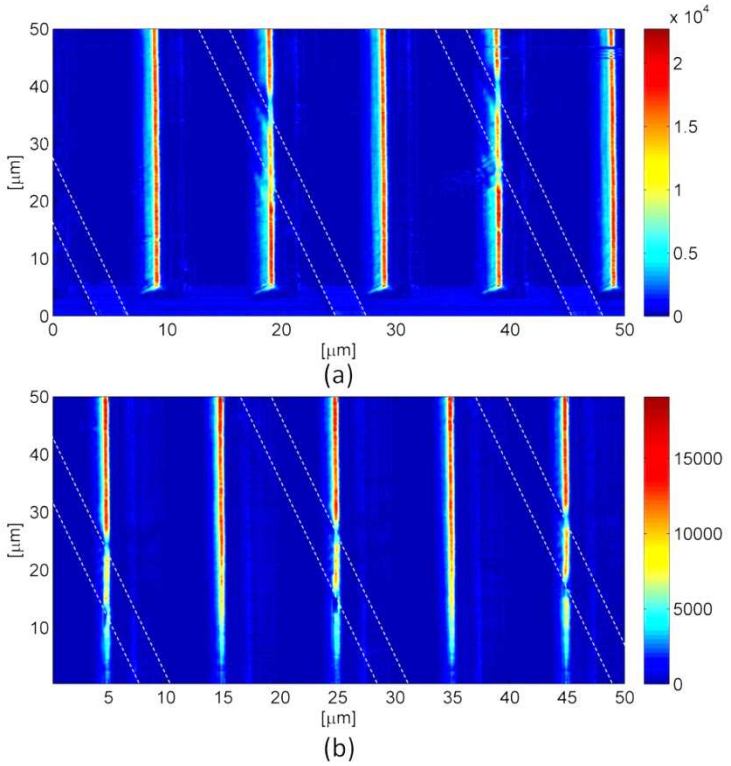

Figure 4.7 SNOM maps of the wedge array sample. The phase shifter is present and it is highlighted by the dashed lines. TM polarized 514nm light was used for illumination. (a) Unpolarized light impinging, (b) TM-polarized light impinging. The darker spots correspond to the intersection between the wedges and the phase shifter, the position of which is marked by the dashed lines.

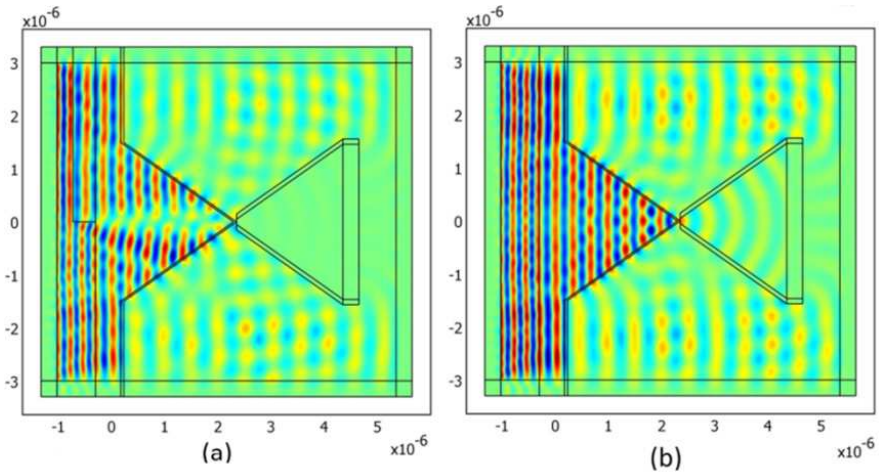

Figure 4.8 Simulated transverse magnetic field (H_z) distribution in the presence of a SNOM probe. (a) Configuration with the phase shifter; (b) Configuration without the phase shifter. The geometrical parameters of the simulations match the ones of the best fabricated sample.

The calculated power transmitted into the hollow pyramid as a function of the position of the phase shifter is reported in Figure 4.9 (a) (green line), taking into account the 25° angle between

wedges and phase shifter. A minimum SNOM intensity signal is predicted in presence of nanofocusing at the wedge edge.

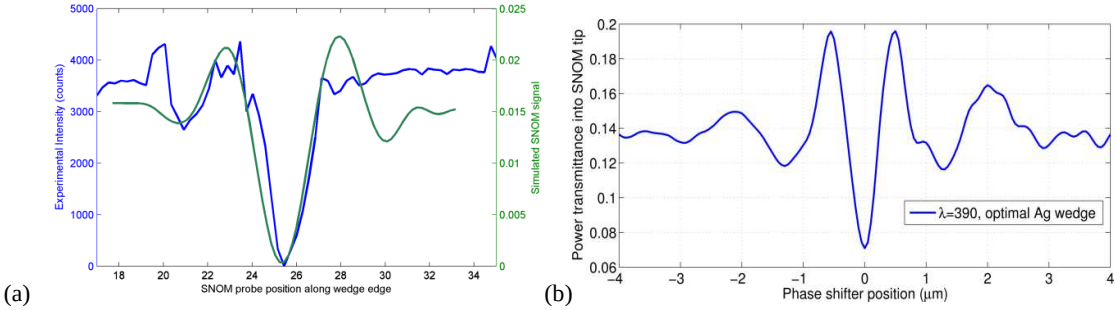

(a) (b)

Figure 4.9 (a) Comparison between experimental (blue) and simulated (green) SNOM signal along a wedge ridge. (b) Simulated SNOM signal along a wedge ridge at 390nm for the optimized structure.

This is somewhat counterintuitive, since it can be expected the SNOM signal to be sensitive to the near-field intensity and therefore being maximum in presence of strong nanofocusing at the wedge edge. However, it is well known that the SNOM probe often perturbs the near field distributions and the SNOM intensity map is the result of sample-probe interactions which are strongly correlated to sample morphology. Moreover, this result is confirmed by data reported in literature for aperture-tip SNOM measurements [118]. Figure 4.9 (a) we also report the experimental near field intensity measured along a wedge edge (blue line). As can be seen, the measured intensity when the SNOM probe passes over a crossing between a wedge and the underlying phase shifter exhibits a dip, the width of which is in good agreement with the simulation. From these data we can infer that the nanofocusing effect actually takes place at the wedge-phase shifter crossing, manifesting itself as a minimum of SNOM signal in correspondence of these points. For comparison we report in Figure 4.9 (b) the result of the same simulation performed with the optimal device layout described in Section 3.

4.5.2 Raman spectroscopy

In order to verify the field enhancement at the wedge tip, experimental analyses based on Raman/SERS were performed. Exploiting the fact that the SERS signal is local, proportional to $|\mathbf{E}|^4$, and roughly independent of the field direction, we expect an enhanced signal in correspondence of the intersection between the wedge ridge and the digital grating below.

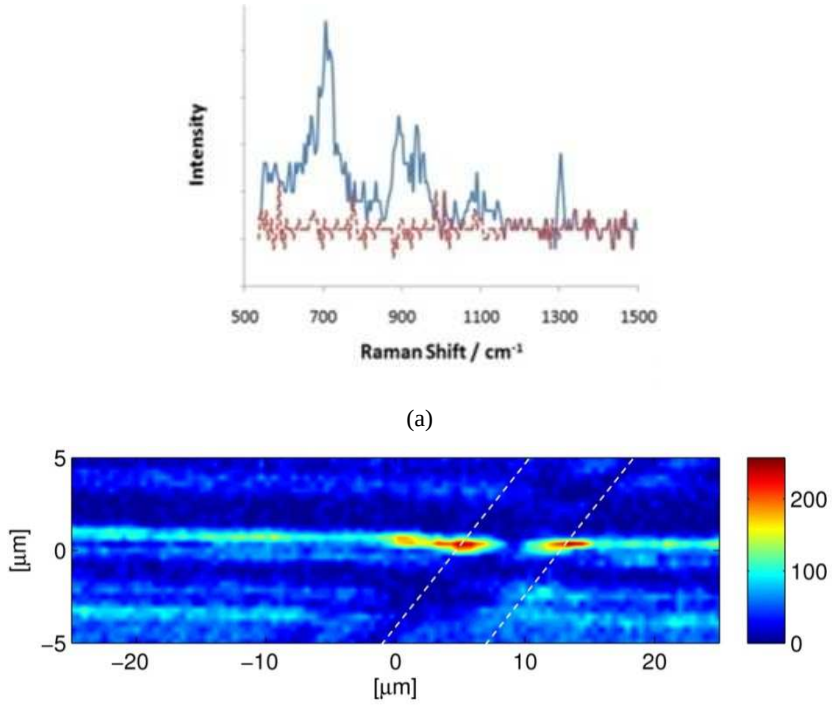

Figure 4.10 (a) Comparison between the Raman spectra obtained from a functionalized (blue line) and a bare sample (red line). (b) Raman map of a wedge. The intersection between the wedge and the digital phase shifter is highlighted and two intensity maxima are observed in correspondence of the intersection.

A wedge array sample was functionalized with a self-assembled monolayer of dodecanethiol ($C_{12}H_{25}SH$) deposited on the gold surfaces at room temperature. Samples were pre-cleaned in a basic peroxide solution (5:1:1 double distilled H_2O, 30% H_2O_2 and 25% NH_4OH) for 10 minutes, rinsed in double distilled water and dried under N_2 flux. The cleaned samples were immersed in a 4-mM solution of dodecanethiol in ethanol for 48 hours and therefore rinsed thoroughly with ethanol for at least 5 minutes, followed by drying under nitrogen stream. The spontaneous assembly of the molecules is known to form a densely packed and highly oriented structure on a metallic surface. The SERS spectrum of the functionalized sample was then measured by means of a confocal micro-Raman Witec instrument. The system is equipped with a 150 mW Ar^+ laser, fiber-coupled to the optical microscope and focused onto the sample surface by a 100x objective. The emitted signal is analyzed by a single grating spectrometer coupled to an Andor DU401 CCD detector, enabling the acquisition of local micro-Raman spectra. The spatial resolution is about 0.5 µm x 0.5 µm laterally and 1 µm in depth. SERS maps can be obtained by integrating the Raman peak signal for each point of a defined grid.

A map along a wedge ridge was collected integrating the Raman peak of dodecanethiol at $707cm^{-1}$ (υ (C-S) [119]). Figure 4.10 (a) compares the acquired spectra of a functionalized (blue

line) and a bare (red line) sample. Figure 4.10 (b) reports the result of this measurement showing the intersection between the wedge and the phase shifter.

As can be seen, two maxima are found as expected in correspondence of the crossing between the wedge and the underlying phase shifter. Actually, as can be seen, the measured Raman enhancement factor at the phase shifter-wedge crossings is rather small, around a factor 25. This reflects the non-ideality of the fabricated structure and is mainly due to the high losses in the gold layer. Nevertheless, the Raman measurement provides direct evidence of the nanofocusing phenomenon.

4.6 Conclusions

We have shown that a valuable nanofocusing effect takes place in a metal coated wedge configuration, provided that the correct phase-shifted illumination conditions are set and geometrical parameters are optimized. Gold coated NOA wedge arrays were fabricated by means of FIB and wet etching, obtaining good control of the wedge size and, most remarkably, a radius of curvature of about 5nm. The correct phase modulation at the wedge profile was achieved with a single step of imprinting. Finite Elements simulations of metal coated wedges were carried out, showing that these structures can effectively focus light at the nanoscale. The plasmonic nanofocusing effect was demonstrated by means of SNOM and Raman measurements, showing the strong potentialities of this system for nano-optics purposes.

Chapter 5

Let's twist to the nanoscale: sub-wavelength focusing of OAM-carrying light by means of Plasmonic Vortex Lenses

5.1 Introduction

In 1992, in a famous paper, Allen et al. [120] were the first to recognize that light beams with an azimuthal phase dependence $e^{il\phi}$, l being an integer, carry an angular momentum, given by the sum of a Spin Angular Momentum (SAM) and of an *orbital* angular momentum (OAM). The former, as was already well known, comes in amounts of $\hbar$ per photon, while the latter is quantized as $l\hbar$. This is expressed by [120, 121]

$$\frac{J_z}{W} = \frac{l+s}{\omega} \tag{5.1}$$

where s = ±1 is the SAM and, ω the wave frequency and W the energy. The OAM of light has of course a history prior to 1992, concerning for instance high-order atomic transitions. The key point of Allen was that this OAM was a natural property of all helically phased beams, and hence could be readily generated in a standard optics lab. These beams can be described in terms of solutions of the paraxial wave equation in cylindrical coordinates, which are known as Laguerre-Gauss (LG) modes. A plot of the phase of a $\mathbf{LG}_0^1$ beam and its intensity pattern are reported in Figure 5.1.

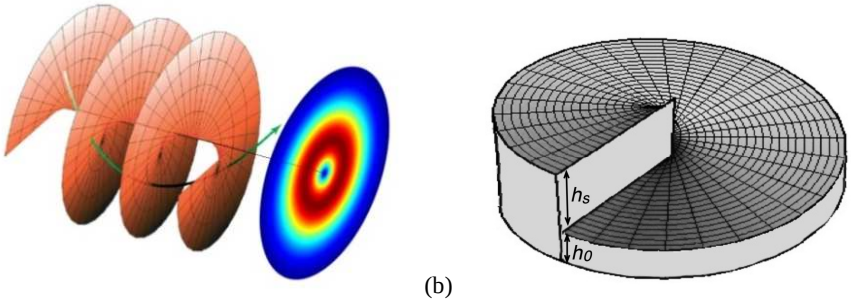

(a) (b)

Figure 5.1 (a) Helical phase of a Laguerre-Gaussian beam with OAM l = 1 and intensity cross section; (b) Model of a spiral phase plate, a device capable to impress an OAM contribution to an incident beam.

In recent years, several groups have proposed materials with special structural features, able to generate or modify OAM-carrying beam. In a work published in Microelectronic Engineering [122], we designed and fabricated a structure called spiral phase plate, an optical element made of glass and PMMA, the latter having an optical thickness which increases with the azimuthal angle (like a “spiral staircase”). If the height of the step is properly chosen, an incident plane wave emerges with a helical phase upon transmission. The plate was fabricated by gray-scale Electron Beam Lithography on standard positive resist PMMA.

More recently, extremely interesting new optical phenomena were discovered by combining OAM-carrying light and plasmonics. Some examples are plasmon-induced spin-orbit interactions [123, 124], optical spin Hall effect in nanoaperture arrays [125] and spin dependent plasmonic effects [126]. In particular, it has been shown that SPP waves carrying OAM can be generated by using particular metallic sub-wavelength structures illuminated by circularly polarized light. Structures such as concentric circular grooves [2] and Archimedean spiral shaped grooves [2, 127] were investigated. The SPP coupled by such structures is sometimes termed as Plasmonic Vortex (PV) [127] and structure itself is called a Plasmonic Vortex Lens (PVL). PVs are useful for various nanophotonic applications such as trapping [128], soliton [129], data storage [130], and quantum computation.

In this Chapter, we analyze PVL structures given by multiple-turns Archimedean spiral groove gratings or multiple concentric ring grooves. Such structures are able at a time to couple impinging circularly polarized light to Plasmonic Vortices and to focus them at the center of the structure, acting as lenses.

First of all, we will discuss the mechanism by which an incident wave is coupled to PVs and explore the focusing possibilities offered by PVLs in terms of field enhancement at their center. We will also describe the special case in which a hole is milled at the center of the PVL. As will be shown, a hole-guided mode can be coupled to the PV for proper geometrical parameters, therefore obtaining Extraordinary Optical Transmission through the hole. The proposed setup offers unique enhancement opportunities together with an easy-to-obtain experimental setup.

We will then describe the fabrication of such structures, performed by means of a combined EBL/FIB process. We fabricated PVL with different chiral and OAM properties in order to experimentally validate our theoretical studies and to explore different configurations for further application.

The characterization of the structures will also be presented. We illuminated the structures with circularly-polarized, collimated laser light and measured the intensity transmitted through the holes in different conditions and for different geometrical parameters.

Finally, we considered the possibility of placing a nanostructure inside the hole, in particular a rod-shaped antenna (or more than one) in different configurations. The exciting conditions and enhancement properties of the integrated system were studied and the structures were fabricated and the characterization is going on in these weeks, in collaboration with the Politecnico di Milano. The results will be presented in an oral talk at the well-known nanofabrication conference *Micro- and Nano-Engineering* (MNE) 2013, held this year in London.

5.2 The Archimedean Spiral PVL

Our PVL structure consists of a gold-air interface where an Archimedean spiral-shaped groove has been milled (Figure 5.2); SPPs are excited at this interface in the way we describe in the following. The geometry of the groove is defined by

$$r_m(\phi) = r_0 + m\frac{d}{2\pi}\phi \tag{5.2}$$

being ϕ the azimuthal angle, d the PVL pitch, m an integer and r_0 the distance from the center to the nearest point of the groove. The complete PVL consists of m spirals, each one rotated of 360/m degrees with respect to the adjacent ones. We will term these structures m-PVLs. We also notice that, in case of $m = 0$, the groove is a circular ring of radius r_0. Thus, we can consider the bull's eye structure, given by concentric ring grooves of period d, as a particular case of PVL.

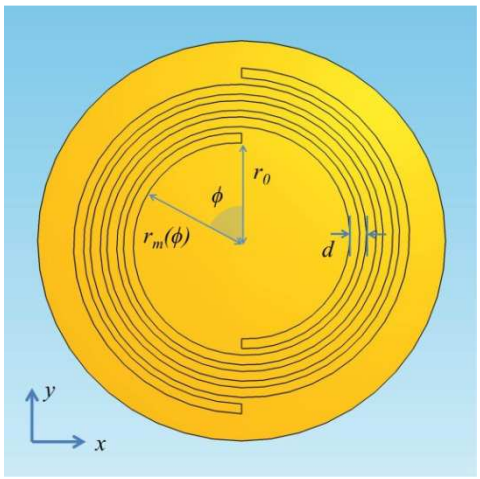

Figure 5.2 Plasmonic Vortex Lens (PVL) geometry.

We explain now how this nanostructured material can create an optical vortex. The simplest example is a circularly symmetric structure illuminated by circularly polarized light. Pioneering works on the angular momentum properties of the SPPs coupled in this situation were done by Hasman's group [126]. We know that, when a 1D grating coupler is illuminated by an arbitrarily polarized beam, SPP surface waves are excited via the TM component of light, and the propagation direction of the resulting SPP is perpendicular to the local direction of the grooves. Now, if circularly polarized light illuminates a circular groove, the optimal coupling to SPP occurs at diametrically opposite points of the groove, which rotate in time, following the electric field of the impinging light. Each spiral element produces a pair of SPP waves, traveling respectively toward the groove center and toward the outside. The wave has a space variant local direction and an azimuthally increasing phase: the origin of this phase is thus purely geometric and it is commonly referred as Pancharatnam-Berry phase [131, 132]. A sketch of the mechanism is reported in Figure 5.3.

In the case of the bull's eye, the geometric phase of the SPPs is only due to a polarization dependent coupling, resulting in a unity topological charge. In spiral structures, an additional phase arises as a result of a space-variant path difference and allows to impress an arbitrary topological charge to the resulting PV [127]. We notice that the groove spiral pitch must be equal to λ_{SPP} for the SPP generated at $\omega t = 2\pi$ to be in phase with that one generated at $\omega t = 0$.

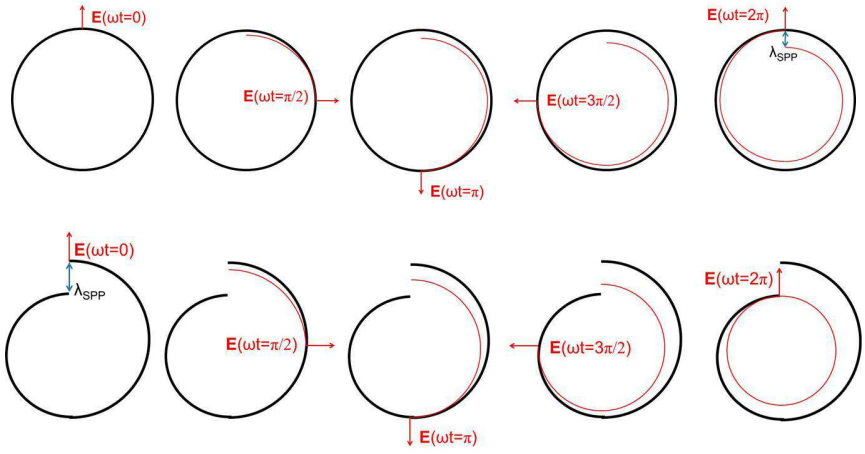

Figure 5.3 Principle of generation of PVs in Plasmonic Vortex Lenses (PVLs), above: circular groove illuminated by circularly polarized light (red arrow). The resulting PV has OAM=1. Below: spiral groove with pitch equal to the SPP wavelength illuminated by circularly polarized light. With the shown helicity, the resulting PV has OAM=0, and it will have OAM=2 in case of opposite helicity.

5.3 Field characteristics on a PVL

The characteristics of the SPP field pattern produced by the PVL are difficult to calculate analytically. Anyway, it has been demonstrated [133] that a reasonable approximation is:

$$E_{SPP,m}(R,\theta) \propto e^{ij\theta} J_j(k_{SPP}R) \tag{5.3}$$

here J_j is the jth order Bessel function and

$$j = s + l + m \tag{5.4}$$

is the total topological charge of the Plasmonic Vortex. The selection rule (5.4) was first reported by Kim and co-workers [127] for arbitrary value of m and light without OAM (i.e. $j = m \pm 1$), and just very recently [134] for light carrying OAM. The case $s = 0$ corresponds to a radially polarized beam.

Since the intensity of the field is described by a Bessel function, we expect an intensity pattern with bright and dark concentric rings. In particular, for $j=0$ a bright spot is expected at the center of the structure, while, for $j>0$, there will be a dark spot at the center and the intensity maximum will be on a ring, the radius of which increases with j.

The field intensity at the origin due to a single circular groove placed at a distance r_0 is

$$I_{SPP,0}(0,0) \propto r_0 e^{-2k''_{SPP}|r_0|} \tag{5.5}$$

The field enhancement due to N grooves can be computed by summing up all the contributions. The meaning of this behavior is clearly understood. At small values of r_0, the field concentrated at the center increases proportionally to r_0 since the groove length – and therefore the energy collected – increases linearly with the radius. This, however, is partially compensated by the natural SPP decay, and the enhancement saturates at some distance from the center, as can be seen in Figure 5.4, where we compare the analytical and numerical results. It is interesting to note that the saturation length turns out to be 228 μm for λ=780 nm and 29.5 μm for λ=633 nm, which are roughly 10 times the respective propagation lengths across the grating. This unexpectedly high contribution to the field enhancement from far grooves is due to the lens effect. Anyway, the plasmon decay length obviously has an effect on the overall achievable field enhancement and it is higher for NIR wavelengths. This decay length also depends on the materials, and it should be also born in mind that the it can be strongly decreased in presence of a rough surface. This issues will be addressed later when we discuss fabrication.

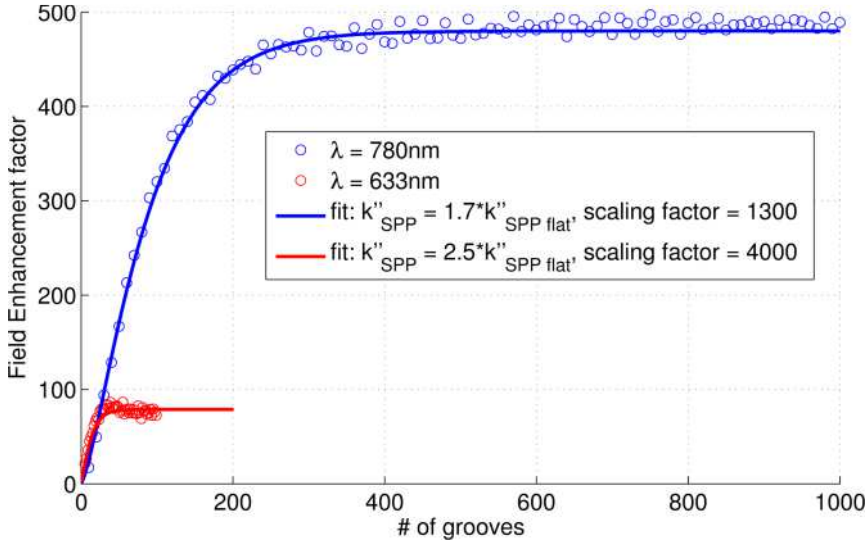

Figure 5.4 Field enhancements at the bull's eye center as a function of the groove number for λ=633nm (red) and λ=780nm (blue); FEM calculated values are marked with circles, solid lines are fits using expression (5.20). The grating period, slit/period and depth are as reported in Fig. 5.4-1 for λ=780nm, while for λ=633nm they are 590nm, 0.5, and 30nm, respectively.

5.4 Optical transmission through a holey PVL

We then considered a holey PVL, i.e. a PVL where a hole has been milled at the center. Extraordinary Optical Transmission (EOT) occurs in this situation. Although EOT through a single hole surrounded by a bull's eye structure has been discussed in literature, in most of the works only plane-wave, linearly polarized illumination is considered, probably due to the relative difficulty of producing other illumination setups, such as radially polarized light beams. With our structure, on the contrary, it is possible to obtain axially symmetric SPPs converging to the center using standard circularly polarized light.

We consider the case of a 200 nm thick gold PVL on a glass substrate, assuming λ=633 nm and λ=780 nm impinging light wavelengths and we studied its behavior numerically. The results are reported in Figure 5.5 (a) and (b).

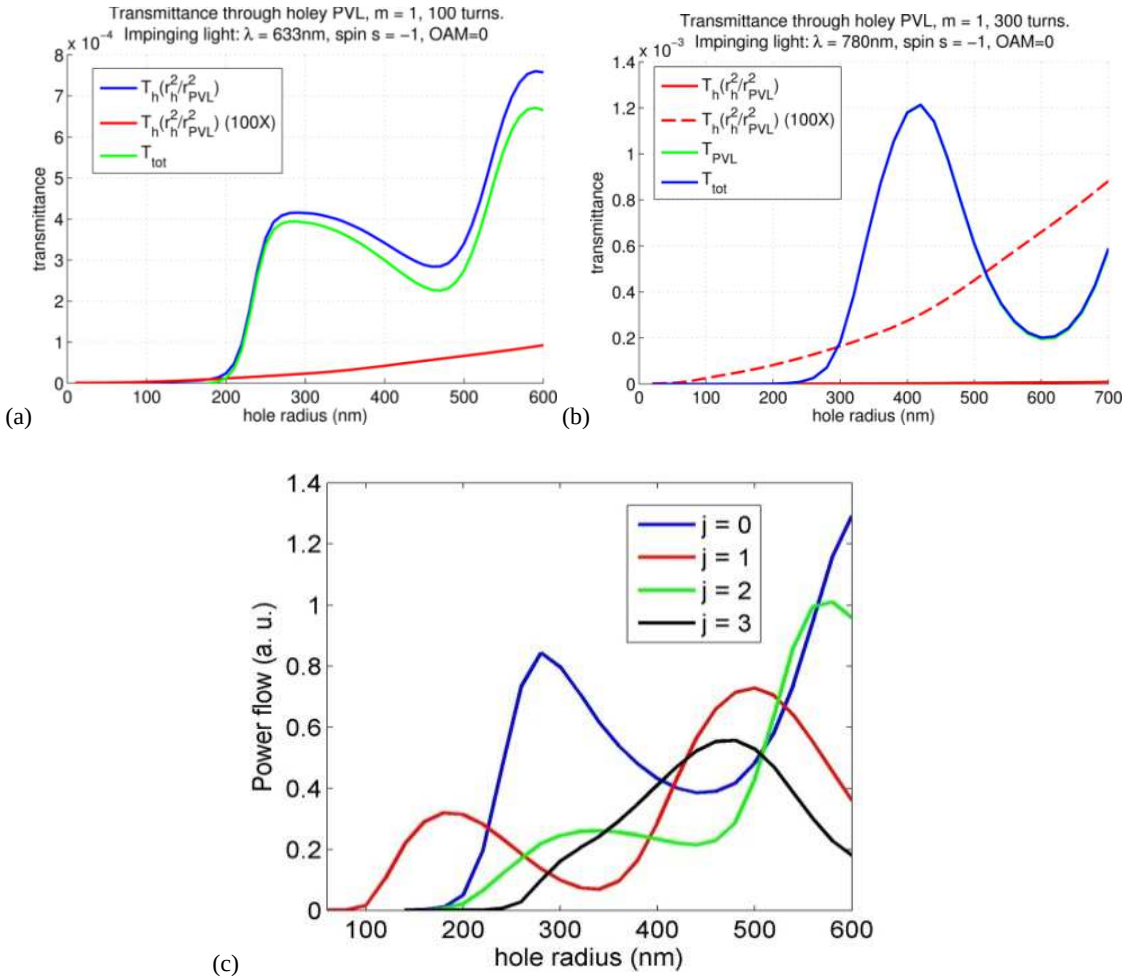

Figure 5.5 Transmittance of holey 1-PVLs illuminated by circularly polarized light *s*=-1 (coupled PV has *j* = 0). (a) λ=633 nm; (b) λ=780 nm. The geometrical parameters of the grating were optimized for efficient plasmon coupling. (c) Power flow as a function of hole radius for different values of the overall OAM. This plot allows to identify the radii at which light is focused for different values of j. The results refer to a wavelength λ=633 nm.

For λ=780 nm, the PVL strongly boosts the transmittance at a hole radius of 400 nm, resulting in a total transmittance that is roughly 600 times higher than that of the single hole. The enhancement is more modest, but still significant, for λ = 633 nm at a hole radius of 300 nm. The maximum of the curves corresponds to the optimal coupling to hole guided modes. In Figure 5.5 (c) we compare the transmittance for different values of the topological charge of the PV as a function of the hole radius.

It is interesting to describe the characteristics of the field inside, and transmitted through, a holey PVL; in particular we focus on the in-plane components (E_x, E_y) of the electric field. In a recent work by our group [135], we demonstrated that, while these components are small in SPP waves travelling at the metal-air interface, their magnitude is dominant in the region within the

hole, and the E_x and E_z components of the outgoing structured wave have the same order of magnitude. The x-y cross sections show field patterns similar to the ones generated by a rotating electric multipole [28] of order 2^j. The PV generated at the upper metal–dielectric interface induces such a rotating multipole charge distribution at the upper hole edge, which propagates down to the lower hole edge [123].

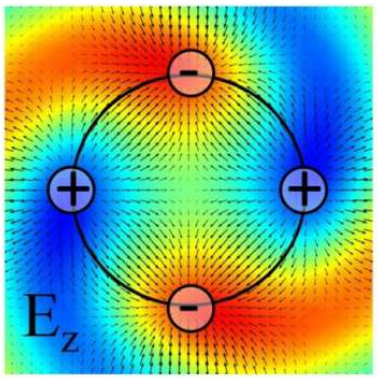

Figure 5.6 E_z field distribution at 50nm under the lower hole edge (color scale) and scheme of the corresponding surface charge distribution at the metal surface in case of j =2.

5.5 Fabrication

We fabricated a series of holey *1*-PVL and *2*-PVL, either left- or right-handed, for λ=633 nm. The geometry of the structure was optimized by FEM simulations. In particular, the parameters affecting the response of the PVL are the period, the duty cycle, the depth of the grooves, the overall thickness of the gold slab, the distance (r_0) from the nearest point of the groove and the hole radius. The optimal parameters found in our case are reported in Table 5.1.

Period	**Duty cycle**	**Groove depth**	**Overall thickness**	**Distance r_0**	**Hole radius**	
λ_{SPP} = 570 nm	50%	35 nm	250 nm	λ_{SPP}+hole rad.	j=0	300 nm
					j=1	180 nm

Table 5.1 Optimization of the PVLs used in our experiments. The working wavelength was 633 nm.

The optimal constants of the material constituting the PVL are also crucial. We therefore used ellipsometry to measure the refractive index of the gold we would actually use in the

fabrication, we implemented the curves in the COMSOL software and used the experimental values for our simulations. These curves are shown in Figure 5.7.

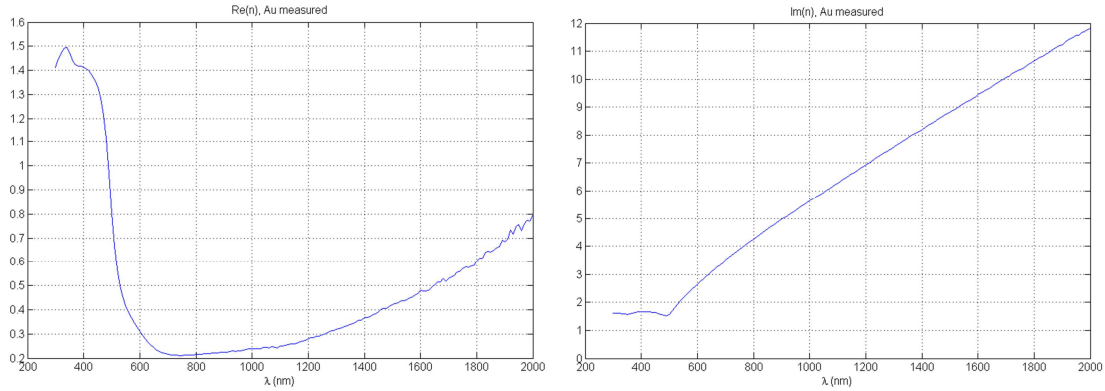

Figure 5.7 Measured real (left) and imaginary (right) part of the refractive index of the electrolytically grown gold used in the experiments.

Before fabricating our PVL structures, we checked the validity of our optimization by fabricating a linear grating with the same parameters. We measured its reflectivity using a spectroscopic ellipsometer and compared it with the one predicted by simulations. Since we cannot perform a reflectivity spectrum at an angle of incidence of 0° - the illumination condition required by the PVL design - we calculated the expected reflectivity at 15°, which is the minimum value that can be set in our ellipsometer. The observations can then be related to the 0° condition. The results are reported in Figure 5.8.

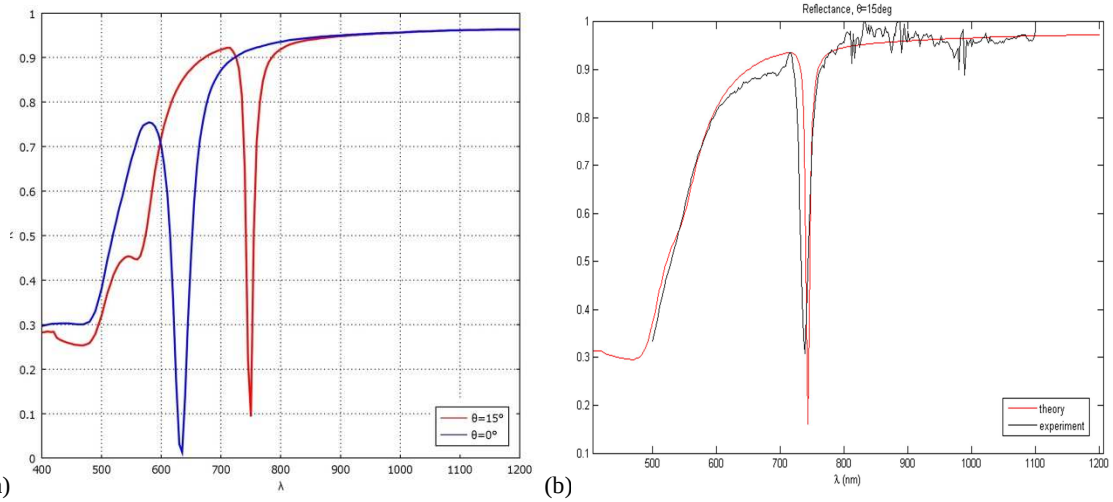

(a) (b)

Figure 5.8 (a) Calculated reflectivity spectrum of a digital gold grating having the same geometric parameters of the PVL, at an incidence angle of 0° (blue curve) and 15° (red curve). (b) Comparison between the measured (black) and calculated (red) reflectivity spectra at 15° (minimum angle which can be set in the ellipsometer). We find a good agreement between theory and experiment, even if a slight blue-shift and lowering of the depth is observed, probably due to a decreased effective thickness caused by surface roughness.

As expected, we find a dip in reflectivity at about 750 nm. A slight blue-shift and lowering of the depth in the experimental curve, probably due to surface roughness, which may lower the effective thickness of the fabricated grating. Anyway, for our purposes, the dips are superimposed well enough and so we can expect that an SPP is actually coupled at the grating-air interface.

We then fabricated our PVL samples. The fabrication process consists in three steps:

1. Substrate preparation;
2. Electron Beam Lithography, to generate the PVL structure;
3. Au deposition, performed by electrolytic growth;
4. FIB milling of the central hole.

A 200 nm-thick slab of gold was electrolytically grown on an ITO-coated glass slide (ITO thickness 15-30 nm, nominal), by applying a voltage of -0.75 V for 5 minutes. A thin (2-3 nm) layer of Au was preliminarily sputtered onto the ITO surface to improve its conductivity, by cycling the sample for 35s at 10mA in a sputtering machine. We then deposited 90 nm of commercial PMMA resist (AR-P 671.02) onto the surface by spin coating (4000 rpm, 60 s) and soft-baking at 180° for 10 minutes.

Electron Beam Lithography was then performed on the sample, using a dose of 570 $\mu C/cm^2$ which was optimized via a dose metrics. The pattern consisted in two lines of PVLs; in each line the period was varied around the central value foreseen by simulations, and the two lines had opposite chirality. All the other parameters were set according to the simulations.

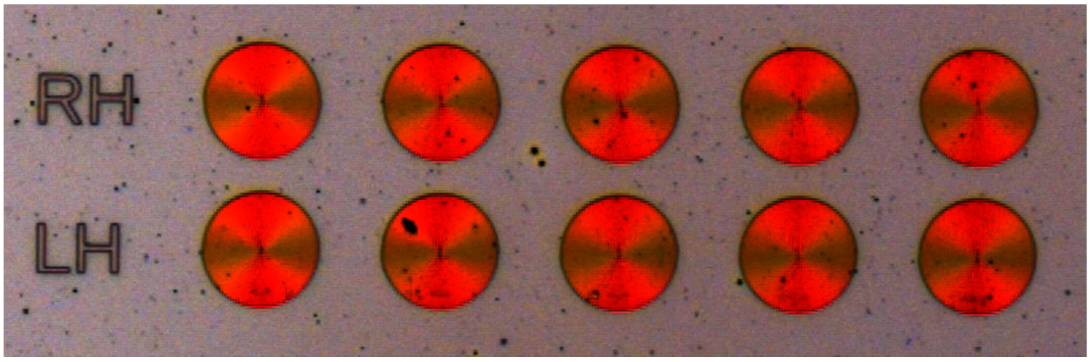

Figure 5.9 Optical microscope image of a part of the pattern used for the “holey spiral” experiment. The picture refers to m=2 spirals. The two lines have opposite chirality (right- and left- handed) and the period is varied around the optimal value.

The PVLs also contained a hole in the middle. This is not the final hole (it will not be a "real" hole since it will "end" on the underlying Au film) but it was used as a marker for subsequent FIB milling. The same layout was used for *1*- and *2*-PVLs. The PVLs had 50 grooves since this is approximately the value at which the PVL enhancement reaches saturation, according to the plot in Figure 5.4; we also fabricated *1*-PVLs with increasing number of grooves to verify the enhancement trend.

The exposed sample was developed in a 3:7 deionized H_2O:IPA solution for 20 s and rinsed in deionized H_2O for 30 s. After that, electrolytic growth was performed to obtain the final PVL structure. We used the same growth parameters as before, but we used a growth time of 20 s to obtain a final thickness of 35 nm. Unexposed resist was then removed by dipping the sample in hot acetone for 3 minutes and then rinsing it with cold acetone and isopropanol. Some examples of the structures obtained after this step are shown in Figure 5.10.

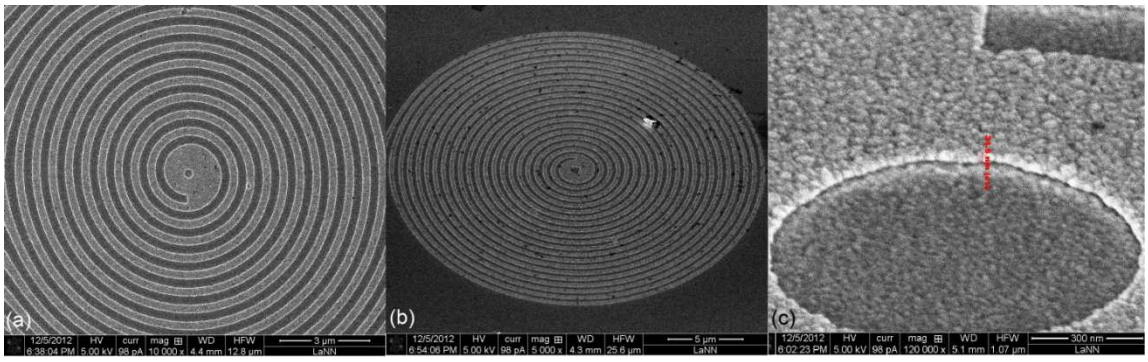

Figure 5.10 SEM pictures of some fabricated chips after EBL exposure and development. (a) Right handed 1-PVL; (b) Tilted image showing a complete *1*-PVL with 20 grooves; (c) detail of the central hole, showing a thickness of 35 nm.

The fabricated sample was then put in our FIB system for milling of the central hole and we thus obtained the final structures, which are shown in Figure 5.11.

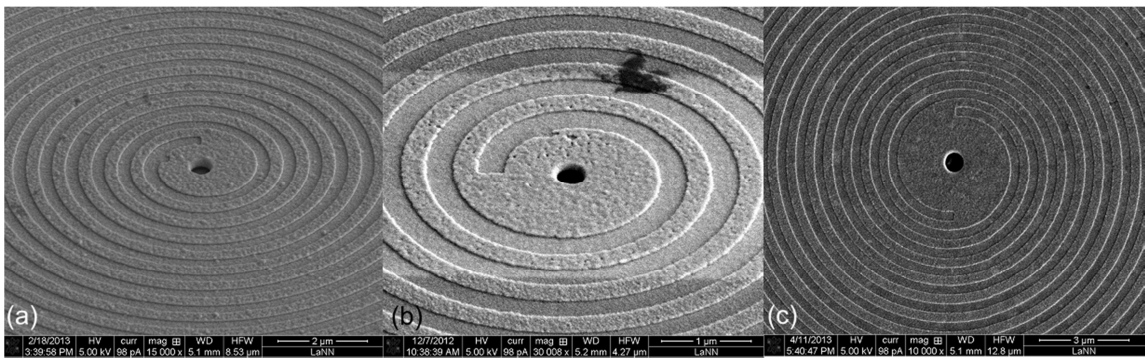

Figure 5.11 SEM pictures of some fabricated chips. (a) Left- and (b) Right-handed *1*-PVL. (c) RH 2-PVL.

5.6 Characterization

To characterize the sample we used a Witec instrument equipped with a confocal microscope, in which we had the possibility of adjusting the optical path and illumination conditions according to our needs. We illuminated the sample from the spiral side with collimated laser light at 633 nm. The beam passed through a linear polarizer first, then through a quarter wave plate, thus impinging on the sample with circular polarization which can be changed from right- to left-handed (s=±1) by rotating the plate. Light emerging from the hole on the other side was then collected using the microscope objective and recorded by a CCD camera.

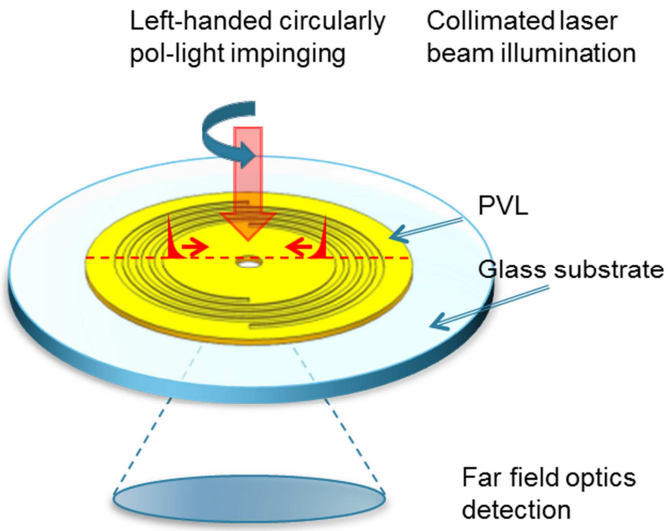

Figure 5.12 Scheme of the experimental setup. The spiral represented here is a 2-PVL.

Figure 5.13 shows the results for *1*-PVLs. In Figure 5.13 (a) the measured intensity is plotted versus the spiral period; the measurement was performed for each of the two chirality lines, without changing the optical path or the wave plate position. For left-handed[3] spirals having m=*-1*, thus providing j=0 with s=*+1*, the trend follows that predicted by simulations (Figure 5.13 (d)), and a maximum is observed with a period of 570 nm. For right-handed spirals (m=+1, thus j=2 with s=+1), the signal is substantially constant and suppressed with respect to the former case. In particular, it is comparable to the one due to light directly passing through the hole. For j=2, in fact, a minimum is present at the PVL center. The maximum lies on a ring

[3] Here we define "right" and "left" handedness as "seen" from the incident light.

which radius is larger than the hole, and it is not transmitted. The ratio between the two signals is a factor 4.

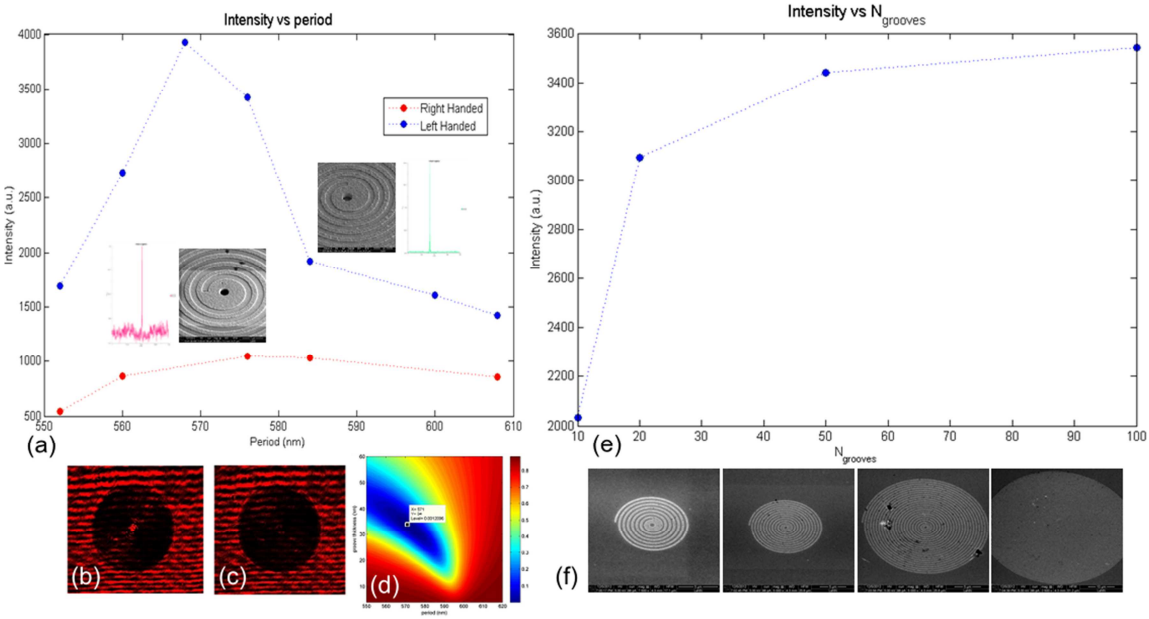

Figure 5.13 (a) Transmitted intensity through the hole as a function of period. The trend follows that predicted by simulations (d) and the ratio between this signal and the intensity directly transmitted through the hole (optical images shown for (b) left-handed spiral, (c) right-handed spiral) is a factor 4. (e) Transmitted intensity as a function of number of grooves. SEM pictures are shown in (f).

Figure 5.13 (b) and (c) show microscope images of the same m=-1 spiral, for two opposite positions of the wave plate; here the PVL properties are kept fixed while the illumination conditions are changed, since polarization is switched from s=+1 to s=-1. A bright spot can be seen for j=0 (b) while the center is dark for j=2, as expected. Figure 5.13 (e) reports the intensity trend measured on spirals of increasing number of grooves; some SEM pictures of these grooves are reported in (f). The trend reproduces the one predicted by theory and simulations, reported in Figure 5.4. The smaller overall enhancement factor is probably due to surface inhomogeneities and roughness. However, the effect is clearly proved.

We repeated the experiment for *2*-PVLs. In this case, we expect a bigger difference between the two possible cases of j=1 and j=3, as can be easily seen by looking at Figure 5.5 (c) and considering the best hole radius for j=1. Figure 5.14 summarizes the expected response.

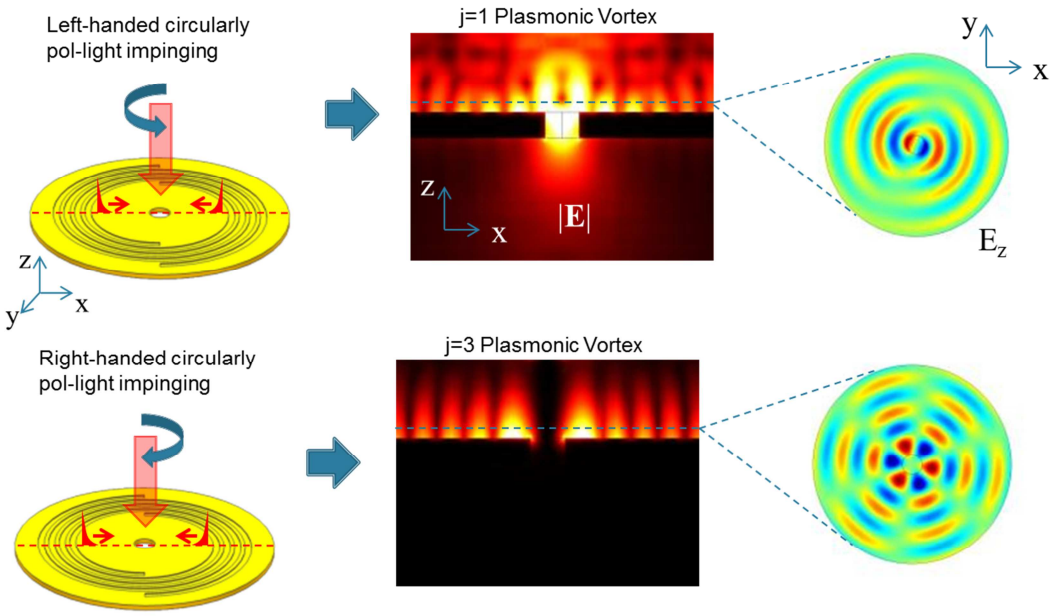

Figure 5.14 Expected response of 2-PVLs illuminated by circularly polarized light. Left: Scheme of the optical setup and effect occurring on the structures, for a RH spiral. Upper line: For LH circular polarization; Lower line: for RH circular polarization. Center: Electric field norm expected in the two cases, calculated by FEM simulations. For j=1 light is transmitted through the hole, while for j=3 the maximum lies outside the hole diameter and the center is dark. Right: Transverse component of the electric field in the near field of the PVL.

Figure 5.15 reports the experimental results. Figure 5.15 (a) shows two frames of a video recorded by a CCD coupled to the Witec microscope, while the quarter wave plate (QWP) was rotated. The two frames correspond to "opposite" positions of the QWP, resulting in LH or RH circularly polarized light, respectively. The two spirals shown in the frames have opposite chirality and thus one is "on" for LH polarized light, the other is on for RH polarized light. Figure 5.15 (b) reports the intensity measured on LH- and RH-polarized spirals of different periods. A maximum is observed for a period of 565 nm (expected: 571 nm) in the case *j*=1, corresponding to LH spirals in the illumination conditions considered. For j=3, the signal is much lower at this value of the period (a factor 100), while the two signals are comparable for periods out of the resonance, reported in the map in Figure 5.15 (c).

This result confirms the effectiveness of our design and demonstrates the possibility of controlling the OAM properties of light at the nanoscale. Therefore, OAM appears to be a powerful tool to control both static and dynamic properties of light in the sub-wavelength regime.

Further near-field characterization is reported in Chapter 6.

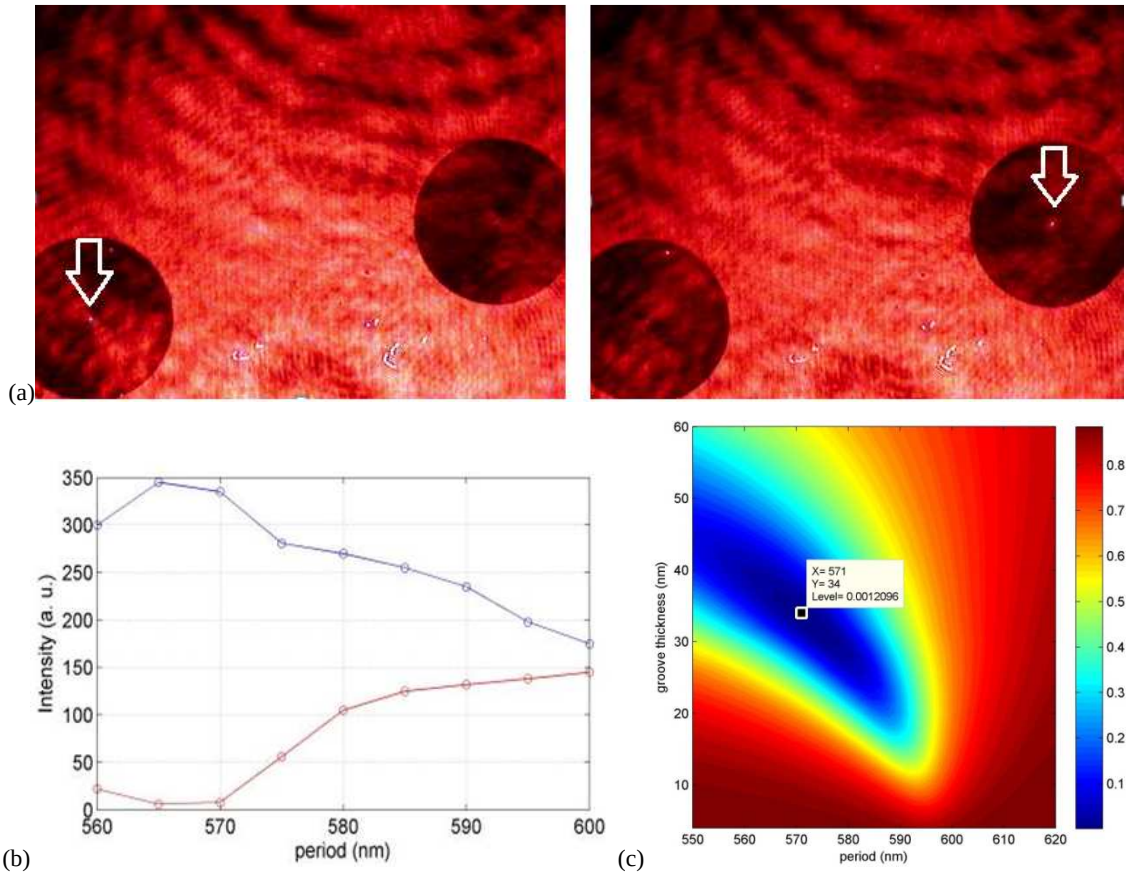

Figure 5.15 (a) CCD-recorded optical images of two 2-PVL of opposite chirality, upon rotation of the quarter wave plate. In each case, only one of the two spiral centers is illuminated (white arrows), while the other one is dark. The situation for which the center is bright corresponds to j=1, while for j=3 the intensity maximum falls on a ring lying out of the central hole and is not transmitted. (b) Measured intensity as a function of the period (expected best: 570 nm). The ratio between *j*=1and *j*=3 is a factor 100 at the period providing the maximum enhancement for *j*=1 (565 nm), while for periods far from the resonance the two signals are comparable. (c) Map showing the expected reflectivity as a function of period and thickness.

5.7 Integration of a nanoantenna inside a holey PVL

After having thoroughly studied and experimentally characterized the behavior of holey PVLs, we wondered what happened if we placed a nanostructure inside the hole. In the hole, in fact, there is basically an in-plane electric field and thus we expect that planar nanostructures which can be excited by such a field can be set on. There are two interesting aspect about this planar field: it is greatly enhanced, and it carries OAM. We therefore decided to study the coupling between a holey PVL and a nanoantenna, a structure we know very well from our SERS/SECARS studies. In fact, nanoantennae are excited by the in-plane field component

along their major axis; moreover, they are small enough to be comfortably placed inside the hole of a PVL.

To study the coupling between a holey PVL and an antenna, numerical analysis was performed, using the Finite Element Method. The geometrical parameters of the PVL were optimized for efficient plasmon coupling at λ=780 nm; we chose this wavelength since it is the common working wavelength of our nanorod antennae. The geometric parameters of the nanorods were already known but were checked, since the illumination conditions are different from the standard plane wave. We limited our study to the case j=1; the simplest way to obtain that is to use a bull's eye structure. As hinted in Section 5.4, in this case a rotating dipole is induced at the hole edge, as shown in Figure 5.16 (a). It is intuitive to understand that, for optimal coupling, the antennae should be arranged inside the hole following the field lines; the antennae must thus be arranged in radial fashion. Figure 5.16 (b) shows the electric field norm on a single nanorod placed inside the hole; the rod is clearly excited and a field concentration can be seen at its ends. The field enhancement of the PVL-antenna integrated system is quantified in Figure 5.16 (c). It is well-described by the product of the constant enhancement of the rod and that provided by the PVL, which depends on the number of grooves.

Although this approach is not suitable for standard sensing experiments where a large number of resonators are preferable, it might be interesting for more challenging issues such as single molecule detection.

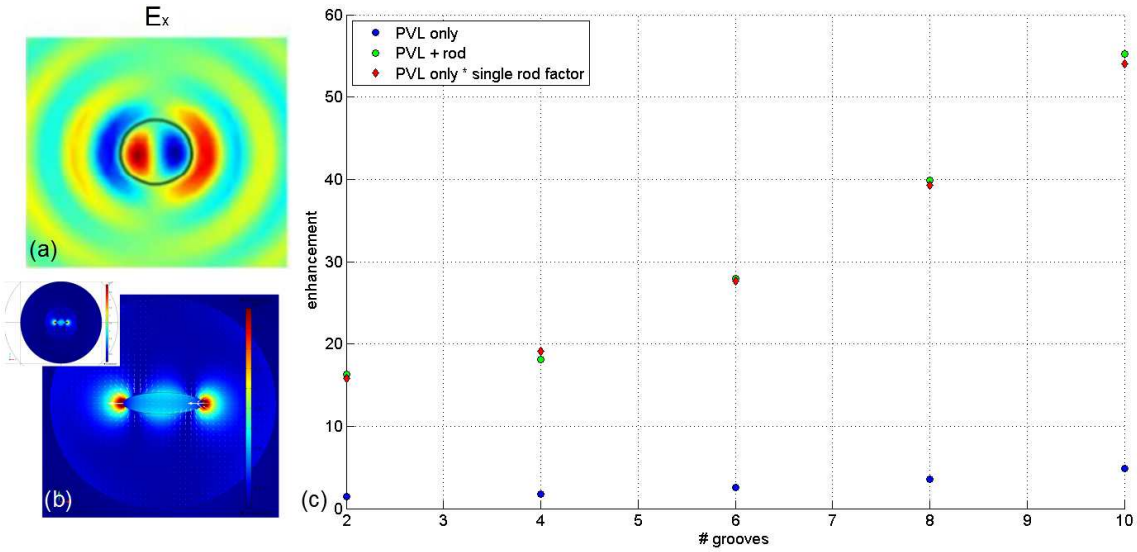

Figure 5.16 (a-d) Different possible antenna configurations for 0-PVLs, together with the x-component of the electric field. (e) Field enhancement factor (EF) of a 0-PVL coupled to a nanorod. It is given by the product of the EFs of the two structures.

The structures were then fabricated by EBL with a two-step overlay exposure. In the first step we exposed pillars in a 400-nm thick negative tone resist (AR-N 7520.073). The exposed structures were developed in a mixture of the standard negative resist developer AR 300-47 and DI H_20 in a ratio of 4:1 for 150 s. Gold was electrolytically grown for 2 min and residual resist was removed by dipping the substrate in the commercial remover AR 300-70, thus obtain holes in a gold slab. Together with the pillars, we exposed global and local marks, which shall be used for alignment in the 2nd step. We then re-aligned the system and we exposed the bull's eye around the hole and nanoantennae inside the hole, using standard positive resist (PMMA, 90 nm thick). Both steps were performed in high-resolution mode. The metallic structures were then obtained by a second electrolytic growth step (voltage -0.75 V, growth time 20 s). Some of the fabricated structures are shown in Figure 5.17.

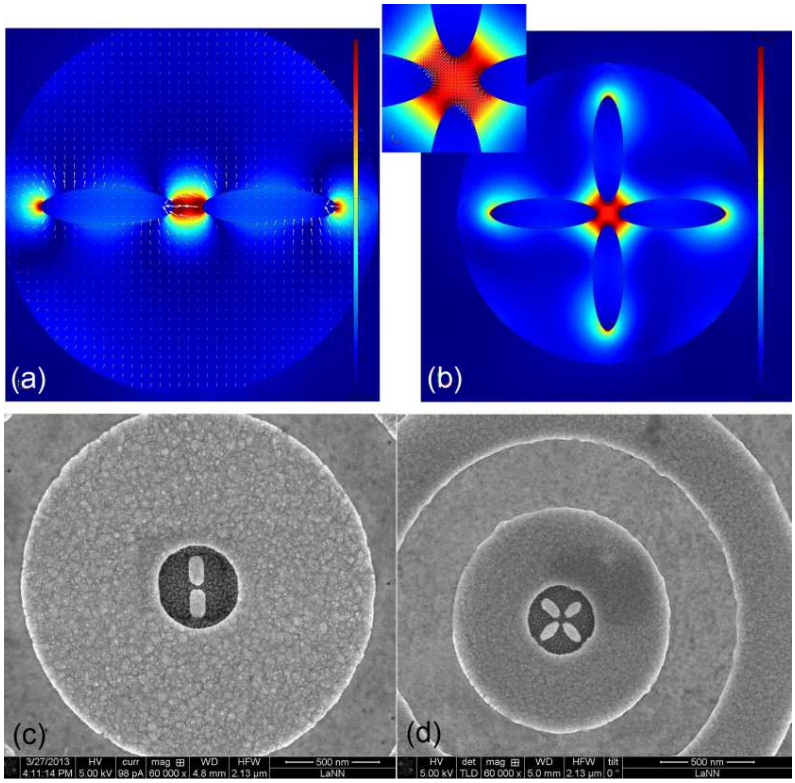

Figure 5.17 Integration of a nanoantenna inside a holey PVL. (a, b) FEM simulations showing the electric field norm (color scale) and in-plane field (white arrows) inside the hole (slice at half nanorod thickness), for an antenna dimer or tetramer, respectively. (c, d) Fabricated chips corresponding to (a) and (b). The chips were obtained by EBL overlay exposure in high resolution.

In principle, these structures could also be fabricated with a single-step EBL exposure followed by FIB milling of the hole and the antenna together, or by Au deposition in the SEM (allowed by our FEI system) inside the hole, upon FIB milling. However, this process cannot

ensure the geometry and positioning control provided by EBL, and this is even more true with such tiny structures. As an example, we report in Figure 5.18 the best structures we could obtain with FIB milling of the antenna/hole, compared with the typical ones obtainable with the EBL overlay process: the quality of the latter structures (shape, dimensions) is much higher.

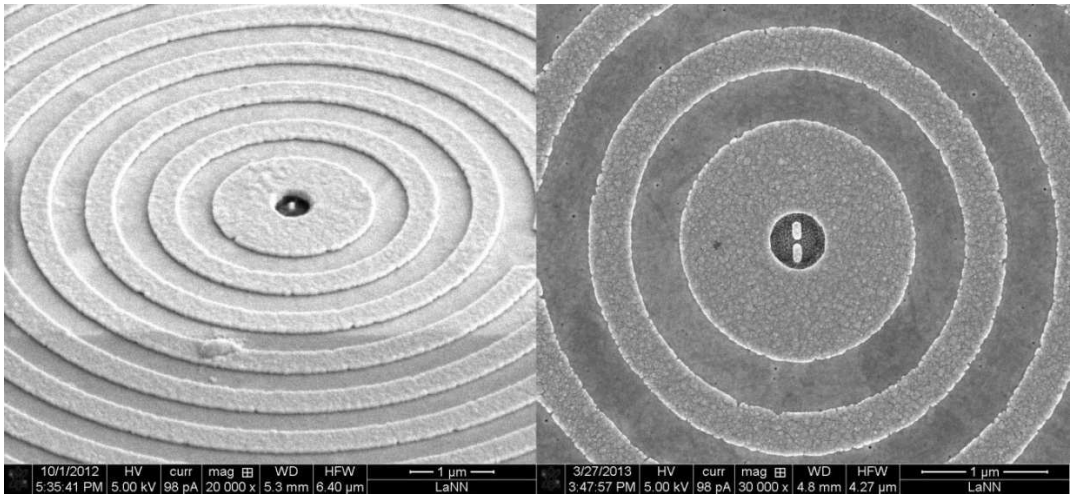

Figure 5.18 Comparison between a nanorod antenna fabricated by (a) single EBL exposure + FIB milling of the hole + antenna pattern and (b) EBL overlay exposure (b). The quality of the latter structure is clearly much higher, the antennae having a well-defined and reproducible shape and dimensions.

These results will be presented in an oral talk at the MNE (*Micro- and Nano-Engineering*) 2013 conference held in London, UK from 16th to 19th September 2013. In the meantime, fluorescence and Raman experiments will be performed in collaboration with the Politecnico di Milano.

5.8 Conclusions

We studied a class of nanostructured plasmonic surfaces able to efficiently couple impinging circularly polarized light to Plasmonic Vortices, i.e. SPPs carrying orbital angular momentum (OAM). Such structures are multiple turns spiral or circular grooves milled in a thick Au slab, and are termed Plasmonic Vortex Lenses (PVLs).

We described the mechanism by which these structures can couple an incident wave to PVs and the characteristics of the field focused at their center. The effect depends on the geometrical and structural characteristics of the nanostructured surface (plasmon decay length, type of metal, geometry of the groove, chirality), as well as the characteristics of the impinging light (wavelength, polarization). We also considered the configuration in which a hole is milled at the

center of the PVL. A huge EOT effect can be obtained with an experimental setup which is much easier than the standard ones proposed in literature.

We then fabricated different PVLs by means of EBL, followed by electrolytic growth and FIB milling. This simple yet precise process allowed us to obtain structures with the desired characteristics, with a very good control on all the parameters, which could thus be tuned.

We optically characterized the PVL, illuminating them with circularly-polarized laser light and measuring the intensity transmitted through the holes. We retrieved the results predicted by our simulations, thus obtaining an “EOT switch” by simply rotating a quarter wave plate.

Finally, we studied the integration of one or more nanorods inside a holey PVL; in the hole, in fact, the electric field is mainly in-plane and can excite such nanostructures. We studied the simple configuration of a nanorod inside a bull’s eye structure, illuminated in such a way that we have an electric dipole at the hole edge. Different antenna configurations were considered and fabricated. This device is a non-trivial integration of different optical phenomena, namely SPP traveling on a grating, nanofocusing of light, OAM properties of light, EOT and LSPR.

Chapter 6

EllipsSNOM: an innovative instrument for combined near- and far-field characterization

6.1 Introduction

The detection of SPPs can be performed by either far-field or near-field techniques. While the former allow to reveal macroscopic effects, such as a dip in a reflectivity spectrum, the latter - among which SNOM is the most famous - allow to directly image an SPP propagating at the surface.

Despite its age, optical microscopy is probably still the most popular microscopy technique. It is fast, cheap, provides a wealth of information and allows to investigate samples at ambient conditions. Since the half of the 19th century, however, scientists have been aware that the diffraction of light in small apertures (holes or edges of particles) limited resolution to the wavelength of light. This fundamental limit, derived by Abbe and also known as the Rayleigh criterion, states that [136]

$$R = 0.61\frac{\lambda}{NA} \tag{6.1}$$

where R is the smallest resolvable distance between two objects, λ is the wavelength of light, NA is the numerical aperture of the objective. The diffraction limit can be slightly pushed by techniques such as the scanning confocal optical microscope [137], where a sharply focused spot of light replaces the wide-field illumination, but it cannot be said that it was really broken by this or similar techniques.

It was 1928 when Synge discussed a scheme to overcome the diffraction limit. In a famous work [138] he proposed the key features of what is now called a Scanning Near-field Optical Microscope (SNOM) [47, 139]. SNOM gets around the diffraction limit by borrowing some concepts from electron physics; in fact, its principle is similar to the Scanning Tunneling Microscope (STM) [140]. A feedback-looped tip [141] scans the proximity of a sample; the "field" (electrons in STM, photons in SNOM) tunnels from the substrate, across the narrow gap

between tip and sample; the detected intensity is monitored during the scan and maps an image of the surface. In SNOM, the near-field tip (also called the probe) is usually fabricated by pulling [142, 143] or etching [144, 145] an optical fiber taper, and is often metallized at the end in order to suppress the coupling of diffracted light fields. The resolution of this technique is limited by the size of the tip aperture, which can reach dimensions of only 50 nm. This resolution is of course poorer than the STM atomic resolution, where no finite-size hole is needed and the tip has true atomic resolution, but is far below the diffraction limit.

The very first studies of the physical properties of SPPs using SNOM investigated the mode confinement at the interface of a thin silver film with air [50]. These studies allowed, for instance, the determination of the penetration of the SPP fields into the air above the surface. Then, the combination of near-field collection with raster scanning techniques enabled the direct visualization of propagating SPPs [49]. Near-field probing has also proved very useful for the assessment of scattering losses on structured metal surfaces [146] as well as for the determination of the dispersion properties of SPPs at curved surfaces [147]. More recently, "apertureless" SNOM techniques have proved to be intriguing and promising strategies [148, 149, 150].

In this Chapter, we describe a fulfilled project for the development of a custom SNOM head, which was integrated on a pre-existing ellipsometric system, in use at the LaNN laboratory. The above-mentioned ellipsometer was essential in different papers by our group, where it allowed far-field investigation of the properties of plasmonic structures such as digital gratings [151] or plasmonic crystals for SPR-based experiments [152, 153]. The aim of this project was to combine ellipsometry and SNOM to get simultaneous control of both far-field and near-field characterization. Such an instrument, which has never been described in literature or industry, is very promising since it allows a full optical description of plasmonic surfaces and devices.

The combined system was called EllipsSNOM. The project was carried out together with SNOM producers (A.P.E. Research, Trieste) in the framework of the PLATFORMS project, and it allows performing coupled near- and far-field measurements, as well as particular and easy-to-setup SNOM characterization. We describe the design, implementation and testing of the instrument, together with the first scientifically relevant experiments.

6.2 Design and implementation

In order to design our custom SNOM head, we had to consider two sets of requirements: those imposed by the coupling with our ellipsometer and those defined by the type of characterization we want to perform on our samples.

Let us first discuss the latter. In principle, we wanted the SNOM head to work both in *collection* and in *illumination* mode, and in both cases it should be possible to work either in *reflection* or in *transmission*. In collection mode the SNOM probe is used to measure the near-field optical signal, created by an external source in the far-field. In illumination mode, on the contrary, the sample is illuminated from the tip and the signal is collected externally in the far-field. A sketch of the possible working modes is reported in Figure 6.1; of course, we wanted the topographic signal as well.

To work as required, the instrument employs *aperture* SNOM probes. In particular, the probe is a hollow tapered optical fiber, with a diameter d<100nm (d << λ) at the end of the tip, mounted on a tuning fork for feedback and connected to a PMT detector. The fiber is metal-coated to avoid undesired reflections.

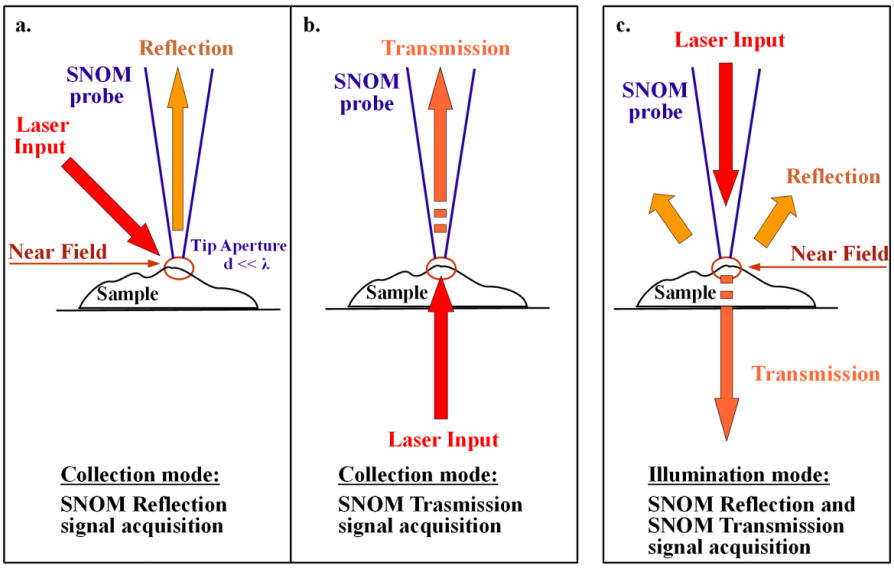

Figure 6.1 Sketch of the possible SNOM working modes: Collection mode (external illumination and collection from the tip) in (a) reflection or (b) transmission; (c) Illumination mode (illumination from the tip and collection in the far-field) with external signal acquisition, both in reflection and in transmission.

The laser source for the EllipsSNOM was designed to be interfaced with the pre-existing input unit of the ellipsometer. This, besides being necessary to perform combined ellipsometric-SNOM measurement, allows a large degree of control on the illumination conditions. Since the laser passes through the illumination optics of the ellipsometer, in fact, it is possible to set important parameters such as the polarization and the angle of incidence; moreover, we can decide whether to illuminate the sample with either focused or collimated light, by inserting or removing the focusing probes of the ellipsometer. Concerning the illumination wavelengths, the SNOM system was equipped with three laser lines, tunable and interchangeable, at 532 nm, 658

nm and 780 nm, respectively. These wavelengths cover the region of the spectrum which is mostly used for plasmonic substrates in our lab. Figure 6.2 shows some pictures of the tip in *collection mode*.

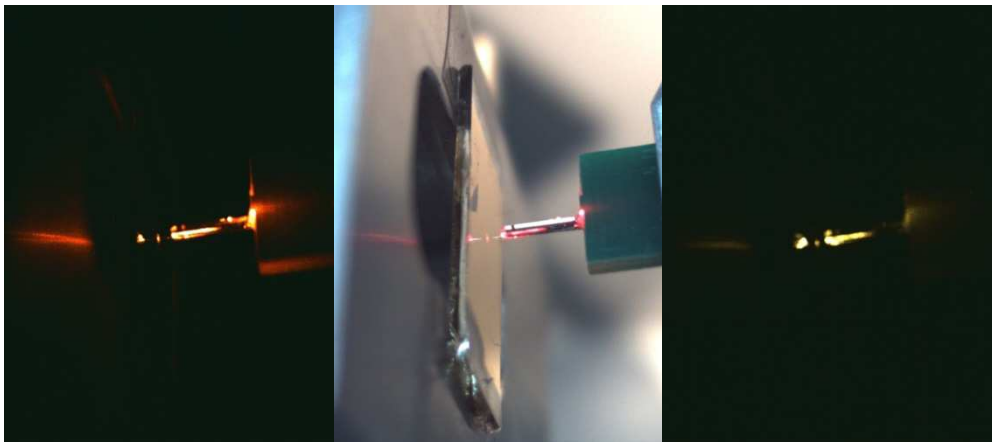

Figure 6.2 Pictures of the tip working in collection mode. (a, b) λ=658 nm, (c) λ=780 nm.

We now consider the constraints due to the fact that this SNOM is not a stand-alone machine, but it is mounted on a pre-existing instrument; this of course limits the possible designs to due hindrance or operation issues and might create stability problems.

The ellipsometer is a J.A. Woollam Co., Vertical Inc. Variable Angle Spectroscopic Ellipsometer (VASE), equipped with an arc lamp and a monochromator, ensuring a spectral range 250 nm-2500 nm. The polarization of the input beam is defined by an input unit which can be controlled via software, while a detector unit collects the signal and measures the polarization state of light after it is reflected off or transmitted through the sample. The beam diameter is 2 mm, but can be reduced to 200 μm by using the focusing probes.. A schematic view of the instrument is reported in Figure 6.3.

The SNOM head was initially designed to be interfaced to the original sample holder of the ellipsometer (3 in the figure), resting directly on the goniometer base (4) in order to minimize modifications on the system itself and maintain the balance, positions and alignments.

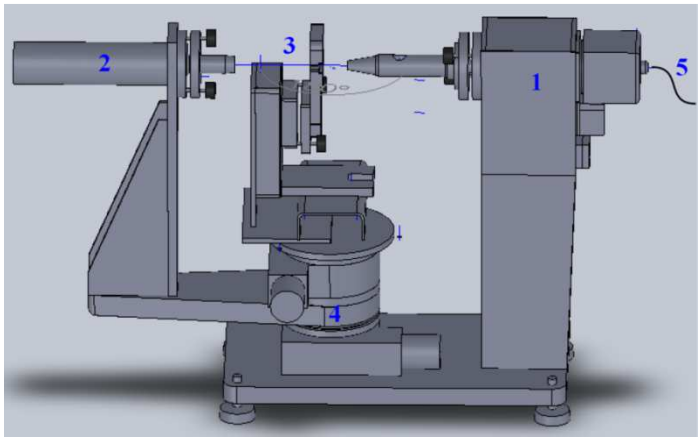

Figure 6.3 Layout of the ellipsometer: 1. Input units; 2. Detection unit; 3. Sample holder; 4. Goniometer base and central stage; 5. Fiber optic cable.

The first issues we had to deal with concerned hindrances in different measurement configurations. As a first solution, a "bridge", “C-shaped” structure was chosen (see Figure 6.4). The support frame was mounted on the central stage of the ellipsometer, between the goniometer and the sample holder. The SNOM head, lying on the upper side of the frame and thus reaching the sample holder from above, could be set in different positions, thus fulfilling the working requirements discussed above (illumination/collection, reflection/transmission). It was designed in *vertical configuration*, i.e. maintaining the vertical plane of the sample. In reflection mode, a working range [25°-80°] for the angle of incidence θ was ensured, while in transmission mode, the angular range of the incident light was not limited below the range [0-40°].

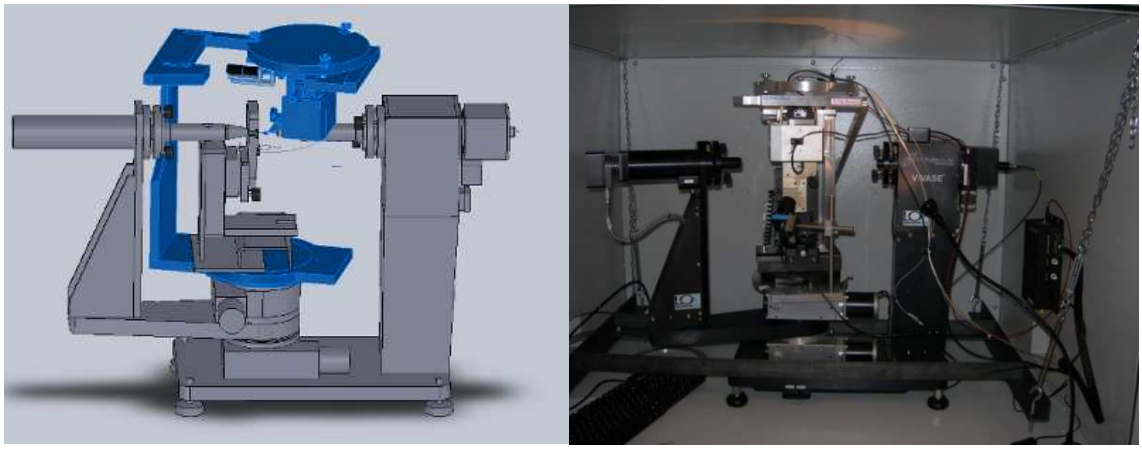

Figure 6.4 SNOM frame in the “C-shaped” structure, design and implementation.

Another critical factor was optimizing the optical path of the SNOM system, in particular the alignment of the SNOM probe with the laser spot, the position of which is fixed by the

ellipsometer. The structure and components of this part are shown in Figure 6.5. The xy-movimentation of the tip along the scan axes can be carried out by a translation system equipped with manual micrometers (range 13 mm), while the movement along the z-axis for tip approach (a horizontal movement in this setup) is guaranteed by a motorized translator, controlled via software.

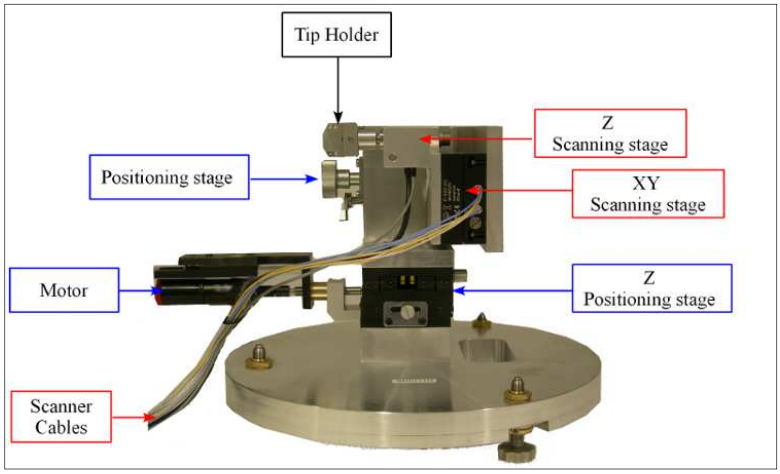

Figure 6.5 Picture and composition of the SNOM head. Highlighted are the probe holder, the scanning system with xy- and z- separated scanning stages, the xy- manual translator system for the tip and the motor for tip approach.

The SNOM system is equipped with a piezoelectric scanner of the “flexure” type, ensuring high resolution and accuracy, even on large scans. The xy-scanner is equipped with capacitive sensors, which enable working in closed loop, and provide a positioning accuracy of 0.02% and a repeatability of ± 2 nm. This kind of scanner maintains its performance even with heavy loads, regardless of the orientation (vertical or horizontal). The z-scanner is separated from the xy-scanner, thus their scan range can be set independently; the maximum scanning range is 250 µm x 250 µm x 15 µm. The technical details are listedin Table 6.1.

X-Y scan range	
	250 x 250 µm (in high voltage mode)
	25 x 25 µm (in low voltage mode)
	Closed loop linearity: 0.02%
Resolution (high voltage):	Resolution Closed loop: 0,7 nm
	Resolution Open loop: 0,04 nm

Z scan range	
Scan Range	15 µm (high voltage mode, closed loop)
	2 µm (low voltage mode)
Resolution:	0.2 nm (in high voltage mode)
	0.03 nm (in low voltage mode

Table 6.1 Scanning stage technical data.

For scanning system control, special electronic modules and specific software were developed by A.P.E. Research. Finally, the SNOM is equipped with a vision optical system to ensure probe positioning control.

6.3 Testing

After having designed and implemented the system, the main challenge was its stability. The SNOM in fact, like all SPM microscopes, is particularly sensitive to mechanical and acoustic vibrations, since the measurement probe must be carefully and continuously maintained at a critical distance of a few nanometers from the surface during scanning. The first step was to add an anti-vibration box equipped with a set of suspension springs. Then, we performed a series of stability tests.

Unfortunately, the first results of the tests were not good. Mechanical noise problems were found, which seriously affected the topographic measurements. These problems were not due to the SNOM head itself; tests on the head alone, in fact, showed that it was inherently stable. Different modifications and adjustments were proposed and tested, such as reinforcing the frame, modifying the tip holder, adding passive as well as active dampers. Although some of these changes showed improved results, they were however, on the whole, not sufficient. After all the tests, we identified the original sample holder of the ellipsometer as the main source of vibrations and we decided to re-design the SNOM with a different set-up, in particular removing the original sample holder.

In the new configuration, the SNOM head was turned upside down and positioned directly on the goniometer of the ellipsometer. Despite the need of designing a new sample holder, the new system was fully compatible with all the requirements; moreover, it is possible to move the whole SNOM head below the working plane of the ellipsometer when performing far-field

measurements, with no need of unmounting the SNOM head when simple far-field experiments are carried out. The new implemented setup is reported in Figure 6.6.

(a) 

(b) 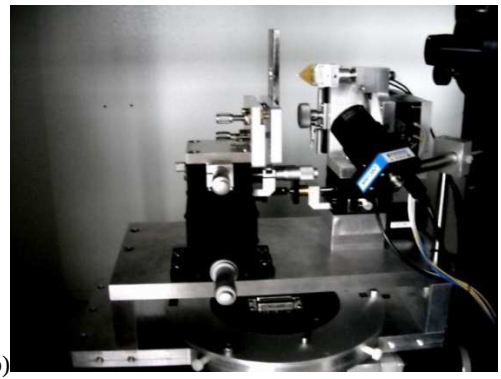

(c) 

Figure 6.6 Final EllipsSNOM setup. (a) Overall picture; (b) SNOM head and sample holder; (c) The whole system during a routine calibration scan of the ellipsometer, with the focusing probes mounted.

The new system proved to be much more stable than the first version. The noise in *z* was 3-4 nm, and the topography image was clear and reliable, as can be seen in Figure 6.7 (left).

We then tested the optical signal. As hinted above, the illumination is achieved by three interchangeable laser lines and the detection is performed by a PMT (Photo Multiplier Tube) with high sensitivity spectrum. First of all, we measured the intensity of the three lasers after the input unit of the ellipsometer, to ensure a sufficient intensity of the signal on the sample, as required from SNOM experiments. We found that the alignment detector of the ellipsometer (containing a photodiode used for the alignment of the instrument) caused a strong suppression of the signal and we thus decided to remove it during SNOM scans. Moreover, the use of the focusing probes to increase the signal was recommended, especially for the 780 nm laser which is the weakest one. After having defined the best illumination conditions, we had to optimize

the collected signal; to this end, it was necessary to eliminate the optical background by entirely obscuring the system with thick black curtains.

Figure 6.7 shows one of the first complete topography-SNOM images collected. The optical signal corresponding to the topography in (a) is shown in (b). A good contrast is achieved and the signal can be easily related to the topography, even if, of course, a proper interpretation of the signal is not straightforward and must be performed for each measurement. This issue will be addressed when discussing the "truly scientific" experiments in the next Section.

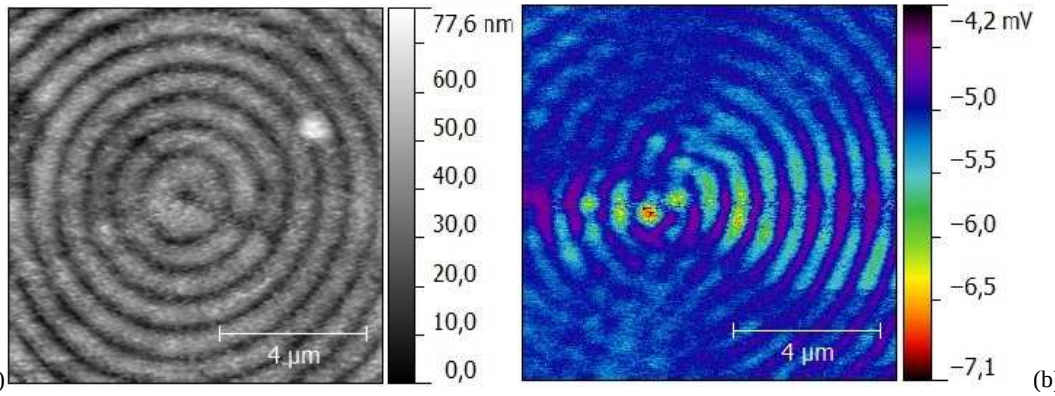

(a) (b)

Figure 6.7 Topography (left) and SNOM (right) scans obtained with the new setup. The sample was a holey bull's eye structure illuminated in the plane of incidence (horizontal polarization in the figure). As can be seen, the topography is stable and reliable, and the optical signal is well-defined. In this picture, the diameter along the polarization direction shows an enhanced signal, due to the geometry of the structure.

Finally, we tested the *ellipsometric* operation with the EllipsSNOM system, concerning in particular the alignment of the system, which is crucial in far-field experiments. Specifically, we wanted to check:

1) The alignment capabilities of the new sample holder;
2) The stability of the alignment upon suspension of the entire system;
3) The stability of the alignment upon removal of the alignment detector. This is not trivial; in fact, to remove the alignment detector it is necessary to unmount the focusing probes after their alignment and then remount them.

Figure 6.8 shows our test, performed on a gold sinusoidal grating having pitch 520 nm and amplitude 40 nm, commonly used for SPR experiments. If this grating is azimuthally rotated by a certain amount, which resulted to be about 50° from simulations, the "classical" plasmonic crystal dip is "split" into two broader dips, which appear in the reflectivity scan at two separate angles of incidence. Since the (azimuthal) angular range in which this phenomenon occurs is very narrow, this setup is very sensitive to misalignments.

The three curves plotted in Figure 6.8 correspond to three situations of increasing complexity: (a) system aligned, with the SNOM system resting on the box; (b) system suspended with springs; (c) system suspended, after removal of the alignment detector. As we can see, no significant downgrade of the signal is observed, even in the most critical condition.

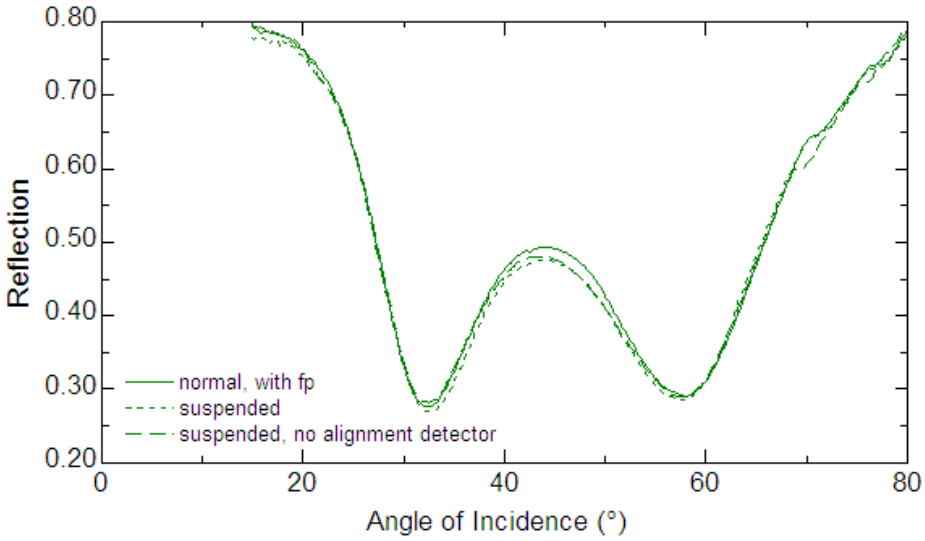

Figure 6.8 Reflectivity scan showing the two plasmonic dips expected for azimuthally-rotated experiment (φ≈50°), performed in three different conditions of increasing complexity.

6.4 Experiments

In the following, we show the first scientifically relevant experiments we performed with the EllipsSNOM. In the first one we were able to observe an SPP propagating toward the center of an Archimedean spiral illuminated along a diameter; in the second one we observed the plasmon on a waveguide, coupled by a digital grating in transmission. In the third experiment, we present the first combined far- and near-field measurements.

6.4.1 SPPs on an Archimedean spiral

We fabricated m=1 Archimedean spirals similar to the ones described in Chapter 5, using EBL followed by electrolytic growth of gold. In this case, the spirals were made of slits completely milled in the Au slab, rather than grooves, since we wanted to perform the experiment in transmission; in this configuration we actually expect a smaller coupling

efficiency of the SPP, but on the other hand we have the possibility to obtain a “clean” signal, free of backgrounds due to reflections. Moreover, we gain the possibility of both illuminating and collecting light at 0°, as required by the design. Another difference is that in these samples a large (diameter: 10 μm) flat area is present at the center, to avoid direct transmission of light and thus enabling an easy-to-interpret signal. The pitch of the spiral was 778 nm, the duty cycle was 50% and the thickness of the spiral and the flat center was 150 nm. A SEM picture of the sample is shown in Figure 6.9.

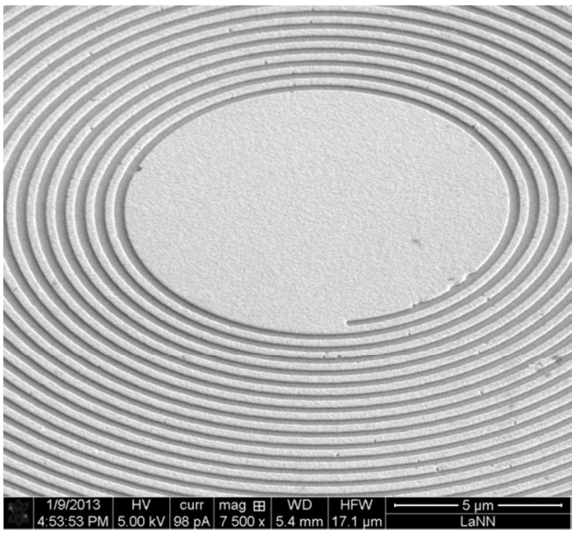

Figure 6.9 SEM picture of the Archimedean spiral structure use in this experiment.

The sample was illuminated from the backside (glass side) and the near-field was collected by the SNOM tip scanning the spiral. As a first measurement, we set a linear polarization of 45° using the input unit of the ellipsometer; with this setup, we expect two plasmons to be excited at opposite points of the spiral, where the electric field is locally TM-polarized with respect to the slits, and focus towards the center. Since the center is flat and opaque, no contribution other than the propagating plasmons is expected there.

Figure 6.10 shows SNOM scans of the spiral, at two different wavelengths (658 nm and 780 nm). Since the PVL is optimized for 780 nm, we expect no SPP to be coupled at 658 nm, while at 780 nm the above discussion applies. This is what we actually observed: the center is dark at 658 nm, while for 780 nm the SNOM signal actually shows a plasmonic excitation propagating to the center along the polarization direction. The typical “standing-wave” pattern due to the interference between the plasmon traveling onward and the one traveling backward can be seen, with intensity maxima occurring at $\lambda_{SPP}/2$. At the center, an intensity maximum is observed.

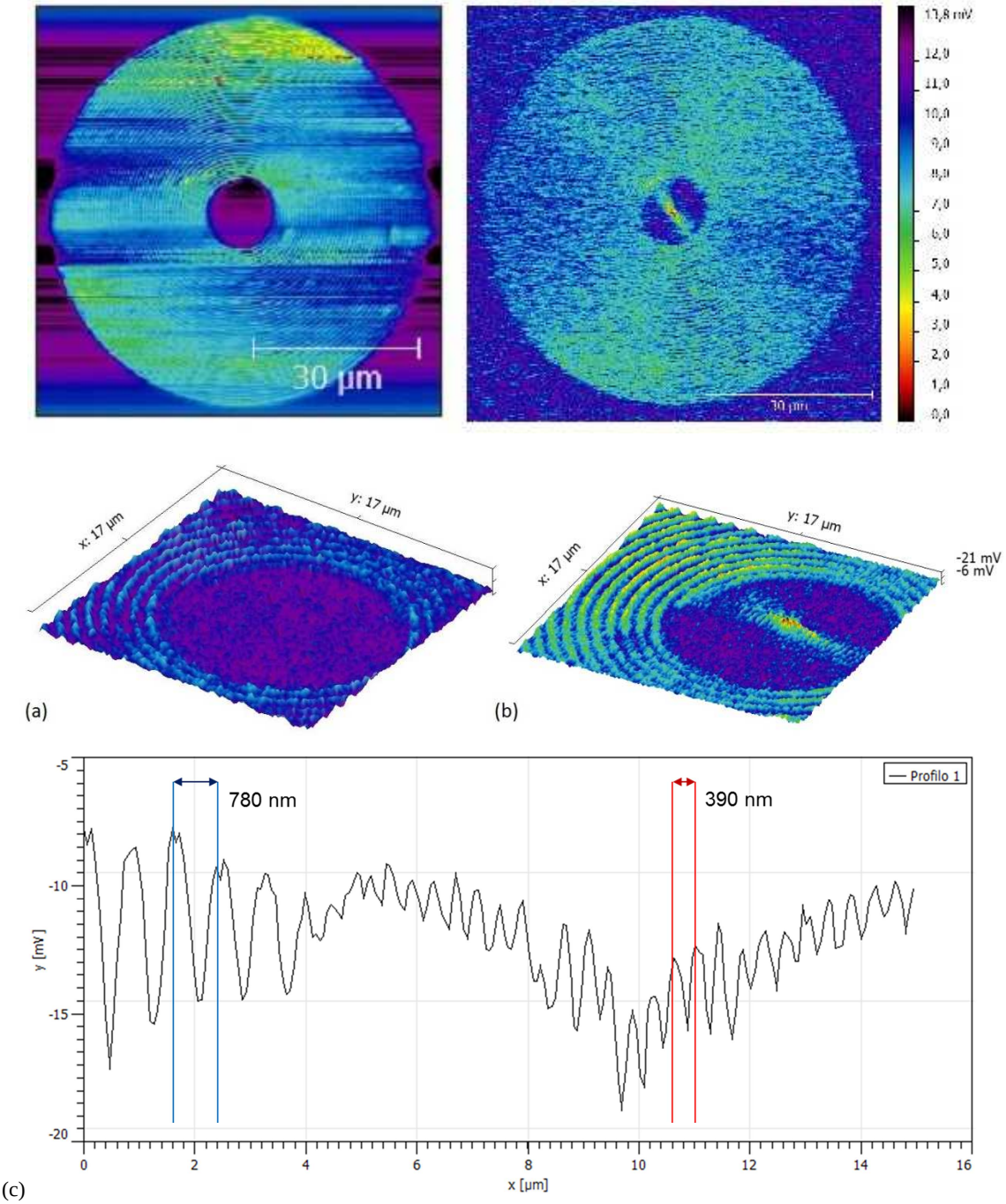

Figure 6.10 SNOM scan of a 1-PVL with a flat central region, in transmission, at (a) λ=658 nm and (b) λ=780 nm, respectively. The polarization was set at 45° and the PVL was optimized for λ=780 nm. The center is dark in the first case, where PVL is not coupled to the wavelength, while in the second case a plasmon is excited along the polarization direction. In the 3d scans of the center, the typical interference pattern between the onward- and backward-traveling plasmons is clearly seen in the central region for λ=780 nm. (c) Profile taken along the illuminated diameter in (b). In the plot a more negative signal corresponds to an higher intensity. In the left part of the plot the period of the signal is that of the grating, while in the central part on the flat region the wavelength is $\lambda_{SPP}/2$, due to interference.

As the second step, a quarter wave plate for 780 nm was conveniently inserted in the optical path of the illumination laser, after the first linear polarization performed by the ellipsometer, in order to illuminate the spiral with circularly-polarized light. Now, the PVL is expected to behave as described in Chapter 5: depending on the helicity of the incident beam (s=±1), a PV with j=2 or j=0 should appear, resulting in a different near-field pattern. For j=0, a bright spot is expected at the center, while for j=2 the light should concentrate on a ring, which, for this geometry, should have a diameter of 730 nm.

Figure 6.11 shows the results for the two values of the helicity of the incident light, corresponding PVs carrying j=0 and j=2, respectively. The variation in helicity was obtained by changing the linear polarization condition while keeping the position of the quarter wave plate fixed: this strategy was chosen since the wave plate is positioned by hand and is thus easily subject to errors, while the linear polarization status is precisely controlled via software.

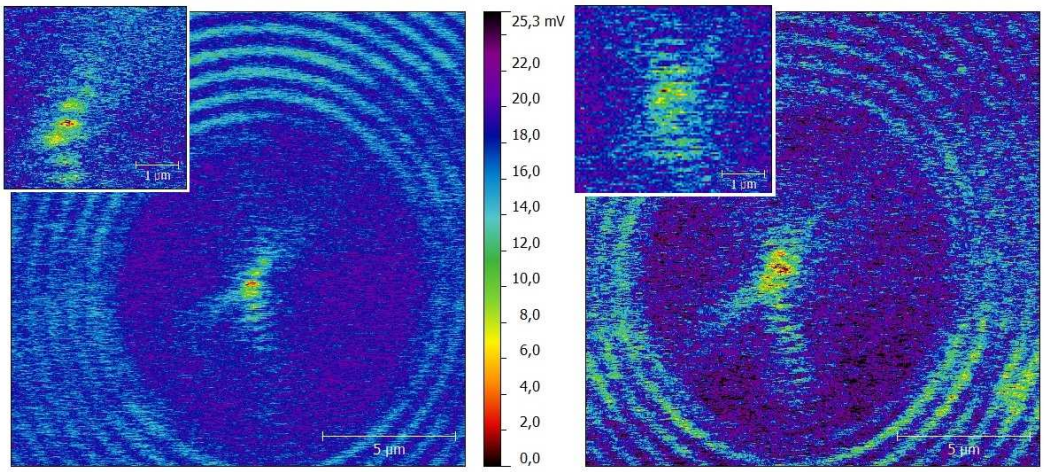

(a) (b)

Figure 6.11 SNOM scan at λ=780 nm, with the addition of a quarter wave plate. In the first case (a) the resulting PV has j=0, in the second case it has j=2. Although the pattern in the center is not perfectly clear, a difference can be seen in the two situations. For j=0, light is squeezed in a tiny spot at the very center, while for j=2 light seems to be concentrated on a larger and irregular spot around the center, which will probably turn out to be the ring with higher resolution measurements and a better control of the wave plate positioning.

The results are not easy to interpret and these must therefore be considered preliminary results. Anyway, a difference for the two situations is observed. For j=0, light is actually concentrated in a small spot at the center of the structure, while for j=2 the maximum seems to fall in a broader region around the center, even if a minimum at the center is not clearly seen. This discrepancy is probably due to errors in the initial positioning of the wave plate, which is probably also the cause of the “tails” seen in both images. Nevertheless, the diameter of the

bright spot in the second case is actually of the order of the one theoretically predicted for the ring.

We can therefore conclude that the EllipsSNOM allowed us to perform a complex and scientifically significant experiment, allowing tuning of the illumination/collection conditions and yielding promising and relevant results.

6.4.3 SPPs on a waveguide

This experiment is conceptually similar to the one described above, and somehow easier to interpret and setup; however, it allows us to highlight another capability of the instrument, i.e. its quantitative sensitivity to the intensity of the plasmonic signal.

The sample used in this experiment is shown in Figure 6.12. A flat, 60 μm-long waveguide (width: 10 μm) is coupled to a digital grating, having a pitch of 770 nm, duty cycle 10% and thickness 60 nm. Once again, this configuration is designed for illumination from the backside, to allow performing the experiment in transmission, in order to clearly distinguish the SPP signal from any stray light component. The sample was fabricated by EBL followed by Au electrolytic growth on a transparent (ITO/glass) sample. The working wavelength was 780 nm and the grating was illuminated at 0° angle of incidence with TM-polarized light.

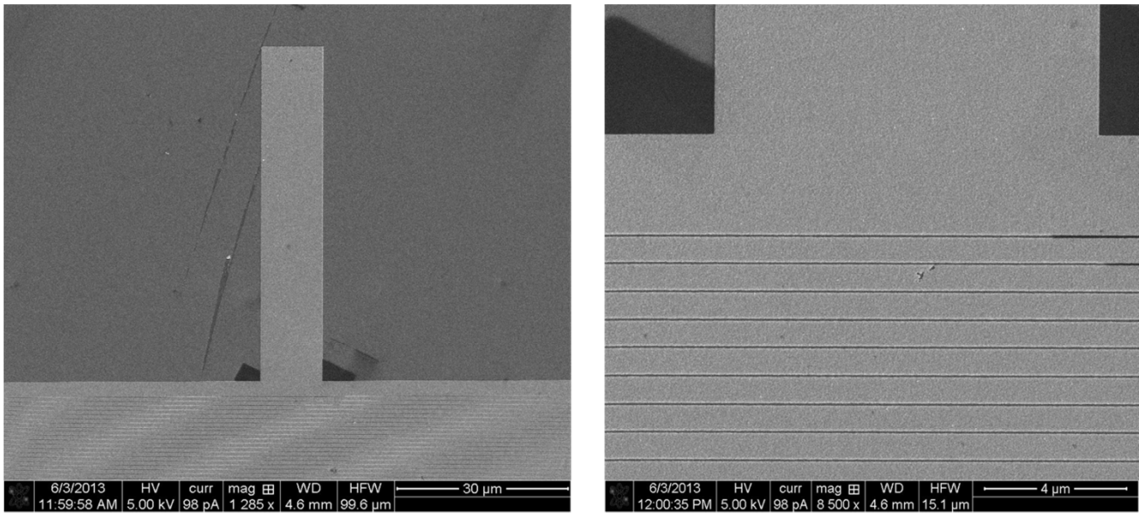

Figure 6.12 SEM pictures of the grating-coupled waveguide used in this experiment.

Figure 6.13 shows the SNOM scans performed, superimposed to the different regions on the waveguide where they were collected (the corresponding topography scans are flat). A periodic signal is observed, having a wavelength of 780 nm, as reported in Figure 6.14. This result is

retrieved in similar works in literature [154] and it is interpreted to be an SPP coupled by the grating and propagating along the waveguide.

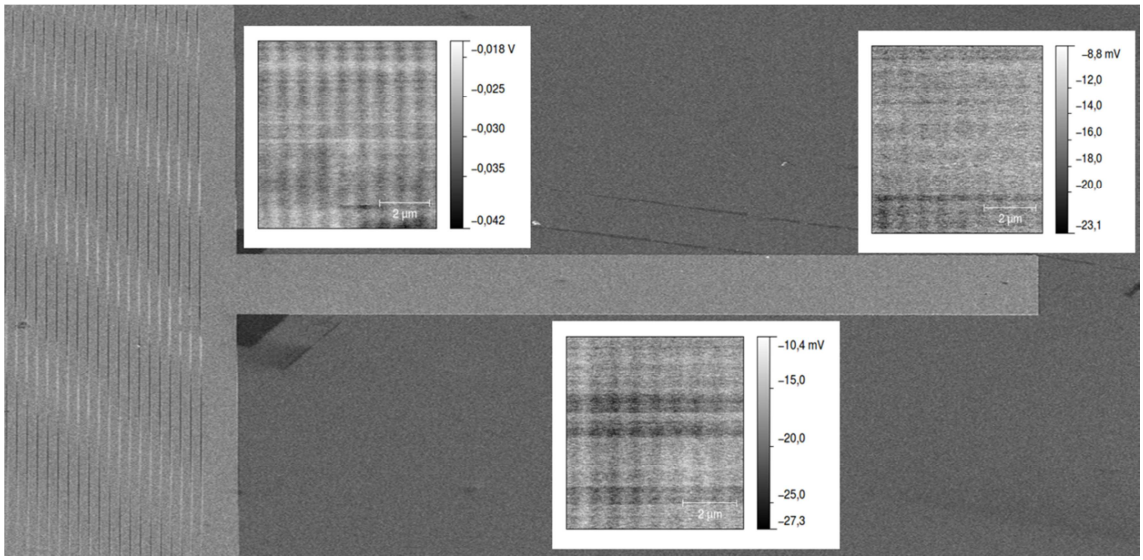

Figure 6.13 SNOM scans taken along the waveguide, superimposed to a SEM picture of the structures showing the regions where the signal was collected. A periodic signal is shown, which can attributed to an SPP propagating along the waveguide. The intensity of the signal decreases as we get farther from the grating coupler, i.e. as it propagates along the waveguide, due to Ohmic losses in the metal.

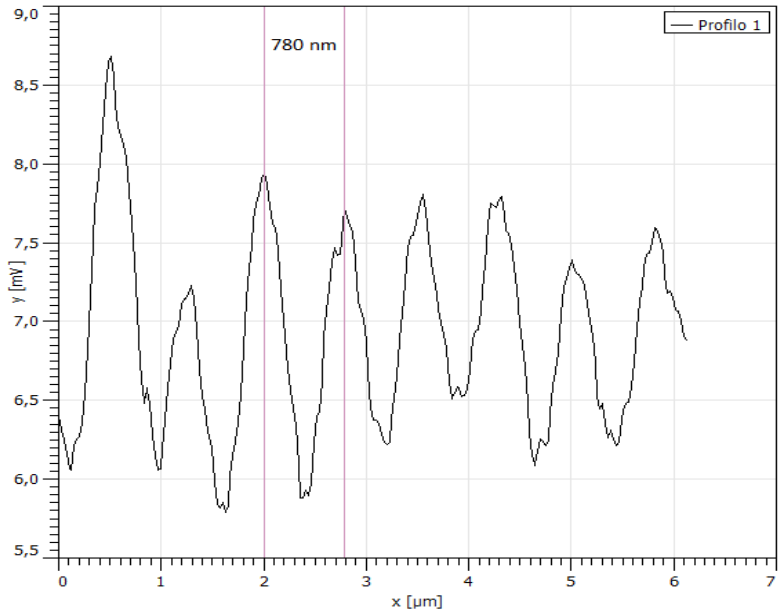

Figure 6.14 Measured profile along the first of the three scans shown in Figure 6.13. The period of the signal is 780 nm, as expected.

As can be seen in Figure 6.13, the intensity of the signal decreases along the waveguide, as we get farther from the SPP source (the grating). This is obviously due to Ohmic losses in the

metal, which cause the SPP to have a finite (some tens of microns) propagation length. This highlights the difference between such a simple system and the central region of the PVL, where Ohmic losses in the metal are overcome by the focusing effect.

6.4.3 Combined far- and near-field experiment

We finally show a combined far- and near-field experiment. The sample was a sinusoidal grating (period 500 nm, amplitude 40 nm), fabricated by interferential lithography on a silicon substrate, followed by evaporation of gold. Such samples are normally used for SPR experiments in our lab [152, 153]. Differently from the two experiments described above, this experiment was performed in reflection, illuminating the surface of the sample with the input unit of the ellipsometer and collecting the near-field with the tip.

We started from the far-field analysis, performing a reflectivity scan in angle interrogation, i.e. working at a fixed wavelength (λ=780 nm) while changing the angle of incidence. The excitation of SPPs occurs for a specific angle and TM polarization. The result is shown in Figure 6.15 (a), where we can appreciate the typical plasmonic crystal dip at $\theta \approx 38°$.

We thus fixed θ and performed SNOM measurements in TM and TE polarization: we expect a different behavior for the two conditions, in particular no SPP should be excited for TE-polarized light. The results are shown in Figure 6.15 (b). While for TM polarization the lines are "on", the signal is almost zero for TE-polarized light. The dependence of the optical signal on polarization is a fingerprint of the plasmonic nature of the observed excitation, which is therefore likely to be an SPP traveling on the grating.

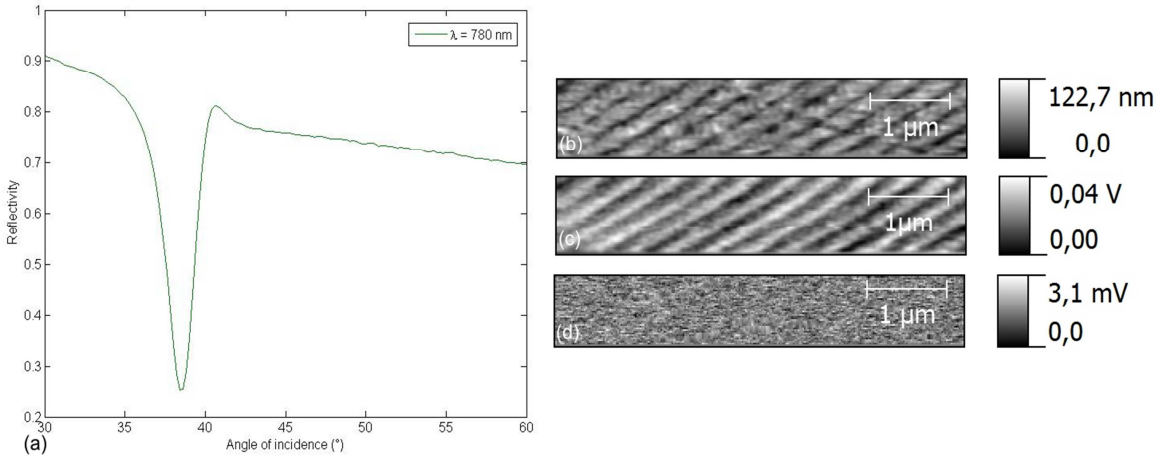

Figure 6.15 Combined far- and near-field experiment performed by EllipsSNOM. (a) Far-field characterization: SPR measurement (reflectivity scan) performed on a sinusoidal grating at λ=780 nm, in angle interrogation. The typical SPR dip appears at an angle of 38°. (b) Near-field characterization: topography and (c, d) SNOM measurements for (c) TM- and (d) TE-polarized light. A non-zero signal is observed for TM polarization only.

6.5 Conclusions

In this Chapter, we described the design and implementation of a combined SNOM-ellipsometer system, called EllipsSNOM. This new instrument allows performing coupled far- and near-field characterization of the structures under study. Such a possibility is extremely useful for plasmonic experiments, where the two characterization types give complementary and equally important information about the system.

To this aim, we collaborated with SNOM producers, APE Research from Trieste, chosen by means of a tender called by the Department of Physics and Astronomy. We studied and designed together a SNOM head to be interfaced with the ellipsometer already in use at the LaNN laboratory. Different requirements and constraints had to be taken into account.

A main problem was the stability of the system. In fact, the first layout we proposed suffered mechanical noise and we had to change the design, after having performed a large number of tests to identify the source of the noise. The new system, however, was very stable and ensured good-quality measurements, both in topography and SNOM. Moreover, it did not affect the operation (alignment, parameter range) of the ellipsometer.

We also presented the first scientifically relevant results obtained with the EllipsSNOM. First of all, it allowed us characterizing Archimedean spiral structures like the ones described in Chapter 5. Taking advantage of the many degrees of freedom and high control provided by the system, were able to set the proper illumination and collection path and we observed the expected plasmonic interference pattern at the center of the structure, with high optical resolution. We were able to measure the wavelength of the propagating plasmon and we compared the results for different wavelengths. In a similar experiment, we also observed an SPP traveling on a waveguide, appreciating the decrease in intensity as we moved away from the SPP source.

Finally, we showed a combined far- and near-field experiment. An SPR measurement was performed on a sinusoidal plasmonic crystal, observing the typical SPR dip at a certain angle of incidence and thus identifying the conditions under which an SPP was set-up; after that, we measured the near-field of the SPP, thus imaging it directly.

The EllipsSNOM system thus proved to be a valuable and versatile instrument for full characterization (topography, far field, near field) of plasmonic structures.

Final conclusions

In this thesis work we addressed the problem of concentrating light in sub-wavelength hot-spots by exploring the optical behavior of different plasmonic nanostructures. After a careful design of the structures, we employed state-of-the-art nanofabrication techniques to fabricate them with great precision. We started from relatively basic structures such as digital gratings and nanoantennae, to evolve them subsequently into smarter and more efficient structures. By these structures we were able not only to concentrate and deliver light at the nanoscale – addressing what is called nanofocusing – but also to finely control the properties of the focused light.

A fundamental task was also the characterization of such structures, which should include both far-field and near-field properties. To this end, we developed of an innovative instrument, called EllipsSNOM, which allows to performed combined near-and far-field measurements. This part of the work was carried out in tight collaboration with the company A.P.E. Research from Trieste.

We started by describing two different yet complementary plasmonic substrates, namely digital gratings and arrays of nanorods, studying their resonances thoroughly and discussing their use as SERS substrates. In particular, we designed and fabricated a 1d digital gold grating supporting a plasmonic resonance with hot-spots inside the slit, called a Cavity Mode resonance. The plasmonic properties of the structure were retrieved in its SERS response. This result was a good starting point for tailoring the properties (like field distribution) of more complex nanostructures that can be optimized and exploited for different applications.

Besides grating resonances, localized resonances were studied. We investigated in particular an array of coupled gold nanorods which was then used in a SERS experiment; it provided an experimental enhancement factor in good agreement with the calculated one. The deep understanding we gained thanks to this accurate study of LSPR-supporting nanostructures has opened up the way to the design and fabrication of smarter devices (e.g. multiple-resonance antennas) which have been optimized and shall be used for the development of innovative techniques, such as Surface Enhanced Coherent Anti-stokes Raman Scattering (SECARS), in collaboration with Politecnico di Milano.

We then moved to more complex nanostructures, addressing what can be effectively called nanofocusing of light, that is, is the *delivery* and *concentration* of light at a scale smaller than the limit imposed by diffraction. We found out that a valuable nanofocusing effect takes place in a metal coated wedge configuration, provided that the correct, phase-shifted illumination

conditions are set and the geometrical parameters are optimized. The structure is able at a time to efficiently couple impinging light to Surface Plasmon Polaritons and to guide them to the wedge ridge. The structure is characterized by an extremely simple and up-scalable fabrication process based on FIB milling anisotropic silicon wet etching and replica molding. This nanofocusing configuration was never investigated in detail before and was never experimentally studied. Although for technical reasons we were not able to fabricate the optimal structure, we could nevertheless demonstrate experimentally the nanofocusing effect, by means of both near field scanning optical microscopy and Raman measurements.

We then studied a class of nanostructured plasmonic surfaces able to efficiently couple impinging circularly polarized light to Plasmonic Vortices, i.e. SPPs carrying angular momentum (OAM). Such structures consist in multiple-turns spiral or circular grooves milled in a thick Au slab, and are termed Plasmonic Vortex Lenses (PVLs). After having discussed the mechanism by which PVLs can couple an incident wave to a PV and the properties of the focused "twisted" light, we investigated them experimentally. We showed that these structures are able not only to couple SPPs and focusing them to a sub-wavelength volume, but also to "shape" them into light with well-defined and finely controllable angular momentum properties. We also discussed a possible evolution of the device, consisting in an integrated PVL-antenna system. This device is a non-trivial integration of different optical phenomena, namely SPP traveling on a grating, nanofocusing of light, OAM properties of light, EOT and LSPR.

Finally, we described the design and implementation of a combined SNOM/ellipsometer system, called EllipsSNOM. This new instrument allows performing coupled far- and near-field characterization of the structures under study. Such a possibility is extremely useful for experiments on plasmonic substrates, where the two characterization types give complementary and equally important information about the system under study.

To this aim, we collaborated with SNOM producers, APE Research from Trieste. We studied and designed together a SNOM head to be interfaced with the ellipsometer already in use at the LaNN laboratory. Different requirement and constraints had to be taken into account, among which the most tricky was the stability of the system. However, we were able to solve these problems and we can now present a stable, reliable and versatile instrument able to ensure full characterization (topography, far field, near field) of plasmonic structures.

Appendix 1

Materials and Methods

In this Appendix I give an overview of the different instruments and techniques that were used throughout the thesis. Many of their characteristics are also discussed in the different chapters when their specific use is presented.

Particular attention will be devoted to Electron Beam Lithography. Not only this technique was extensively used during the thesis, but it was also the object of study for specific fabrication issues, such as the choice of the optimal resist polymers, the developer, and other process coordinates such as the Point Spread Function for Proximity Effect Correction.

We will then discuss two different metal deposition strategies (lift-off and electrolytic growth) which were used and/or tested during the thesis, trying to elucidate the reasons behind the choice of one or another.

Focused Ion Beam lithography will also be addressed; in this thesis it was often used in combination with EBL and it was the main fabrication tool for one of the structures presented (nanofocusing wedges).

Finally, the two main optical characterization tools (ellipsometry and SNOM) will be briefly presented.

A1.1 Electron Beam Lithography

Electron Beam Lithography (EBL) is a modern nanofabrication technique, allowing not only the direct writing of structures down to 10 nm and below, but also enabling the fabrication of high-quality masks, masters and templates to be used by other lithographic techniques. In short, it consists in exposing a charge-sensitive polymer (called a resist) with an highly focused electron beam. The charge per square centimeter deposited in the resist is called the dose. The exposure modifies the solubility of the polymer in its developer solution; the resist can thus be selectively removed in a subsequent development step if an appropriate dose is chosen.

EBL appeared in the early 1960s, evolving from the scanning electron microscope (SEM), when an electron-sensitive resist, poly-methyl-methacrylate (PMMA), was discovered. PMMA

is nowadays one of the most used positive-tone resists, even if higher-resolution resists such as ZEP have been developed.

The main advantage of EBL is its unparalleled high resolution in resist patterning, due to the short wavelength associated to electrons, which is significantly smaller than the typical minimum feature size. Therefore, EBL is not diffraction-limited, in contrast with optical lithography where the minimum resolution is comparable to the wavelength of light using for exposure (typically UV or X light). Moreover, EBL allows to precisely control the geometry and arrangement of the nanostructures, since the design is controlled by a CAD and by the machine programming language. The patterned resist can be used as a mask for the permanent transfer of the pattern image from the resist to the substrate.

The most important limitation in electron beam lithography is its low writing speed (or throughput). In fact, the serial scanning strategy of EBL cannot compete with the parallel projection of photons in optical lithography.

A1.1.1 Electron-substrate interactions

The physics of the electron-beam exposure process is dictated by the nature of electron-solid interactions, both in the resist and in the underlying substrate materials. The main parameters influencing these interactions are those of the beam (primary beam energy) and of the materials (resist and substrate materials and resist thickness).

The electrons in the beam interact with the resist-coated substrate through elastic and inelastic scattering with the resist/substrate atoms. Therefore, energy is deposited both in the resist and the substrate, and it is the energy distribution in the resist which determines the final pattern. We briefly describe the main interaction events occurring during an EBL exposure, sketched in Figure A.1:

- Forward scattering is characterized by a small scattering angle. The main impact of forward scattering on the lithography process is broadening of the incident beam. The beam broadening is reduced as the resist thickness decreases or the accelerating voltage increases. Therefore, high-energy systems like ours (100 keV) provide less beam broadening and thus higher resolution. Moreover, high-energy beams are also effective in lowering chromatic and space charge aberrations.
- Backscattering is characterized by large-angle scattering, up to nearly 180° from the primary beam direction. Therefore, it is possible for electrons reaching the substrate to return back to the resist; backscattered electrons (BSE) may also originate from the resist layer without ever reaching the substrate. A direct consequence is that BE

can deposit energy in the resist away from the primary beam, leading to pattern distortions (the so-called Proximity Effect).

- Secondary electrons ejected from the substrate. Their energy distribution has a peak at a few eV; due to their low energy, they are readily absorbed by the resist, contributing significantly to the exposure. Fortunately, their effective range in the resist is limited to a few nanometers for the same reason [155].

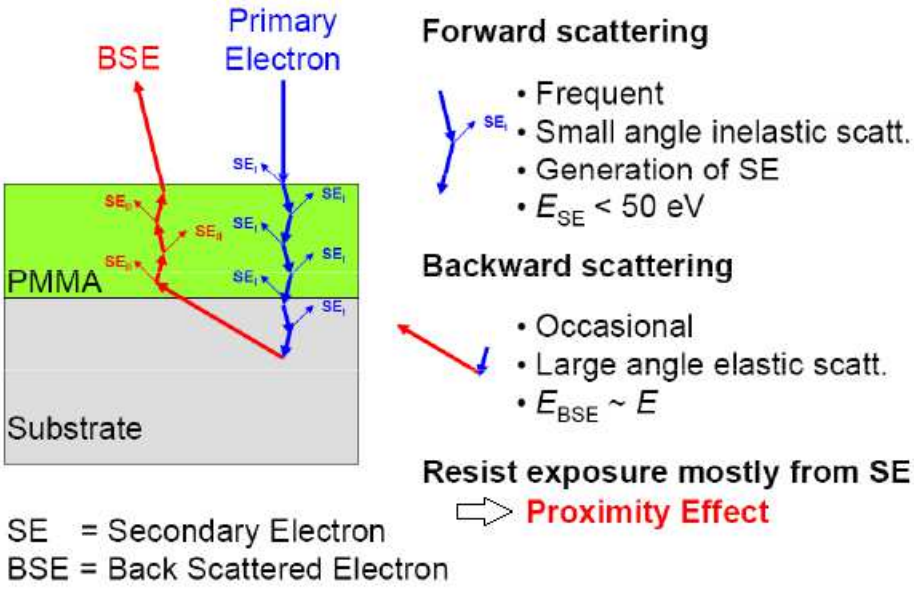

Figure A.1 Electron scattering events.

The electron collisions can be modeled by Monte Carlo simulations [156]. Although each individual scattering is random, the collective behavior of a large number of scattering events will give the correct picture of the energy deposited in the substrate. An example of such a simulation can be seen in Figure A.2. From these data, a point spread function (PSF) can be obtained, which represents the deposited energy distribution in the resist from as a function of the distance from the point of incidence. The PSF can then be implemented in the software used for Proximity Effect Correction [157].

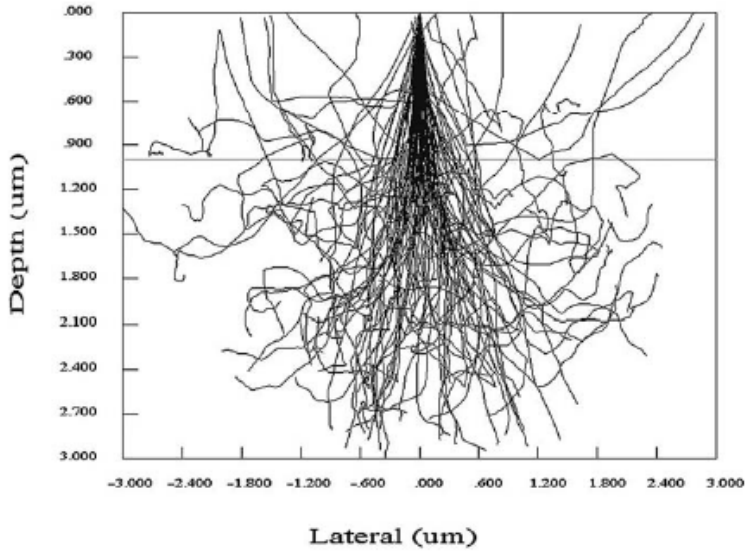

Figure A.2 Monte-Carlo simulation of a hundred electron trajectories. The energy distribution in the resist and the substrate is well-represented.

A1.1.2 Proximity Effect Correction

We have just seen that, due to electron scattering in the substrate materials, the region of resist interaction with electrons is in fact larger than the spot size of the incident beam. As hinted above, the Proximity Effect is the exposure of resist by electrons backscattered from the substrate, constituting a background where the pattern is superimposed. Since this background is not constant but rather depends on the exposed geometry, pattern distortions arise, as sketched in Figure A.3.

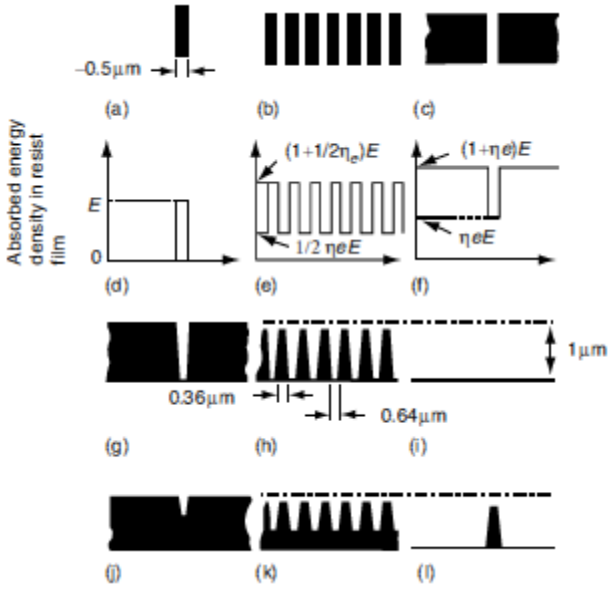

Figure A.3 The influence of the proximity effect on the exposure of (a) an isolated line, (b) equally spaced lines and spaces, and (c) an isolated space (exposed regions are denoted by shading). The absorbed energy densities are shown in (d), (e), and (f). The profiles of the resist patterns are shown in (g), (h), and (i) after development time appropriate for the isolated line. The profiles shown in (j), (k), and (l) occur after a development time that is appropriate for the isolated space.

Basically, due to Proximity Effects, the optimal dose does not depend only on the materials and thicknesses, but also on the specific pattern we are exposing. If a dose of, say, 500 μC/cm^2 is determined for equally spaced lines 500 nm wide, it will probably be wrong for a 100 μm x 100 μm square pattern, as well as for a 70 nm x 30 nm nanorod. In general, large or "dense" patterns receive a lot of background exposure and thus need a lower "nominal" dose with respect to smaller and/or isolated features, which receive no or low background charge. It is clear that, for complex geometries, the correct determination of the dose is not trivial, and different regions in the same pattern will require a different dose.

There are commercial software which allow determining the correct dose for each feature, with respect to the so-called Base Dose, considering the dimensions and position of the feature in the pattern. The Base Dose is the correct dose for a "standard" pattern of equally spaced lines at the center; it depends on the resist process, the underlying material stack composition and the accelerating voltage. Once properly calibrated, and used in conjunction with dose correction, the Base Dose becomes independent of pattern layout and underlying material stack. To determine it, a preliminary "calibration" exposure must be performed. Besides the Base Dose, the PSF for the considered sample is needed. This can be obtained from Monte-Carlo simulations, but it is often implemented experimentally using properly-designed patterns. These patterns allow to experimentally determine the α, η and β coefficients of the PSF; these parameters are basically

the width of the Gaussian distributions appearing in the PSF, which can be approximated as a multi-gaussian function. While η and β are related to the "long-range" back-scattering correction, which accounts for the different "surroundings" of different parts of the pattern, α is the so-called short-range parameter and allows to correct the shape of tiny features.

To determine the PSF coefficients and the Base Dose in this thesis, we used the method suggested by Unal et al. [158]. We exposed a properly designed pattern similar to the one proposed in that work, but correcting the limitations highlighted by the paper itself. The suggested pattern, sketched in Figure A.4, consists of a large "square grating" field, made of equally spaced lines (pattern density 50%), with different checkerboard patterns ("sensors") placed in appropriately chosen points. Each of these pattern allows to determine one of the above-mentioned parameters.

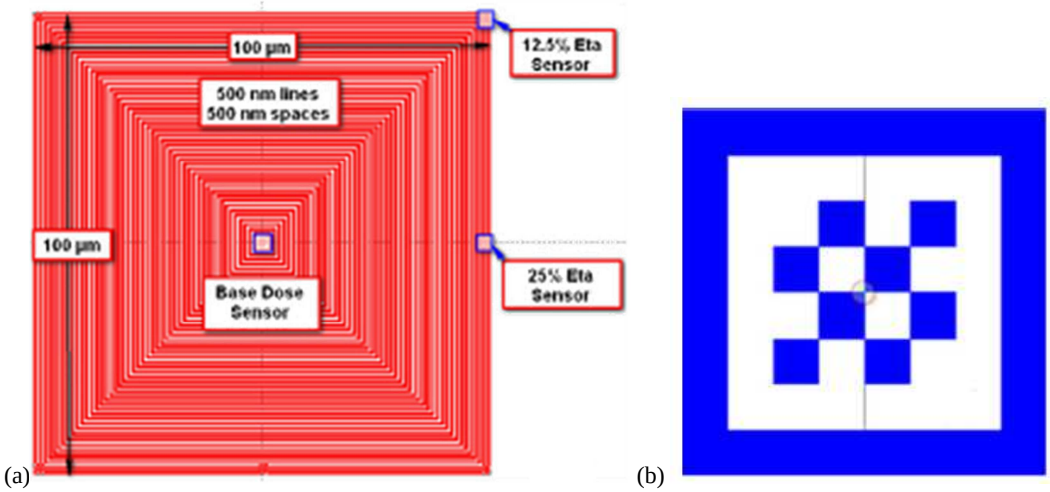

(a) (b)

Figure A.4 Layout of the pattern used for the evaluation of the coefficients of the Point Spread Function for Proximity Effect Correction (taken from [158]). (a) Complete pattern, with the position of the "sensors" highlighted. A matrix of such patterns with different doses was exposed. (b) Dose "checkerboard" sensor. The optimal dose is determined by looking at the corners of the checkerboard: when they are exactly touching (no residual resist and non-merged squares), then the dose is correct.

The ''Base Dose Sensor'' is positioned in the center of the large field and the Base Dose is simply the optimal exposure dose for this sensor. The optimal dose of course occurs when the squares in the checkerboard are exactly touching at the corners, while the pattern will be respectively under-dosed if a residual resist gap is observed between the squares, and over-dosed if the squares are merged together. The sensors at the edge and/or corner of the large field are used for η calibration. The relationship between dose and layout density is [159].

$$D = \frac{1+\eta}{1+2\cdot\delta\cdot\eta}$$

Where D is the best dose and δ is the pattern density. We notice that this equation also applies for the central sensor, which has a pattern density of 50% (0.5 in the formula). At the edge (corner) of the same pattern, the effective density is 25% (12.5%). By evaluating the best dose for this sensor and inverting the formula, we can calculate η. For the determination of β instead, a checkerboard pattern was placed in the center of an array of circles with varying radii.

We therefore exposed a matrix of 36 doses of the above-mentioned pattern, using the same process conditions that shall be used in the process of interest. Here I report an example of such a calibration. The first line in Figure A.5 shows an example of under-dosed, right-dosed and over-dosed Base Dose sensors, respectively, while the second line shows the same for the eta sensor.

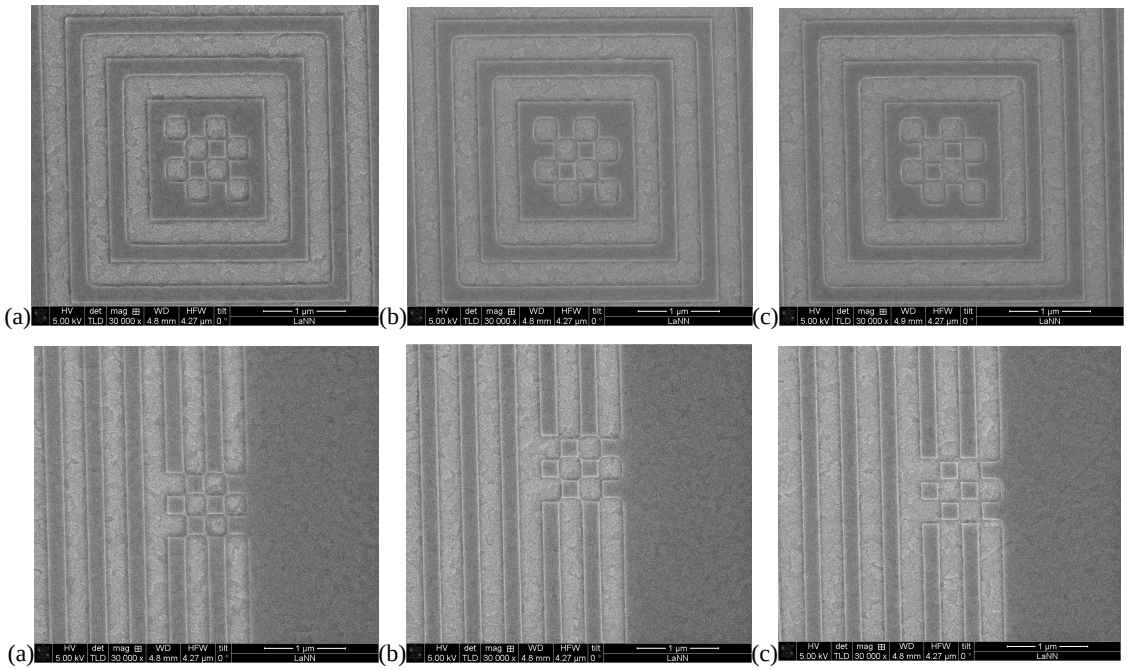

Figure A.5 SEM pictures of the exposed checkerboard pattern "sensors" for Base Dose and η determination. (a) Underdose (b) Best dose (c) Overdose

Although Proximity Effect Correction software usually allow to compensate well enough for proximity effects, in some cases the correction can be done more efficiently by resizing the pattern geometry (biasing). This is often used for very tiny structures (tens of nm) where increasing the resolution of software corrections may create undesired pattern distortions.

A1.1.3 Electron Beam Resists

Electron-beam resists are most commonly liquid solutions of organic polymers. The liquid is applied to the substrate by spin coating, to form a film of uniform thickness and is then soft-baked to yield a durable polymer film on the substrate. The resist may also be applied to the substrate in multiple layers, for instance in combination with other materials which are not sensitive to EB exposure. As hinted above, the energy of charged particles deposited in an EB resist modifies the polymer chain structure and thus the solubility of the resist in specific developers, usually organic solvents or aqueous-based developers.

There are two main EB resist types:

- For *positive* resists, exposure has the effect of breaking the polymeric chains. The exposed regions are thus made more soluble and are selectively removed by the developer. After metal deposition has been performed, we therefore obtain the positive image of the exposed pattern.
- For *negative* resists, exposure has the effect of helping the cross-linking of the polymeric chains. The exposed regions are thus made less soluble and the unpatterned area is removed by the developer. After metal deposition, we obtain the negative image of the exposed pattern.

There two main parameters describing the performance of a resist are sensitivity and contrast, which are directly linked to the resolution capability of the resist.

The sensitivity is related to the dose needed to completely clear a region of exposed resist. It is experimentally calculated from the contrast curve of a resist. A contrast curve is obtained by exposing a series of large squares with different doses and measuring the remaining resist thickness against the exposure dose. The dose needed to clear the resist is normally quoted as the sensitivity of the resist. The smaller this threshold dose, the higher the resist sensitivity.

The contrast is defined by the slope of a development curve and is expressed in Figure A.6. D_p is the clearing dose defined above and D_0 is the exposure dose at which the resist starts to be removed by the developer. The steeper the slope, the higher the resist contrast. An high contrast is always desirable because it leads to steep resist profiles after development.

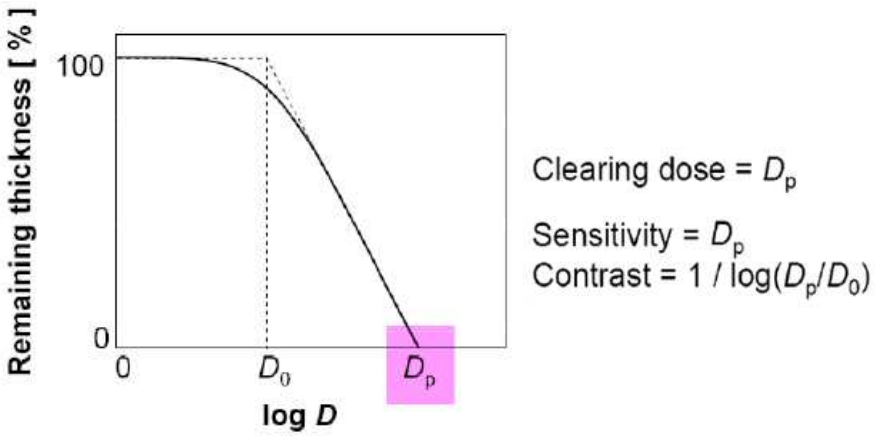

Figure A.6 Clearing dose, sensitivity and contrast definition.

PMMA-TYPE RESISTS

PMMA is the first and still the most common positive resist. It has extremely high resolution (below 10 nm), excellent shelf life, and does not suffer from swelling or post-exposure latency effects. Its biggest drawbacks are its poor sensitivity, poor dry etch resistance, and poor thermal stability. It is available in molecular weights from 50K to 950K, with slightly decreasing sensitivity and higher resolution capability with increasing molecular weight. PMMA is also sensitive to exposure by deep ultraviolet light and x-rays, permitting hybrid exposure strategies.

In this thesis, we mostly used the All Resist AR-P 671.05 and AR-P 671.02 resists, consisting of PMMA polymer in chlorobenzene. At 400 rpm they yield a resist thickness of 490 nm and 90 nm, respectively.

NEGATIVE RESISTS

We employed the negative e-beam resists of the All Resist series AR-N 7520. They show a good sensitivity, very high resolution (< 30 nm), high contrast and an excellent process stability, due to the fact that the crosslinking is not based on the principle of chemical amplification. These resists contain Novolak resins, naphthochinondiazides and crosslinking compounds in the solvent propylene glycol-methyl-ether-acetate. The resists can be developed in the AR 300-47 developer diluted with deionized water (4:1). Pre- and post-baking steps at 85° are recommended for better resist stability. Typical thicknesses we used with these resists are 100-400 nm.

A1.1.4 Developers

In EBL, the development of exposed resist often involves the use of binary solvent mixtures, which typically consist of a strong solvent and a moderating non-solvent. The mixture must act as a minimal solvent for the unexposed resist, in order to minimize swelling, while being a good solvent for the exposed resist, so that the soluble regions are completely dissolved and washed away.

A standard developer for PMMA is a mixture of Methil-Isobutyl-Ketone (MIBK) and isopropanol (IPA), with an optimal working temperature of 25 °C, a MIBK:IPA ratio of 1:3 and a development time of 30s [160]. This developer was used in the first structures shown in this thesis. However, in a recent work, Yasin et al. [161] found that a high improvement in sensitivity and contrast can be achieved using isopropanol (IPA)/H_2O mixtures. Among the different compositions, a ratio of 3:7 DI H_2O:IPA was selected as the optimum one, due to its combination of high sensitivity and good contrast.

This developer is more effective in removing exposed PMMA while leaving the unexposed regions unaffected. In particular, a drawback of MIBK:IPA ratio of 1:3 that we found was the large surface roughness observed in large-area partially developed resist features. As discussed in [162], this effect can be attributed to a two-dimensional phase separation effect, which is characteristic of development in weak solvents and long development times and results in a division of the mixture into polymer-rich and polymer-poor phases. The delay in dissolution of the polymer-rich phase results in some regions being left behind during development process. These regions are indistinguishable from the unexposed resist and appear as roughness. In our work [122] we found that the roughness reduces by an order of magnitude with the use of DI H_2O:IPA developer compared to MIBK:IPA development. For this reason, the 3:7 H_2O/IPA developer was used in the following of the thesis.

A1.1.5 The JEOL JBX-6300FS

The LaNN laboratory is equipped with a JEOL JBX-6300FS EBL machine, provided with a thermal field emission filament with a ZrO/W emitter. The system is pictured in Figure A.7 together with a scheme of the optical column. An accelerating voltage up to 100 keV is available, ensuring extremely high resolution (minimum line 6 nm). There are mainly two working modes:

- EOS6[4]: high resolution[5] (beam diameter as low as 2 nm), low throughput (field size 62.5 μm, typical current: 100 pA)
- EOS3: high throughput (field size 500 μm, typical current: 2 nA), lower resolution (beam diameter 6 nm)

The machine has a 4-stage electron beam focusing system with a 2-stage objective lens. The scanning speed is up to 12MHz and the stage positioning resolution is λ/1024, where λ is the wavelength of the laser used for interferometric positioning.

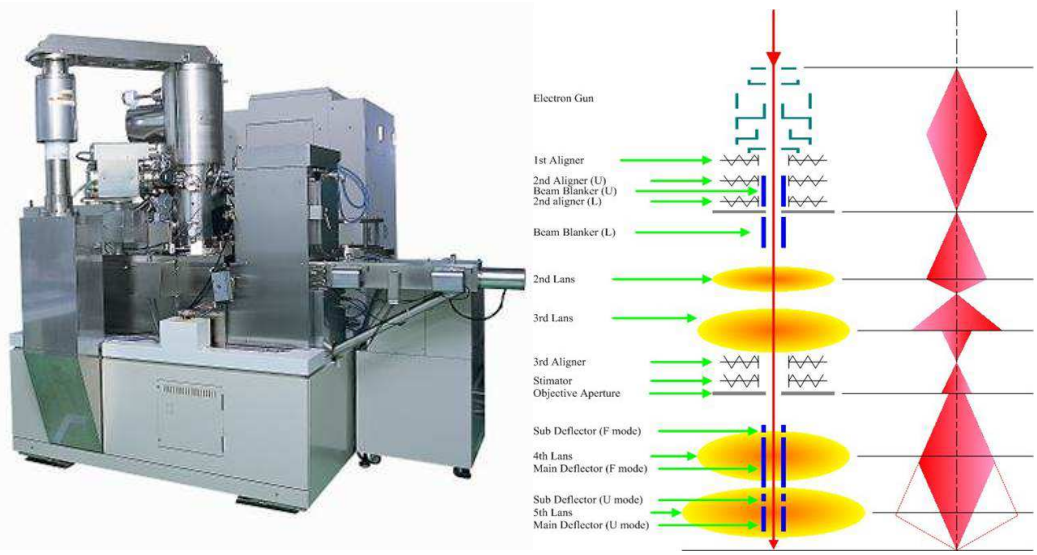

Figure A.7 Left: photo of the JEOL JBX6300-FS system in use at LaNN, Right: scheme of the EOS (Electron Optics System) of the machine. It is possible to switch from the 4th to the 5th lens sketched here to change from high-throughput (EOS3) to high-resolution (EOS6) mode.

A1.2 Metal deposition

In all the EBL processes described in this thesis, the exposed substrates were all intended for direct writing rather than for using them as masks or masters. Therefore, the deposition of the plasmon-supporting metal layer was performed directly on the exposed substrate. Two main methods were used: evaporation/lift-off and electrolytic growth. The choice of the technique

[4] EOS=Electron Optics System

[5] The resolution here is given in terms of the minimum beam diameter, which is also the width of the minimum lithographable line. However, it must be taken into account that this minimum line value holds for an isolated line in a high-resolution positive resist such as ZEP. For more complex patterns, Proximity Effect appears, reducing the minimum achievable resolution in a pattern-depending fashion. The role of a lower-resolution resist must also be considered.

depends on different parameters and will be discussed for each single case. Here we briefly described the two techniques.

A1.2.1 Lift-off

The lift-off process is shown schematically in Figure A.8. First, the desired material is deposited on the patterned substrate, usually by evaporation. After that, the resist is removed, so that the excess metal on top of the resist is washed away, or *lifted-off*, leaving only the deposited material on the substrate in the patterned openings. The quality of the metal obtained with this method is usually very good (usually better than that obtained with electrolytic growth) and an excellent control on the deposited thickness is usually achieved. However, two aspects must be taken into account:

- An adhesion layer is often needed to improve the adhesion of the evaporated metal to the substrate; usually Cr or Ti is used. Unfortunately, these layers are known to drastically affect the plasmonic resonances; therefore, care must be taken when choosing this method and the effect of the adhesion layer must be considered.
- Due to the non-selective deposition of the metal on the substrates, lift-off often requires an undercut resist profile to prevent deposition on the sidewalls, which can lead to ragged edges, tearing of material from the substrate, or total failure of lift-off due to complete encapsulation of the resist. This can be achieved for instance by exploiting a bilayer strategy. In this technique, a polymer which is not soluble in the developer used for the resist is deposited on the substrate before the resist itself; an example of such a polymer is PMGI (polymethylglurarimide). PMGI is not charge-sensitive and thus is will not be affected by exposure. After the exposure, the two polymers are developed separately; the PMGI is developed in order to have a slightly “reentrant” profile with respect to the resist (“undercut”). This prevents the subsequently evaporated gold to deposit on the sidewalls near the surface and the liftoff is therefore easier.

A1.2.2 Electrolytic growth

Electrolytic growth requires a conductive substrate and a resist thickness sufficient to prevent overgrowing on top of the resist. The conductivity needed to allow a good electrolytic growth depends on the characteristics of the electrolytic solution.

The aqueous electrolytes used for metal coatings are solutions of metal salts, which dissociate under certain conditions to form electrically charged anions and cations. Metal cations, MeZ^{+} are delivered to the substrate, and are deposited onto its conductive regions, i.e. the exposed regions only (unexposed for negative resists). Metal deposition is brought about by current flow from an external power source.

Different plating baths are possible, usually classified in terms of their operating pH. In addition to metal salts, electrolytic solutions usually contain various other species added to increase electrolyte conductivity, inorganic and organic salts, acids, alkalis. In metal finishing, anionic or non-ionic surfactants are often used.

Under equilibrium conditions, no net reaction takes place and the process is governed by a dynamic equilibrium. However, if an external bias is applied (a voltage), the equilibrium will be broken and electrodeposition takes place.

Our set-up is very similar to the one pictured in Figure A.8. Besides the two main electrodes (anode and cathode, the latter being the sample itself), another electrode between them is present, having an active area much larger than the nanostructures; its purpose is to attract the major part of the ions so that the growth becomes slower and more controllable.

For the growth processes at LaNN we used a TECHNI-GOLD 25 ES electrolytic solution. It is a neutral non-cyanide gold plating formulation having 8,2 g/l Au density. The working temperature was 30° and the electrolytic bath was controlled in voltage (-0.75 V).

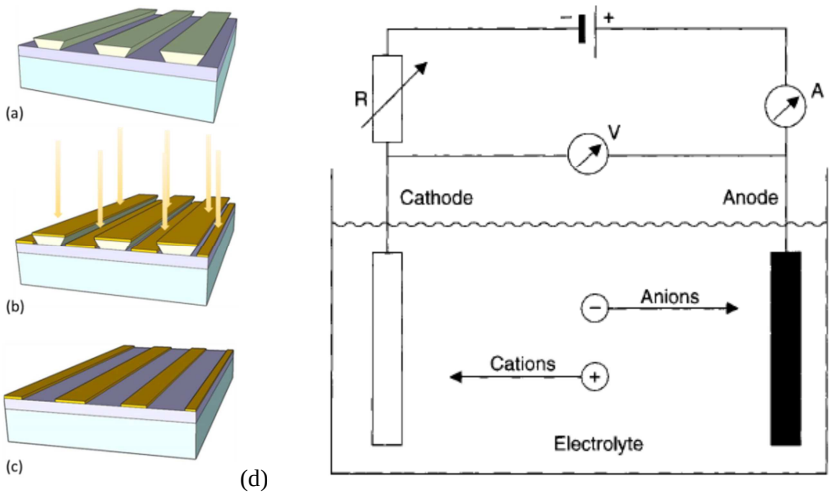

Figure A.8 Scheme of the (a,b,c) lift-off and (d) electroplating processes. Lift-off: (a) the exposed substrate is developed. An “undercut profile” is desirable. (b) Au is deposited on the surface using evaporation. The thickness is finely controlled by a balance. (c) The resist is removed (acetone for PMMA, specific remover for negative resists) and Au is left only in the exposed areas. (d) Sketch of the electrolytic growth working principle and setup.

A1.3 Focused Ion Beam

The Focused Ion Beam (FIB) is a widely used fabrication technique for site-specific analysis, deposition and ablation of materials. From the operation point of view, the FIB is similar to a SEM. However, while the SEM uses a focused beam of electrons to image a sample in the chamber, a FIB uses a focused beam of positive ions, typically Ga^+, to mill the surface of the sample. Gallium is chosen since realizing a Ga-liquid metal ion source (LMIS) is quite an easy task. The gallium source is placed in contact with a tungsten needle; the heated gallium wets the tungsten and flows to the tip of the needle. The huge electric field at this small tip (greater than 1×10^8 V/cm) causes ionization and field emission of the Ga^+ ions, which are then accelerated to an energy of 5-50 keV, and focused on the sample by electrostatic lenses.

Unlike the electron microscope, the FIB is destructive to the sample. As the highly energetic Ga^+ ions hit the sample, the superficial atoms are removed and micro-machining of the sample is therefore possible.

The FIB can also be used to deposit material by means of a sedimentation induced by an ion beam. The LaNN laboratory is equipped with an FIB/SEM dual beam Nova 600 NanoLab instrument. It combines a Scanning Electron Microscope (SEM) field effect at very high resolution and a precise FIB system.

Listed below are the technical details of the ion optics:

- Sidewinder ™ ionic column with Ga^+ liquid ion source
- Resolution: 7 nm, maximum etchable linewidth: 15 nm
- Accelerating voltage: 5-30 kV
- Probe current: 1 pA - 20 nA

A1.4 Optical Characterization

A1.4.1 Ellipsometry

Ellipsometry is a versatile and powerful technique for characterization of the optical properties of a substrate through the reflection of a monochromatic light beam impinging on the sample. By analyzing the polarization state of the reflected beam (specifically the ratio between the p- and s-polarized components), information about the thickness and refractive index of each of the layers constituting the substrate can be obtained. Moreover, SPR-like measurements can

be done by measuring the reflectivity or transmittivity of a sample in angle of wavelength interrogation.

The measurements presented in this thesis were performed on a J.A. Woollam Co., Vertical Inc. Variable Angle Spectroscopic Ellipsometer (VASE). The ellipsometer is equipped with an arc lamp and a monochromator, resulting in a total spectral range 250 nm-2500 nm. The polarization of the input beam is defined by an input unit which can be controlled via software, while a detector unit measures the polarization state of light after it is reflected off or transmitted through the sample. The beam diameter is 2 mm, but can be reduced to 200 μm by using focusing probes. The ellipsometer allows to vary the angle of incidence in the range 15°-90° (accuracy: 0.01°) and it moves in the θ-2θ configuration: when the angle of incidence (i.e. the angle of rotation of the sample with respect to the beam) is changed, the detector arm will rotate twice the angle of rotation of the sample stage.

A1.4.2 SNOM

An entire Chapter will be dedicated to the design and development of a SNOM head; therefore, here we will not enter into details of Scanning Near-field Optical Microscopy, which consists in coupling a tapered probe with a sub-wavelength aperture to the near-field of the sample under study, thus allowing optical imaging beyond the diffraction limit. However, it is worth citing this technique one more time, since it is the only present technique which allows to directly visualize plasmons with the required resolution. This great power is accompanied by signals of highly non-trivial interpretation, due to the complex interactions between the SNOM tip and the sample.

According to Abbe's theory, the resolving capability of conventional optical microscopy is ultimately limited by diffraction. As hinted above, SNOM breaks this limit by exploiting the properties of the non-propagating fields that exist only near the surface of the object. To this end, the probe is placed very close to the surface, typically a few nanometers, and is kept there by accurate feedback techniques. With this technique, the resolution of the image is limited by the size of the detector aperture rather than by the wavelength of the illuminating light.

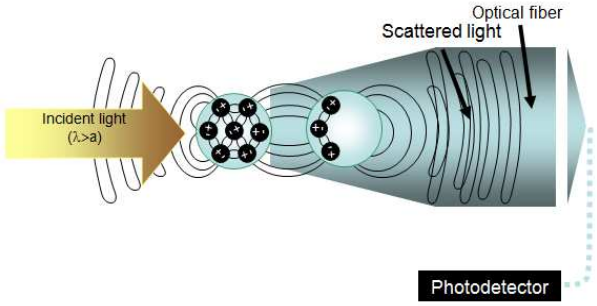

Figure A.9 Scheme of the SNOM detection principle.

Different kinds of SNOM probes were used during this thesis:

- Tapered, metal-coated optical fibers (used in the EllipsSNOM instrument described in Chapter 6);
- Cantilever probes, with tips having the shape of a hollow square pyramid (used in the Witec instrument used for the characterization of many of the described plasmonic substrates).

The two probes also require a different feedback strategy. For cantilever probes, the principle is just the same used in Atomic Force Microscopy (AFM), and the force acting on the cantilever is monitored by using a beam-deflection setup and a four-quadrant photodiode. For optical fiber probes, a tuning fork is often used to monitor the shear force acting on the probe. The probe is raster-scanned across the sample and the near-field optical signal is collected together with the topography. Figure A.10 shows some pictures of typical SNOM probes.

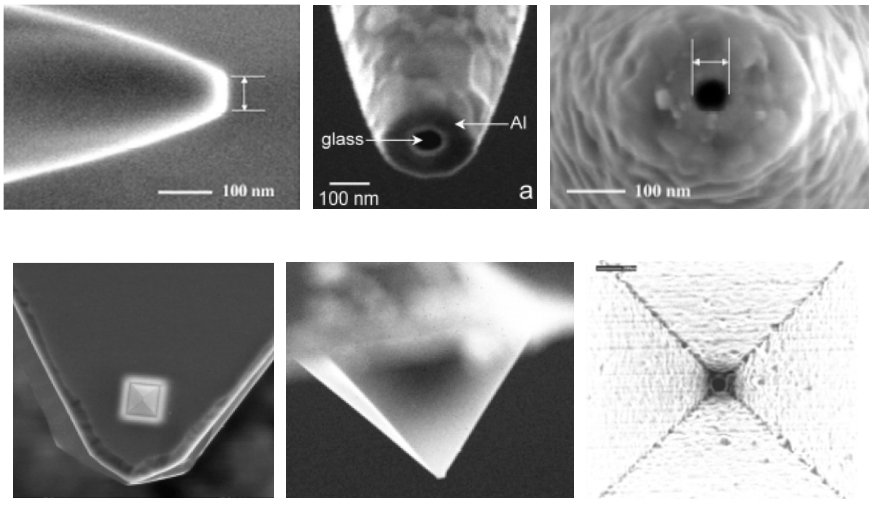

Figure A.10 Pictures of cantilever probes. First line: tapered optical fiber probes such as the ones used in the EllipsSNOM described in Chapter 6; Second line: cantilever-type probes. The tip is a hollow square pyramid. The diameter of the sub-wavelength hole is typically around 60 nm.

Activities and publications

Publications:

1. *Enhanced sensitivity azimuthally controlled grating-coupled surface plasmon resonance applied to the calibration of thiol-poly(ethylene oxide) grafting*, Sensors and Actuators B **181**, 559-566 (2013)
2. *Plasmonic nanofocusing by means of metal coated dielectric nanowedges*. In: Proceedings of SPIE - The International Society for Optical Engineering **8457**, art. no. 84572L (2012)
3. *Wedge nanostructures for plasmonic nanofocusing*, Opt. Expr. **20**, 16224-16233 (2012)
4. *Design, fabrication and characterization of phase masks for astronomical applications*, Microelectron. Eng. **88**, 2675-2678 (2011)
5. *Sinusoidal plasmonic crystals for bio-detection sensors*, Microelectron. Eng. **88**, 1898-1901 (2011)
6. *Temperature insensitive conductance detection with surface-functionalized silicon nanowire sensors*, Microelectron. Eng. **88**, 1753-1756 (2011)
7. *Design, fabrication and characterization of plasmonic gratings for SERS*, Microelectron. Eng. **88**, 2717-2720 (2011).
8. *Nanoscale silicon nanowires surface functionalization and characterization for sensing applications*. In: Proceedings of ESSDERC/ESSCIRC. Seville (Spain), 2010
9. *Nanoscale-selective silicon nanowires surface functionalization for sensing applications*. In: Proceedings of MRS Spring Meeting Symposium K. San Francisco, CA USA, April 5-10, 2010

Submitted to Conference Journals:

10. *Study of the Coupling Properties of Plasmonic Vortex Lenses with Nanoantenna Resonators*, Metamaterials 2013 (Bordeaux);
11. *Integration of dipole nanoantennae in a holey Plasmonic Vortex Lens*, oral presentation at MNE 2013 (London).

Participation to the research projects:

- Progetto di Eccellenza 2008-2009 della fondazione CARIPARO “Surface PLasmonics for Enhanced Nano Detectors and Innovative Devices (SPLENDID)”;

- Progetto Strategico di Ateneo 2008: "PLAsmonic nano-Textured materials and architectures FOR enhanced Molecular Sensing (PLATFORMS)";
- Progetto PRIN: "Design and fabrication of nano-based plasmon optics designed for interaction with structured light with orbital angular momentum".

Participation to schools and conferences:

- *International School of Quantum Electronics – 47th course: advances on Nanophotonics* – Erice (TP), 11-18 July 2010;
- *MNE 2010, 36th International Conference on Micro & Nano Engineering*- Genova, 19-22 September 2010;
- *SPIE Optics and Photonics 2012* - San Diego, California (USA), 12-16 August 2012;
- *MNE 2013, 39th International Conference on Micro & Nano Engineering*- Genova, 16-19 September 2013;

Acknowledgements

So that's the end of this journey, and it's time to say thank you to each and every one who helped me getting here. First of all, I would like to express all my gratitude to all my colleagues at LaNN in Padova and IOM/TASC in Trieste, for being not only valuable collaborators, but also good friends. In particular, I really thank Pierfrancesco Zilio for his constant support in simulations and fruitful discussion on theoretical aspects. He was always very helpful and kind to me. A great thank you must also be said to Michele Massari, who welcomed me in my first PhD days and introduced me to EBL… and he is still a reference for nanofabrication issues, and a nice person to chat with. A special thanks also to Denis Garoli, who showed equal – and great – ability at FIB lithography and at cooking lunches at LaNN. I also would like to thank Valentina Giorgis, for her patient and extremely helpful support with evaporations and electrolytic growths in Trieste, and Gabriele Zacco, the "fake Irishman" (from Sicily) who was always so nice and a smile-bringer. Thank you also to Tommaso Ongarello, with whom I shared our first PhD year at NanoFab and who was an excellent guitarist for my *bossa nova* "in-house" exhibitions. And I would like to mention and thank all the other LaNN collegues: Enrico Gazzola, Gioia della Giustina, Francesco Ricci, Gianluca Ruffato, Davide Sammito, Alessandro Surpi, Giuseppe Parisi and Elettra Mari. I do not want to forget the Master students who worked or are working at LaNN, with a special mention to the ones I am trying to follow in these months: Giovanni Sartorello, who is excellently sharing long and challenging – but fruitful – "EllipsSNOM days", and Swati Jha, who brought about some international taste to LaNN. A special thanks, then, to our technician Simone Brusa, who was always ready to solve our problems for the best.

I did not forget you, Agnese Sonato! I thought you deserved a special place for being first of all a wonderful friend, for sharing confidences, ideas, projects, and more.

I also would like to thank all the people with whom I collaborated, in different contexts and ways, since my PhD experience would not have been the same without them. Thank you to Davide Rurale, Sandro Vestini and Kato-san from JEOL Ltd., for their precious technical support with EBL and interesting discussions about lithography. Thank you to Irene Andreella from the Administration of the Department of Physics and Astronomy (DFA), who was always so kind, extremely precise and ready to help with all bureaucratic issues. I cannot forget the people at NanoFab, where I had the opportunity to spend my first PhD year, with a special thanks to Piero Schiavuta, Francesco Enrichi and Francesco Marinello, together with the

technician Claudio de Lazzari. Also a special thanks to Roberto Pilot from the Department of Chemical Sciences, for his assistance in SERS experiments.

A special thanks must be granted to the A.P.E. Research people, guided by Stefano Prato. It was a great pleasure to collaborate with them and specially with Barbara Troian and Roberto Schiabel, who were always so helpful and kind. From both of them I learned a lot, and I am always happy to visit them in Trieste.

These acknowledgements could well go on for another while if I mentioned all the people who crossed my path in these three years; each and every one made the difference, and I thank them for this.

Before going towards the true end of this thesis, of course, I would like to express my gratitude to my supervisor Filippo Romanato, who brought me in the LaNN adventure. I think this experience educated me not only as a scientist, but first of all as a person, since it allowed me to measure myself with different situations, opportunities and challenges which I think I would not have met so easily in other places.

Finally, my most deep and sincere thank you goes to my parents and to my boyfriend Andrea. They were the ones who, as the dedication says, “believed in me even when I did not”. Every time I was feeling low they were there to support – and bear[6] – me. They never failed to encourage me and stand by my side, as they did throughout my life and, I hope, will do forever.

[6] Actually, the word game sounds better in Italian ☺

Bibliography

[1] M. I. Stockman, "Nanofocusing of optical energy in tapered plasmonic waveguides," *Phys. Rev. Lett.*, vol. 93, p. 137404, 2004.

[2] Y. Gorodetski, N. Shitrit, I. Bretner, V. Kleiner and E. Hasman, "Observation of optical spin symmetry breaking in nanoapertures," *Nano Lett.*, vol. 9, no. 8, pp. 3016-3019, 2009.

[3] H. Raether, Surface Plasmons on Smooth and Rough Surfaces and on Gratings, Berlin: Springer-Verlag, 1988.

[4] S. A. Maier, Plasmonics: fundamentals and applications, Bath: Springer, 2007.

[5] M. L. Brongersma and P. G. Kik, Surface Plasmon Nanophotonics, Atlanta: Springer, 2007.

[6] J. Zenneck, "Über die Fortpflanzung ebener elektromagnetischer Wellen längs einer ebenen Leiterfläche und ihre Beziehung zur drahtlosen Telegraphie," *Ann. Phys.*, vol. 23, pp. 846-866, 1907.

[7] G. Mie, "Beiträge zur Optik trüber Medien, speziell kolloidaler Metallösungen," *Annalen der Physik*, vol. 330, no. 3, pp. 377-445, 1908.

[8] A. Sommerfeld, "Über die Ausbreitlung der Wellen in der drahtlosen Telegraphie," *Annalen der Physik*, vol. 28, pp. 665-736, 1909.

[9] J. Homola, S. S. Yee and G. Gauglitz, "Surface Plasmon resonance sensors: review," *Sensor. Actuat.*, vol. 54, pp. 3-15, 1999.

[10] W. Barnes, A. Dereux and T. Ebbesen, "Surface plasmon subwavelength optics," *Nature*, vol. 424, no. 6950, pp. 824-830, 2003.

[11] A. Sommerfeld, "Über die Fortpflanzung elektrodynamischer Wellen an längs eines Drahtes," *Annalen der Physik*, vol. 67, pp. 233-290, 1899.

[12] R. W. Wood, "On a remarkable case of uneven distribution of light in a diffraction grating spectrum," *Phil. Mag.*, vol. 4, p. 396, 1902.

[13] L. Rayleigh, "On the Dynamical Theory of Gratings," *P. Roy. Soc. Lond. A - Mat.*, vol. 79, no. 532, pp. 399-416, 1907.

[14] U. Fano, "The Theory of Anomalous Diffraction Gratings and of Quasi-Stationary Waves on Metallic Surfaces," *J. Opt. Soc. Am.*, vol. 31, p. 213, 1941.

[15] R. Ritchie, "Plasma Losses by Fast Electrons in Thin Films," *Phys. Rev.*, vol. 106, no.

5, p. 874, 1957.

[16] C. J. Powell and J. B. Swan, "Origin of the Characteristic Electron Energy Losses in Magnesium," *Phys. Rev.*, vol. 116, pp. 81-83, 1959.

[17] C. a. S. J. Powell, "Effect of Oxidation on the Characteristic Loss Spectra of Aluminum and Magnesium," *Physical Review*, vol. 118, pp. 640-643, 1960.

[18] E. A. Stern and R. Ferrell, "Surface Plasma Oscillations of a Degenerate Electron Gas," *Phys. Rev.*, vol. 120, no. 1, pp. 130-136, 1960.

[19] T. Turbadar, "Complete Absorption of Light by Thin Metal Films," *P. Phyis. Soc.*, vol. 73, no. 1, p. 40, 1959.

[20] A. Otto, "Excitation of nonradiative surface plasma waves in silver by the method of frustrated total internal reflection," *Z. Phys.*, vol. 216, p. 398, 1968.

[21] E. Kretschmann and H. Raether, "Radiative decay of non-radiative surface plasmons excited by light," *Z. Naturf.*, vol. 23A, p. 2135, 1968.

[22] Y.-Y. Teng and E. A. Stern, "Plasma Radiation from Metal Grating Surfaces," *Phys. Rev. Lett.*, vol. 19, no. 9, pp. 511-514, 1967.

[23] M. Fleischmann, P. J. Hendra and A. J. McQuillan, "Raman spectra of pyridine adsorbed at a silver electrode," *Chem. Phys. Lett.*, vol. 26, pp. 163-166, 1974.

[24] D. L. Jeanmarie and R. P. Van Duyne, "Surface Raman electrochemistry. Part 1. Heterocyclic, aromatic and aliphatic amines adsorbed on the anodised silver electrode," *J. Electroanal. Chem.*, vol. 84, pp. 1-20, 1977.

[25] M. Moskovits, "Surface roughness and the enhanced intensity of Raman scattering by molecules adsorbed on metals," *J. Chem. Phys.*, vol. 69, no. 9, p. 4159, 1978.

[26] M. Kerker, D.-S. Wand and H. Chew, "Surface enhanced Raman scattering (SERS) by molecules adsorbed at spherical particles," *Appl. Optics*, vol. 19, no. 19, pp. 3373-3388, 1980.

[27] N. W. Ashcroft and N. D. Mermin, Solid State Physics, International Thomson Publishing, 1976.

[28] J. D. Jackson, Classical electrodynamics, 3rd ed, John Wiley & Sons, 1999.

[29] P. Drude, "Zur Elektronentheorie der metalle," *Ann. Phys.*, vol. 306, p. 566, 1900.

[30] L. Novotny and B. Hecht, Principles of Nano-Optics, Cambridge: Cambridge University Press, 2006.

[31] P. B. Johnson and R. W. Christy, "Optical Constants of the Noble Metals," *Phys. Rev.*

B, vol. 6, pp. 4370-4379, 1972.

[32] W. L. Barnes, "Surface plasmon polariton length scales: a route to sub-wavelength optics," *J. of Opt. A: Pure Appl. Opt.*, vol. 8, p. S87, 2006.

[33] E. D. Palik, Handbook of Optical Constants of Solids, Orlando: Academic, 1985.

[34] W. L. Barnes, T. W. Priest, S. C. Kitson and J. R. Sambles, "Physical origin of photonic energy gaps in the propagation of surface plasmons on gratings," *Phys. Rev. B*, vol. 54, p. 6227, 1996.

[35] J. C. M. Garnett, "Colours in Metal Glasses and Metallic Films," *Phil. Trans. Roy. Soc. Lond. A*, vol. 203, pp. 385-420, 1904.

[36] U. Leonhardt, "Optical metamaterials: Invisibility cup," *Nat. Phot.*, vol. 1, pp. 207-208, 2007.

[37] C. F. Bohren and D. R. Huffman, Absorption and Scattering of Light by Small Particles, New York: John Wiley and Sons, 1983.

[38] M. W. Knight, Y. Wu, J. B. Lassiter, P. Nordlander and N. J. Halas, "Substrates Matter: Influence of an Adjacent Dielectric on an Individual Plasmonic Nanoparticle," *Nano Lett.*, vol. 9, no. 5, pp. 2188-2192, 2009.

[39] T. Hutter, S. R. Elliott and S. Mahajan, "Interaction of metallic nanoparticles with dielectric substrates: effect of optical constants," *Nanotechnology*, vol. 24, p. 035201, 2013.

[40] G. Leveque and O. J. .. Martin, "Optical interactions in a plasmonic particle coupled to a metallic film," *Opt. Express*, vol. 14, no. 21, pp. 9971-9981, 2006.

[41] P. Nordlander and E. Prodan, "Plasmon Hybridization in Nanoparticles near Metallic Surfaces," *Nano Lett.*, vol. 4, no. 11, pp. 2209-2213, 2004.

[42] T. Okamoto and I. Yamaguchi, "Optical Absorption Study of the Surface Plasmon Resonance in Gold Nanoparticles Immobilized onto a Gold Substrate by Self-Assembly Technique," *J. Phys. Chem. B*, vol. 107, no. 38, pp. 10321-10324, 2003.

[43] W. R. Holland and D. G. Hall, "Frequency Shifts of an Electric-Dipole Resonance near a Conducting Surface," *Phys. Rev. Lett.*, vol. 52, no. 12, pp. 1041-1044, 1984.

[44] J. R. Krenn, A. Dereux, J. C. Weeber, E. Bourillot, Y. Lacroute, J. P. Goudonnet, G. Schider, W. Gotschy, A. Leitner, F. R. Aussenegg and C. Girard, "Squeezing the Optical Near-Field Zone by Plasmon Coupling of Metallic Nanoparticles," *Phys. Rev. Lett.*, vol. 82, no. 12, pp. 2590-2593, 1999.

[45] M. Quinten and U. Kreibig, "Absorption and elastic scattering of light by particle

aggregates," *Appl. Optics,* vol. 32, no. 30, pp. 6173-6182, 1993.

[46] J. Homola, Surface Plasmon Resonance Based Sensors, Berlin: Springer-Verlag, 2006.

[47] H. Heinzelmann and D. W. Pohl, "Scanning near-field optical microscopy," *Appl. Phys. A,* vol. 59, pp. 89-101, 1994.

[48] B. Hecht, B. Sick, U. P. Wild, V. Deckert, R. Zenobi, O. J. F. Martin and D. Pohl, "Scanning near-field optical microscopy with aperture probes: fundamentals and applications," *J. Chem. Phys.,* vol. 112, no. 18, 2000.

[49] P. Dawson, F. de Fornel and J.-P. Goudonnet, "Imaging of surface plasmon propagation and edge interaction using a photon scanning tunneling microscope," *Phys. Rev. Lett.,* vol. 72, no. 18, pp. 2927-2930, 1994.

[50] O. Marti, H. Bielefeldt, B. Hecht, S. Herminghaus, P. Leiderer and J. Mlynek, "Near-field optical measurement of the surface plasmon field," *Opt. Commun.,* vol. 96, no. 4, pp. 225-228, 1993.

[51] P. M. Adam, L. Salomon, F. de Fornel and J.-P. Goudonnet, "Determination of the spatial extension of the surface-plasmon evanescent field of a silver film with a photon scanning tunnelling microscope," *Phys. Rev. B,* vol. 48, pp. 2680-2683, 1993.

[52] H. Ditlbacher, J. R. Krenn, N. Felidj, B. Lamprecht, G. Schider, M. Salerno, A. Leitner and F. R. Aussenegg, "Fluorescence imaging of surface plasmon fields," *Appl. Phys. Lett.,* vol. 80, no. 3, pp. 404-406, 2002.

[53] T. Reilly, S. Chang, J. Corbam, G. Schatz and K. Rowlen, "Quantitative Evaluation of Plasmon Enhanced Raman Scattering from Nanoaperture Arrays," *J. Phys. Chem. C,* vol. 111, no. 4, pp. 1689-1694, 2007.

[54] F. J. Garcia-Vidal, T. W. Ebbesen and L. Kuipers, "Light passing through subwavelength apertures," *Revs. Mod. Phys.,* vol. 82, 2010.

[55] Q. Cao and P. Lalanne, "Negative role of surface plasmons in the transmission of metallic gratings with very narrow slits," *Phys. Rev. Lett.,* vol. 88, no. 5, p. 057403, 2002.

[56] Y. Xie, A. Zakharian, J. V. Moloney and M. Mansuripur, "Transmission of light through periodic arrays of sub-wavelength slits in metallic hosts," *Opt. Express,* vol. 13, pp. 4485-91, 2005.

[57] Y. Takakura, "Optical resonance in a narrow slit in a metallic screen," *Phys. Rev. Lett.,* vol. 86, p. 5601, 2001.

[58] F. Marquier, J. J. Greffet, F. Pardo and J. L. Pelouard, "Resonant transmission through a metallic film due to coupled modes," *Opt. Express,* vol. 13, p. 70, 2005.

[59] H. Hartnagel, A. Dawar, A. Jain and C. Jagadish, Semiconducting Transparent Thin Films, Philadelphia: Institute of Physics, 1995.

[60] C. G. Granqvist and A. Hultaker, "Transparent and conducting ITO films: new developments and applications," *Thin Solid Films,* vol. 411, pp. 1-5, 2002.

[61] C. W. Tang and S. A. Van Sylke, "Organic electroluminescent diodes," *Appl. Phys. Lett.,* vol. 51, p. 913, 1987.

[62] H. Kim, C. Gilmore, A. Piqué, J. Horwitz, M. H., H. Murata, Z. Kafafi and D. Chrisey, "Electrical, optical, and structural properties of indium–tin–oxide thin films for organic light-emitting devices," *J. Appl. Phys.,* vol. 86, no. 11, pp. 6451-6461, 1999.

[63] G. Sberveglieri, P. Benussi, G. Coccoli, S. Groppelli and P. Nelli, "1990," *Thin Solid Films,* vol. 186, pp. 349-360, 1988.

[64] Y. S. Cho, J. J. Hong, S. M. Yang and C. J. Choi, "Nanostructured antistatic and antireflective thin films made of indium tin oxide and silica over-coat layer," in *Proceedings of SPIE - Nanostructured Thin Films III*, San Diego, California (USA), 2010.

[65] R. Tueta and M. Braguier, "Fabrication and Characterization of Indium Tin Oxide Thin Films for Electroluminescent Applications," *Thin Solid Films,* vol. 80, pp. 143-148, 1981.

[66] E. C. Le Ru and P. Etchegoin, Principles of SERS, Oxford: Elsevier, 2009.

[67] K. B. Biggs, J. P. Camden, J. N. Anker and R. P. Van Duyne, "Surface-Enhanced Raman Spectroscopy of Benzenethiol Adsorbed from the Gas Phase onto Silver Film over Nanosphere Surfaces: Determination of the Sticking Probability and Detection Limit Time," *J. Phys. Chem. A,* vol. 113, no. 16, pp. 4581-4586, 2009.

[68] R. Favors, Y. Jiang, Y. Loethen and D. Ben-Amotz, "External Raman standard for absolute intensity and concentration measurements," *Rev. Sci. Instrum.,* vol. 76, p. 033108, 2005.

[69] C. L. Haynes and R. P. Van Duyne, "Plasmon-Sampled Surface-Enhanced Raman Excitation Spectroscopy," *J. Phys. Chem. B,* vol. 107, no. 30, p. 7426–7433, 2003.

[70] E. Hutter and J. H. Fendler, "Exploitation of Localized Surface Plasmon Resonance," *Adv. Mater.,* vol. 16, no. 19, pp. 1685-1706, 2004.

[71] M. L. Brongersma, "Plasmonics: Engineering optical nanoantennas," *Nat. Phot.,* vol. 2, pp. 270-272, 2008.

[72] K. A. Willets and R. P. Van Duyne, "Localized Surface Plasmon Resonance Spectroscopy and Sensing," *Annu. Rev. Phys. Chem.,* vol. 58, pp. 267-297, 2007.

[73] D. K. Gramotnev and S. I. Bozhevolnyi, "Plasmonics beyond the diffraction limit," *Nat. Photon.,* vol. 4, p. 83, 2010.

[74] A. Kinkhabwala, Z. Yu, S. Fan, Y. Avlasevich, K. Mullen and W. E. Moerner, "Large single-molecule fluorescence enhancements produced by a bowtie nanoantenna," *Nat. Phot. Lett.,* vol. 3, pp. 654-657, 2009.

[75] M. Agio, "Optical antennas as nanoscale resonators," *Nanoscale,* vol. 4, pp. 692-706, 2012.

[76] I. S. Maksymov and A. E. Miroshnichenko, "Active control over nanofocusing with nanorod plasmonic antennas," *Opt. Express,* vol. 19, no. 7, pp. 5888-5894, 2011.

[77] J. J. Mock, M. Barbic, D. R. Smith, D. A. Schultz and S. Schultz, "Shape effects in plasmon resonance of individual colloidal silver nanoparticles," *J. Chem. Phys.*, vol. 116, no. 15, p. 6755, 2002.

[78] K. L. Kelly, C. E., Z. L. L. and G. C. Schatz, "The Optical Properties of Metal Nanoparticles: The Influence of Size, Shape, and Dielectric Environment," *J. Phys. Chem. B,* vol. 107, no. 3, p. 668–677, 2003.

[79] C. a. H. J. Nehl, "Shape-dependent plasmon resonances of gold nanoparticles," *J. Mater. Chem.,* vol. 18, pp. 2415-2419, 2008.

[80] E. Tatartschuk, E. Shamonina and L. Solymar, "Plasmonic excitations in metallic nanoparticles: Resonances, dispersion characteristics and near-field patterns," *Opt. Express,* vol. 17, no. 10, pp. 8447-8460, 2009.

[81] W. Rechberger, A. Hohenau, A. Leitner, J. R. Krenn, B. Lamprecht and F. R. Aussenegg, "Optical properties of two interacting gold nanoparticles," *Opt. Commun.,* vol. 220, p. 137–141, 2003.

[82] L. J. Sherry, P. Chang, P. S. Schatz, R. P. Van Duyne, B. J. Wiley and Y. Xia, "Localized surface plasmon resonance spectroscopy of single silver nanocubes," *Nano Lett.,* vol. 10, no. 2034-2038, p. 5, 2005.

[83] C. L. Nehl, H. Hongwei Liao and J. H. Hafner, "Optical Properties of Star-Shaped Gold Nanoparticles," *Nano Lett.,* vol. 6, no. 4, p. 683–688, 2006.

[84] J. P. Kottmann and O. J. F. Martin, "Plasmon resonant coupling in metallic nanowires," *Opt. Express,* vol. 8, no. 12, pp. 655-663, 2001.

[85] J. Aizpurua, G. W. Bryant, L. J. Richter, F. J. García de Abajo, B. K. Kelley and T. Mallouk, "Optical properties of coupled metallic nanorods for field-enhanced spectroscopy," *Phys. Rev. B,* no. 71, p. 235420, 2005.

[86] J. B. Jackson, S. L. Westcott, L. R. Hirsch, J. L. West and N. J. Halas, "Controlling the surface enhanced Raman effect via the nanoshell geometry," *Appl. Phys. Lett.,* vol. 82, no. 257, 2003.

[87] J. Aizpurua, P. Hanarp, D. S. Sutherland, M. Kall, G. W. Bryant and F. J. Garcìa de Abajo, "Optical Properties of Gold Nanorings," *Phys. Rev. Lett.,* vol. 90, no. 5, p. 057401, 2003.

[88] P. Bharadwaj, B. Deutsch and L. Novotny, "Optical Antennas," *Adv. Opt. Photon.,* vol. 1, pp. 438-483, 2009.

[89] E. J. Smythe, E. Cubukcu and F. Capasso, "Optical properties of surface plasmon resonances of coupled metallic nanorods," *Opt. Express,* vol. 15, no. 12, pp. 7439-7447, 2007.

[90] P. Mühlschlegel, H. J. Eisler, O. J. .. Martin, B. Hecht and D. W. Pohl, "Resonant optical antennas," *Science,* vol. 308, no. 5728, pp. 1607-1609, 2005.

[91] B. Willingham, D. W. Brandl and P. Nordlander, "Plasmon hybridization in nanorod dimers," *Appl. Phys. B,* vol. 93, pp. 209-216, 2008.

[92] J. Britt Lassiter, J. Aizpurua, L. I. Hernandez, D. W. Brandl, I. Romero, S. Lal, J. H. Hafner, P. Nordlander and N. J. Halas, "Close Encounters between Two Nanoshells," *Nano Lett.,* vol. 8, no. 4, pp. 1212-1218, 2008.

[93] S. Enoch, R. Quidant and G. Badenes, "Optical sensing based on plasmon coupling in nanoparticle arrays," *Opt. Express,* vol. 12, no. 15, pp. 3422-3427, 2004.

[94] K. Kneipp, Y. Wang, H. Kneipp, L. T. Perelman, I. Itzkan, R. Dasari and M. S. Feld, "Single molecule detection using surface-enhanced Raman scattering (SERS)," *Phys. Rev. Lett.,* vol. 78, pp. 1667-1670, 1997.

[95] S. Nie and S. R. Emory, "Probing Single Molecules and Single Nanoparticles by Surface-Enhanced Raman Scattering," *Science,* vol. 275, no. 5303, pp. 1102-1106, 1997.

[96] H. Xu, E. J. Bjerneld, M. Käll and L. Börjesson, "Spectroscopy of Single Hemoglobin Molecules by Surface Enhanced Raman Scattering," *Phys. Rev. Lett.,* vol. 83, no. 21, 1999.

[97] J. Beermann, S. M. Novikov, K. Leosson and S. I. Bozhevolnyi, "Surface enhanced Raman imaging: periodic arrays and individual metal nanoparticles," *Opt. Express,* vol. 17, no. 15, pp. 12698-12705, 2009.

[98] B. Auguié and W. L. Barnes, "Collective Resonances in Gold Nanoparticle Arrays," *Phys. Rev. Lett.,* vol. 101, p. 143902, 2008.

[99] C. Steuwe, C. F. Kaminski, J. J. Baumberg and S. Mahajan, "Surface Enhanced Coherent Anti-Stokes Raman Scattering on Nanostructures Gold Surfaces," *Nano Lett.,* vol. 11, p. 5339–5343, 2011.

[100] H. Harutyunyan, G. Volpe, R. Quidant and L. Novotny, "Enhancing the Nonlinear Optical Response Using Multifrequency Gold-Nanowire Antennas," *Phys. Rev. Lett.,* vol. 108, no. 21, p. 217403, 2012.

[101] M. A. Kats, P. Genevet, G. Aoust, N. Yu, R. Blanchard, F. Aieta, Z. Gaburro and F. Capasso, "Giant birefringence in optical antenna arrays with widely tailorable optical anisotropy," *Proc. Natl. Acad. Sci.,* vol. 109, no. 31, p. 12364–12368, 2012.

[102] M. W. Vogel and D. K. Gramotnev, "Shape effects in tapered metal rods during adiabatic nanofocusing of plasmons," *J. Appl. Phys.,* vol. 107, p. 044303, 2010.

[103] J. A. Kong, Electromagnetic wave theory, New York: Wiley, 1990.

[104] L. Novotny and S. J. Stranick, "Near-Field Optical Microscopy and Spectroscopy with Pointed Probes," *Annu. Rev. Phys. Chem.,* vol. 57, pp. 303-331, 200657.

[105] D. O'Connor, M. McCurry, B. Lafferty and A. V. Zayats, "Plasmonic waveguide as an efficient transducer for high-density data storage," *Appl. Phys. Lett.,* vol. 95, p. 171112, 2009.

[106] D. K. Gramotnev and K. C. Vernon, "Adiabatic nano-focusing of plasmons by sharp metallic wedges," *Appl. Phys. B,* vol. 86, p. 7, 2007.

[107] P. Nagpal, N. Lindquist, S. Oh and D. Norris, "Ultrasmooth patterned metals for plasmonics and metamaterials," *Science,* vol. 325, p. 594, 2009.

[108] A. Boltasseva, V. Volkov, R. Nielsen, E. Moreno, S. Rodrigo and S. Bozhevolnyi, "Triangular metal wedges for subwavelength plasmon-polariton guiding at telecom wavelengths," *Opt. Express,* vol. 16, p. 5252, 2008.

[109] I. S. Bozhevolnyi, "Plasmonic nanoguides and circuits," Singapore, Pan Stanford, 2009, p. 353.

[110] D. K. Gramotnev, M. W. Vogel and M. I. Stockman, "Optimized nonadiabatic nanofocusing of plasmons by tapered metal rods," *J. Appl. Phys.,* vol. 104, p. 034311, 2008.

[111] D. F. P. Pile and D. K. Gramotnev, "Adiabatic and nonadiabatic nanofocusing of plasmons by tapered gap plasmon waveguides," *Appl. Phys. Lett.,* vol. 89, p. 041111, 2006.

[112] K. C. Vernon, D. K. Gramotnev and D. F. P. Pile, "Adiabatic nanofocusing of

plasmons by a sharp metal wedge on a dielectric substrate," *J. Appl. Phys.,* vol. 101, p. 104312, 2007.

[113] E. Verhagen, L. K. Kuipers and A. Polman, "Plasmonic nanofocusing in a dielectric wedge.," *Nano Lett.,* vol. 10, no. 9, p. 3665, 2010.

[114] M. Ohtsu, K. Kobayashi, T. Kawazoe, S. Sangu and T. Yatsui, "Nanophotonics: design, fabrication, and operation of nanometric devices using optical near fields," *IEEE, J. Sel. Top. Quantum Electron.,* vol. 8, p. 839, 2002.

[115] K. Kato, A. Ono, W. Inami and Y. Kawata, "Plasmonic nanofocusing using a metal-coated axicon prism," *Opt. Express,* vol. 18, p. 13580, 2010.

[116] E. Moreno, S. Rodrigo, S. Bozhevolnyi, L. Marin-Moreno and F. Garcia-Vidal, "Guiding and focusing of electromagnetic fields with wedge plasmon polaritons," *Phys. Rev. Lett.,* vol. 100, no. 2, p. 023901, 2008.

[117] A. V. Zayats and D. Richards, Nano-Optics and Near-Field Optical Microscopy, London: Artech House, 2009.

[118] W. Chen, D. Abeysinghe, R. Nelson and Q. Zhan, "Experimental confirmation of miniature spiral plasmonic lens as a circular polarization analyzer," *Nano Lett.,* vol. 10, no. 6, p. 2075, 2010.

[119] S. Yamamoto and H. Watarai, "Surface-Enhanced Raman Spectroscopy of Dodecanethiol-Bound Silver Nanoparticles at the Liquid/Liquid Interface," *Langmuir,* vol. 22, p. 6562, 2006.

[120] L. Allen, M. J. Beijersbergen, R. J. C. Spreeuw and J. P. Woerdman, "Orbital angular-momentum of light and the transformation of Laguerre–Gaussian laser modes," *Phys. Rev. A,* vol. 45, p. 8185, 1992.

[121] A. M. Yao and M. J. Padgett, "Orbital angular momentum: origins behavior and applications," *Adv. Opt. Photon.,* vol. 3, p. 161, 2011.

[122] M. Massari, F. Romanato, M. Carli, T. Ongarello, M. Prasciolu, F. Tamburini, E. Mari, A. Bianchini and C. Baribieri, "Design, fabrication and characterization of phase masks for astronomical applications," *Microelectron. Eng.,* vol. 88, pp. 2675-2678, 2011.

[123] L. Vuong, A. Adam, J. Brok, P. Planken and H. Urbach, "Electromagnetic spin-orbit interactions via scattering of subwavelength apertures.," *Phys. Rev. Lett.,* vol. 104, p. 083903, 2010.

[124] M. Kang, J. Chen, B. Gu, Y. Li, L. Vuong and H. T. Wang, "Spatial splitting of spin states in subwavelength metallic microstructures via partial conversion of spin-to-orbital

angular momentum," *Phys. Rev. A,* vol. 85, p. 035801, 2012.

[125] N. Shitrit, I. Bretner, Y. Gorodetski, V. Kleiner and E. Hasman, "Optical spin Hall effects in plasmonic chains.," *Nano Lett.,* vol. 11, p. 2038, 2011.

[126] Y. Gorodetski, A. Niv, V. Kleiner and E. Hasman, "Observation of the spin-based plasmonic effect in nanoscale structures," *Phys. Rev. Lett.,* vol. 101, no. 4, 2008.

[127] H. Kim, J. Park, S.-W. Cho, S.-Y. Lee, M. Kang and B. Lee, "Synthesis and dynamic switching of surface plasmon vortices with plasmonic vortex lens.," *Nano Lett.,* vol. 10, no. 2, pp. 529-536, 2010.

[128] K. T. Gahagan and G. A. Swartzlander, "Simultaneous trapping of low-index and high-index microparticles observed with an optical-vortex trap," *J. Opt. Soc. Am. B.,* vol. 16, p. 533, 1999.

[129] Y. S. Kivshar and B. Luther-Davies, "Dark optical solitons: physics and applications," *Phys. Rev.,* vol. 298, p. 81, 1998.

[130] J. Scheuer and M. Orenstein, "Optical vortices crystals: Spontaneous generation in nonlinear semiconductor microcavities," *Science,* vol. 285, p. 230, 1999.

[131] S. Pancharatnam, "Generalized theory of interference, and its applications," *Proc. Indian Acad. Sci.,* vol. A44, p. 247, 1956.

[132] M. V. Berry, "Quantum phase factors accompanying adiabatic changes," *P. Roy. Soc. Lond.,* vol. A392, p. 45, 1984.

[133] S. Yang, W. Chen, R. L. Nelson and Q. Zhan, "Miniature circular polarization analyzer with spiral plasmonic lens," *Opt. Lett.,* vol. 34, p. 3047, 2009.

[134] S. W. Cho, J. Park, S. Y. Lee, H. Kim and B. Lee, "Coupling of spin and angular momentum of light in plasmonic vortex," *Opt. Express,* vol. 20, p. 10083, 2012.

[135] P. Zilio, E. Mari, G. Parisi, F. Tamburini and F. Romanato, "Angular momentum properties of electromagnetic field transmitted through holey plasmonic vortex lenses," *Opt. Lett.,* vol. 37, no. 15, pp. 3234-3236, 2012.

[136] E. Abbe, "Beiträge zur Theorie des Mikroskops und der mikroskopischen Wahrnehmung," *Archiv für Mikroskopische Anatomie,* vol. 9, no. 1, pp. 413-418, 1873.

[137] G. S. Kino and G. Xiao, "Scanning Confocal Optical Microscope". USA Patent 5.022.743, 11 June 1991.

[138] E. Synge, "A suggested method for extending the microscopic resolution into the ultramicroscopic region," *Phil. Mag.,* Vols. 6, 356, p. 356, 1928.

[139] D. W. Pohl, W. Denk and M. Lanz, "Optical stethoscopy: Image recording with resolution λ/20," *Appl. Phys. Lett.,* Vols. 44, 651, p. 651, 1984.

[140] G. Binnig and H. Rohrer, "Scanning Tunneling Microscopy," *Helv. Phys. Acta,* vol. 55, no. 6, pp. 726-735, 1982.

[141] E. Betzig, P. L. Finn and J. S. Weiner, "Combined shear force and near-field scanning optical microscopy," *Appl. Phys. Lett.,* vol. 60, p. 2484, 1992.

[142] E. Betzig, J. K. Trautman, T. D. Harris, J. S. Weiner and R. L. Kostelak, "Breaking the Diffraction Barrier: Optical Microscopy on a Nanometric Scale," *Science,* vol. 251, no. 5000, pp. 1468-1470, 1991.

[143] G. A. Valaskovic, M. Holton and G. H. Morrison, "Parameter control, characterization, and optimization in the fabrication of optical fiber near-field probes," *Appl. Optics,* vol. 34, no. 7, pp. 1215-1228, 1995.

[144] S. Munster, S. Werner, C. Mihalcea, W. Scholz and E. Oesterschulze, "Novel micromachined cantilever sensors for scanning near-field optical microscopy," *J. Microsc.,* vol. 186, no. 1, pp. 17-22, 1997.

[145] D. Turner, "US Patent". USA Patent 4.469.554, 1984.

[146] A. Bouhelier, T. Huser, H. Tamaru, H. J. Guntherodt, D. W. Pohl, F. I. Baida and D. Van Labeke, "Plasmon optics of structured silver films," *Phys. Rev. B,* vol. 63, no. 5, p. 155404, 2001.

[147] A. Passian, R. H. Ritchie, A. L. Lereu, T. Thundat and T. L. Ferrell, "Curvature effects in surface plasmon dispersion and coupling," *Phys. Rev. B,* vol. 71, no. 11, p. 115425, 2005.

[148] R. Esteban Llorente, Apertureless SNOM: realistic modeling of the imaging process and measurements of resonant plasmonic nanostructures, EPFL, 2007.

[149] Y. Inouye and S. Kawata, "A scanning near-field optical microscope having scanning electron tunnelling microscope capability using a single metallic probe tip," *J. Microsc.,* vol. 178, no. 1, pp. 14-19, 1995.

[150] B. Knoll and F. Keilmann, "Near-field probing of vibrational absorption for chemical microscopy," *Nature,* vol. 399, pp. 134-137, 1999.

[151] F. Romanato, R. Piilot, M. Massari, T. Ongarello, G. Pirruccio, P. Zilio, G. Ruffato, M. Carli, D. Sammito, V. Giorgis, D. Garoli, R. Signorini, P. Schiavuta and R. Bozio, "Design, fabrication and characterization of plasmonic gratings for SERS," *Microelectron. Eng.,* vol. 88, p. 2717–2720, 2011.

[152] G. Zacco, F. Romanato, A. Sonato, D. Sammito, G. Ruffato, M. Morpurgo, D. Silvestri, M. Carli, P. Schiavuta and G. Brusatin, "Sinusoidal plasmonic crystals for bio-detection sensors," *Microelectron. Eng.*, vol. 88, pp. 1898-1901, 2011.

[153] A. Sonato, G. Ruffato, G. Zacco, D. Silvestri, M. Natali, M. Carli, G. Giallongo, G. Granozzi, M. Morpurgo and F. Romanato, "Calibration of Surface Plasmon Resonance Output Through the Enhanced Sensitivity Azimuthally-Controlled Grating-Coupled System," *Sensor. Actuat. B – Chem.*, vol. 181, pp. 559-566, 2013.

[154] W. Barnes, A. Dereux and T. Ebbesen, "Surface Plasmon subwavelength optics," *Nature*, vol. 424, pp. 824-830, 2003.

[155] A. Broers, "Resolution Limits of PMMA Resist for Exposure with 50 kV Electrons," *J. Electrochem. Soc.: Solid State Sci. & Technol.*, vol. 128, no. 1, pp. 166-170, 1981.

[156] K. Murata, T. Matsukaw and R. Shimizu, "Monte Carlo Calculations on Electron Scattering in a Solid Target," *Jap. J. Appl. Phys.*, vol. 10, no. 6, p. 678, 1971.

[157] M. Parikh, "Corrections to proximity effects in electron beam lithography," *J. Appl. Phys*, vol. 50, p. 1104, 1979.

[158] N. Unal, M. Charlton, Y. Wang, U. Waizmann, T. Reindl and U. Hofmann, "Easy to adapt electron beam proximity effect correction parameter calibration based on visual inspection of a ‘‘Best Dose Sensor’’," *Microelectron. Eng.*, vol. 88, p. 2158–2162, 2011.

[159] J. Pavkovich, "Proximity Effect Correction Calculations by the Integral-Equation Approximate Solution Method," *J. Vac. Sci. Technol. B*, vol. 4, no. 1, 1986.

[160] S. Yasin, Nanotechnology using Electron Beam Lithography and Ultrasonically Assisted Development in Organic Resists, Ph.D. Thesis, University of Cambridge, 2001., University of Cambridge, 2001.

[161] S. Yasin, D. Hasko and H. Ahmed, "Comparison of MIBK/ IPA and water / IPA as PMMA developers for electron beam nanolithography," *Microelectron. Eng.*, vol. 61–62, p. 745–753, 2002.

[162] S. Yasin, D. G. Hasko, M. N. Khalid, D. J. Weaver and H. Ahmed, "Influence of polymer phase separation on roughness of resist features," *J. Vac. Sci. Technol. B*, vol. 22, no. 2, pp. 574-578, 2004.